

UNIVERSIDADE FEDERAL DO RIO GRANDE
INSTITUTO DE MATEMÁTICA, ESTATÍSTICA E FÍSICA
PROGRAMA DE PÓS GRADUAÇÃO EM FÍSICA

GEFERSON LUCATELLI

**A New Approach to Galaxy Structural Analysis with the
Curvature of the Brightness Profile**

Rio Grande – RS

Março de 2019

GEFERSON LUCATELLI

**A New Approach to Galaxy Structural Analysis with the Curvature of the
Brightness Profile**

Dissertação de mestrado realizada sob orientação
do Prof. Dr. Fabricio Ferrari e apresentada ao Insti-
tuto de Matemática, Estatística e Física da FURG
em preenchimento parcial dos requisitos para a
obtenção do título de Mestre em Física.

Área de estudo: Física Teórica/ Astrofísica.

Orientador: Fabricio Ferrari

Rio Grande – RS

Março de 2019

Geferson Lucatelli

A New Approach to Galaxy Structural Analysis with the Curvature of the Brightness Profile

Dissertação de mestrado realizada sob orientação do Prof. Dr. Fabricio Ferrari e apresentada ao Instituto de Matemática, Estatística e Física da FURG em preenchimento parcial dos requisitos para a obtenção do título de Mestre em Física, aprovada pela comissão de avaliação abaixo assinada:

Trabalho _____ . **Rio Grande – RS**, Março de 2019:

Prof. Dr. Fabricio Ferrari
Orientador (Universidade Federal do Rio Grande –
FURG)

Profª. Drª. Ana Chies Santos
(Universidade Federal do Rio Grande do Sul –
UFRGS)

Prof. Dr. Sandro Barboza Rembold
(Universidade Federal de Santa Maria – UFSM)

Prof. Dr. Stavros Akras
(Universidade Federal do Rio Grande – FURG)

Rio Grande – RS
Março de 2019

Este trabalho é dedicado em especial, à minha mãe Iria Maria Damini Lucatelli.

Dedico ainda:

à todas as pessoas que não tiveram a oportunidade de estudar, mas que são competentes no que fazem.

à todas as pessoas humildes, que possuem como primeira filosofia, a simplicidade.

ao fim da barreira que divide a “elite intelectual” e a sociedade;

por fim, ao anticonservadorismo.

Agradecimentos

Gostaria de deixar registrado meus agradecimentos as pessoas que estiveram comigo ao longo da minha jornada acadêmica.

Primeiramente, agradeço à minha família; à minha companheira Thais Pereira e aos meus amigos Lucas e Dani; peço também desculpas por querer controlar tanto o tempo e por estar indisponível na maioria das vezes.

Aos meus amigos Jefferson, Calígula, Walas, Lara, Sara, Adriano e Ana Laura.

Ao Prof. Fabricio pelas ideias sugeridas para esta pesquisa desenvolvida; além de todas as discussões.

Ao Prof. Horácio Dottori e ao Leonardo Ferreira por todos comentários úteis na pesquisa.

Aos professores Ana Chies Santos, Sandro Barboza Rembold e Stavros Akras pela participação da banca.

Ao Centro de Atendimento Psicológico da FURG, que me fez perceber que minha vida não se resume a academia.

A todo auxílio prestado pela FURG, desde as Políticas de Assistência Estudantil – os quais foram fundamentais para minha estabilidade, até os recursos prestados pela Universidade (PROPESP) para minha participação em eventos.

Ao PPGFísica-IMEF pela infraestrutura fornecida.

Aos funcionários terceirizados da FURG: em especial aos que atuam no IMEF; e ao seguranças Manuel e Marcone.

Por fim, agradeço ao subsídio recebido da Coordenação de Aperfeiçoamento de Pessoal de Nível Superior – Brasil (CAPES).

*“Sick of politicians, harassment and laws.
All we do is get screwed up by other people’s flaws.
World turned upside down now, nothing else to do.
Live in concrete jungles, house block seven view.
And that ain’t no joke, you could disappear in smoke.”*

Hawkwind – The Psychedelic Warlords (Disappear In Smoke)

Resumo

Neste trabalho introduzimos a curvatura do perfil de brilho de uma galáxia, como uma maneira não paramétrica para identificar suas componentes estruturais. Tais componentes como por exemplo, bojos, barras, discos, braços espirais, lentes, anéis, entre outras, são fundamentais para o entendimento do caminho formativo e evolutivo em que as galáxias se submeteram. Identificá-las é também crucial para a classificação morfológica de galáxias. Com essa nova medida, foram analisadas em detalhe a curvatura de 16 galáxias com variadas morfologias. Uma alta (baixa) taxa de variação do perfil de brilho mostra altos (baixos) valores absolutos de curvatura. Além disso, regiões de transição entre componentes mostram altos valores de curvatura. Com essa nova metodologia foram identificados padrões que caracterizam bojo (pseudo ou clássico), discos, barras e anéis. O procedimento de cálculo e análise poderá ser automatizado em breve para lidar com o processamento de uma grande quantidade de dados e identificar as componentes das respectivas galáxias de uma forma automática, ou fornecer um ponto inicial para tal análise onde se utilizam métodos tradicionais de modelagem da distribuição de luz de múltiplas componentes. Como complemento, ao que nos motivou a introdução da medida de curvatura, analisamos como é o comportamento de ajustes de Sérsic únicos (e.g. n) e do índice de concentração C para galáxias de múltiplas componentes. Foram obtido que tais galáxias possuem altos valores dessas medidas (C e n) e são comparáveis aos medidos em galáxias de componentes únicas, portanto levando a classificação errônea dessas galáxias.

Palavras-chave: galáxias: morfometria – galáxias: parâmetros fundamentais – galáxias: análise estrutural – galáxias: fotometria

Abstract

In this work we introduce the curvature of a galaxy brightness profile to non-parametrically identify its structural subcomponents. Bulges, bars, disks, lens, rings, spiral arms and so on, are a key to understanding the formation and evolutionary paths the galaxy undertook. Their identification is also crucial for the morphological classification of galaxies. We measure and analyse in detail the curvature of 16 galaxies with varied morphology. High (low) steepness profiles show high (low) absolute curvature measures. Transitions between components present high values of the curvature. With this new tool we identify patterns that characterise bulges (pseudo or classic), disks, bars, rings, spiral arms. The procedure can be automated in a future study to deal with large datasets and identify galaxy components automatically, or to provide a reliable starting point for traditional multi components modelling of galaxy light distribution. For a complementary study, which leaded us to introduce the curvature, we investigate the behaviour of single-Sérsic fits (e.g. single Sérsic index n) and concentration index C for multicomponent galaxies. We have obtained that these galaxies have systematically high values of n and C comparable to the ones measured in single component galaxies, thus resulting in misclassification of them.

Keywords: galaxies: morphometry – galaxies: fundamental parameters – galaxies: structure analysis – galaxies: photometry

List of figures

Figure 11	– The curvature and its associated osculating circle for a unidimensional curve. At each different point P in a path or curve, an osculating circle can be placed in which it passes through P and some of its neighbour points. The radius, and so the curvature, of this circle changes as we move to another different point P' . . .	31
Figure 12	– Similar to FIGURE 11, but extended to a bidimensional surface. \mathbf{N} stands for the normal vector at each point P	32
Figure 13	– Plots of Equation (4.19) for different Sérsic indices. The higher is n , the higher is $\tilde{\varkappa}$ in the inner regions, which is reasonable because high n represent inner components. Note that for large R , the $\tilde{\varkappa}$ profiles are similar.	36
Figure 14	– Example of the procedure to calculate $\tilde{\varkappa}(R)$ for the EFIGI/SDSS data of galaxy NGC 1211/PGC 11670. Left Top: first derivative of $I(R)$, raw (blue) and filtered (green). Left Bottom: the same but for the second derivative of $I(R)$. Right: log-normalized brightness profile $v(R)$ (red) and the raw (blue) and filtered (green) curvature. The solid vertical lines represent the possible transition between regions dominated by different components, and will be explained latter on Section 4.5. The vertical dashed line delimit the regions where the signal-to-noise S/N goes below 2 and we avoid to interpret profiles outside that region.	37
Figure 15	– Top Left: SDSS r image for NGC1211 from the EFIGI sample. The yellow lines represent each component of the galaxy. These regions were drawn from the local peaks in the green line of $\tilde{\varkappa}(R)$ (see bellow). The numbers in the yellow ellipses and in the $\tilde{\varkappa}$ plots refer to the same regions. Top Right: Residual from a single Sérsic fit to the image above made with MORFOMETRYKA. For both, yellow dotted lines correspond to regions identified in the curvature plot below; yellow dot-dashed line is the $2R_p$ region. Bottom: Normalized log-brightness profile (red curve) and curvature $\tilde{\varkappa}$ calculated from it (green curve). The solid vertical lines delimit regions of different components (see text for details). The vertical dashed line is the limit of confidence of $SNR=2$	39
Figure 16	– Near infrared band ($3.6\mu\text{m}$) of NGC 1357 from Spitzer telescope. Labels and graphic positions are the same as FIGURE 15, and the same for the remaining figures. Region 1 is the bulge (high and large peak in $\tilde{\varkappa}$). Region 2 is the disk with spiral arms and the outer disk is region 3 with low values in curvature. Again, the dashed vertical line ($SNR=2$) is our limit of confidence. See the text for further details of this galaxy.	40

Figure 17 – The same as FIGURE 15, but for r band of NGC 936 from EFIGI. See text for details.	46
Figure 18 – The same as FIGURE 15, but for NGC 2767 from HST (f160w).	47
Figure 19 – The same as FIGURE 15, but for r -band of NGC 4267 from EFIGI.	49
Figure 20 – The same as FIGURE 15, but for i -band of NGC4251 from SDSS.	50
Figure 21 – The same as FIGURE 15, but for r band of NGC4417 from EFIGI.	51
Figure 22 – The same as FIGURE 15, but for r band of NGC4452 from EFIGI.	52
Figure 23 – The same as FIGURE 15, but for r band of NGC 1512 from CTIO telescope.	53
Figure 24 – The same as FIGURE 15, but for r band of NGC 2273 from Pan-STARRS survey.	55
Figure 25 – The same as FIGURE 15, but for near infrared band ($3.56\mu\text{m}$) of NGC 7723 from Spitzer telescope.	56
Figure 26 – The same as FIGURE 15, but for r band of NGC 6056.	57
Figure 27 – The same as FIGURE 15, but for NGC 1270 from HST (f160w).	58
Figure 28 – The same as FIGURE 15, but for NGC 472 from HST (f160w).	59
Figure 29 – The same as FIGURE 15, but for NGC 384 from HST (f160w).	60
Figure 30 – The same as FIGURE 15, but for r band of NGC 1052 from EFIGI.	61
Figure 31 – Results of $\tilde{\alpha}(R)$ for sorted galaxies under C_i (left) of TABLE 2. The three elliptical galaxies are PGC 29249, PGC 38740 and PGC 36678 while the others have a very different behaviour in $\tilde{\alpha}$, indicating that they are multicomponent.	65
Figure 31 – continued.	66
Figure 32 – Curvature calculated for the galaxies with high Sérsic indices of TABLE 1.	67
Figure 33 – Diagnostic diagram for: Left: the information entropy H versus the integrated area under $\tilde{\alpha}$ for ~ 1600 galaxies of the EFIGI sample. Right: the concentration index C_i versus the integrated area under $\tilde{\alpha}$ for the same sample.	69

List of tables

Table 1 – Examples of galaxies with high n_{eff} supposed to be misclassified by inappropriate single Sérsic fit.	23
Table 2 – Some galaxies of EGIFI with the highest values in C_1 (left) and C_2 (right).	27
Table 3 – Data sample used in this work.	45

Summary

1	INTRODUCTION	I
1.1	Formation & evolution of galaxies	I
1.2	Galaxy Morphology	3
2	JUSTIFICATION & OBJECTIVES	17
2.1	Justification	17
2.2	General Objectives	18
2.3	Specific objectives	18
3	MISCLASSIFICATION OF SPIRALS AND DISKS GALAXIES BY C AND n	21
3.1	Effective Sérsic Index and misclassification	21
3.2	Concentration C and Misclassification	24
4	CURVATURE OF THE GALAXY BRIGHTNESS PROFILE	29
4.1	Mathematical Definitions	29
4.2	Curvature of a Sérsic Law	34
4.3	Measuring $I(R)$ with MORFOMETRYKA	35
4.4	Filters for $\tilde{\chi}$	36
4.5	Case Studies	38
5	RESULTS & DISCUSSIONS	43
5.1	Data	43
5.2	Analysis of $\tilde{\chi}$ for individual galaxies	44
5.2.1	Lenticular Galaxies	46
5.2.2	Spirals	53
5.2.3	Spheroidal components	58
5.3	Identifying galaxy structures with curvature	62
5.4	Misclassification of galaxies using C and n	66
5.5	Further Analysis	68

6	FINAL REMARKS	71
----------	--------------------------------	-----------

References	73
-----------------------------	-----------

APPENDIX	85
---------------------------	-----------

APPENDIX A – ARTICLE I (SUBMITTED)	87
---	-----------

APPENDIX B – PYTHON CODE FOR $\tilde{\pi}(R)$	109
---	------------

I

INTRODUCTION

“There is no dark side of the moon, really. Matter of fact it’s all dark.”

Pink Floyd – Eclipse

1.1 Formation & evolution of galaxies

Galaxy formation and evolution are vital to understand the Universe as a whole, for galaxies portray the general structure where they emerged and evolved. Galaxy morphology provides us with a framework on which we describe galaxy structures that are connected with such evolution. The processes that gave birth to bulges, disks, bars, rings, arms, halos, for example, are imprinted in the properties or absence of these features. However, classification only cannot describe purely how they formed and evolved, the need is to understand their formation mechanism which in this way allows us to built a connection between assembly theory and observable properties ([TONINI et al., 2016](#)).

To understand the formation and evolution of galaxies, several steps are taken. The observational part of galaxies is made in terms of starlight, therefore such formation and evolution knowledge starts by exploring the star formation history ([KEEL, 2007](#)). Also, galaxies are contained in a cosmological universe, which means we see them at different times due to the redshift, therefore any formative model/scenario of galaxies must account for each property at the different stages of the evolution in the cosmological context ([MO; BOSCH; WHITE, 2010](#)). In order to understand these aspects, in the past decades some scenarios were explored by means of different formative processes such as hierarchical galaxy formation ([WHITE; REES, 1978; COLE et al., 2000](#)), merger formation ([TOOMRE; TOOMRE, 1972](#)), secular evolution ([KORMENDY; KENNICUTT JR., 2004; FALCON-BARROSO; KNAPEN, 2013](#)), chemical evolution ([LYNDEN-BELL, 1975; PAGEL, 2001; PRANTZOS, 2008; PAGEL, 2009; MATTEUCCI,](#)

2012) and using semi-analytical models (KAUFFMANN; WHITE; GUIDERDONI, 1993; COLE et al., 1994; SOMERVILLE; PRIMACK, 1999; LACEY, 2001).

With respect to the traditional understandings of galaxy formation and evolution, we have the following. In these scenarios, the basics of formation and evolution distinguishes distinct processes that origin elliptical galaxies and classical bulges from the formation of disk dominated/spiral galaxies and pseudo bulges. The first mechanism are merger events having violent relaxations and hierarchical clustering (TOOMRE; TOOMRE, 1972; TONINI et al., 2016; NAAB; TRUJILLO, 2006; HOPKINS et al., 2010). In the merger scenario, it is established that elliptical galaxies are formed by major mergers of spiral galaxies (BURKERT; NAAB, 2003). In the case of spiral, lenticular and irregular galaxies, first it was supposed that they are a result of formative evolution where rapid violent processes such as hierarchical clustering and merging led to the formation of them (WHITE; REES, 1978; WHITE; FRENK, 1991; FIRMANI; AVILA-REESE, 2003; BUTA, 2013).

Bulges can be formed by two different ways and therefore separated in two categories: classical originates from violent processes such as hierarchical clustering via minor mergers (NAAB; TRUJILLO, 2006; HOPKINS et al., 2010; GADOTTI, 2009), are dynamically hot and posses similar properties of elliptical galaxies (FISHER; DRORY, 2008); pseudo originates from secular evolution through longer times scales where disk material is rearranged by bars and spiral structures in a slow steady process (WYSE; GILMORE; FRANX, 1997; FIRMANI; AVILA-REESE, 2003; KORMENDY; KENNICUTT JR., 2004; ATHANASSOULA, 2005; GUEDES et al., 2013; GROSSI et al., 2018). Characteristics of pseudo bulges are not found in elliptical galaxies and can be similar to those of disks, which are dynamically cold with the kinematics dominated by rotation (FISHER; DRORY, 2008). Even so, not all bulges can be clearly labelled as classic or pseudo, for there are bulges that present a mix of properties of the two types (KORMENDY; KENNICUTT JR., 2004).

More recently, however, computer simulations such as (SPRINGEL et al., 2005; DUBOIS et al., 2014; VOGELSBERGER et al., 2014; SCHAYE et al., 2015; KAVIRAJ et al., 2017) (between many others) allowed more profound studies on galaxy formation and evolution (MARTIN et al., 2019). Therefore the principles of the ideas commented above changed slightly and other assumptions raised. For example, to cite only: pseudobulges instead of being formed only by secular processes, can also be formed trough dynamical process (GUEDES et al., 2013), and also from major mergers (KESELMAN; NUSSER, 2012; GROSSI et al., 2018); dark matter haloes can also evolve in terms of two phases (not only by secular evolution (GADOTTI, 2009)), early by major mergers and later by minor mergers (ZHAO et al., 2003; DIEMAND; KUHLEN; MADAU, 2007; ASCASIBAR; GOTTLÖBER, 2008).

The brief introduction above is far way from the real picture of the actual understanding of how galaxies forms and evolves. A review made by [Naab and Ostriker \(2017\)](#) and references therein can cover the main questions about the formation and evolution of galaxies in recent years.

1.2 Galaxy Morphology

Preview

Galaxy morphological classification helps us to recognise the processes that drives galaxy evolution ([BUTA, 2013](#)). The first ideas were presented by [Reynolds \(1920\)](#) and later by [Hubble \(1926\)](#), [Hubble \(1936\)](#), who separated galaxies in classes, constituting the Hubble sequence - early to late types galaxies. Their classification, and the main similar procedures adopted by others in the XX Century, were based on visual examination of galaxy images. The procedures of classification gained in detail along the years, new parameters and schemes have been introduced but they remained based on the visual inspection of the image by an expert ([MORGAN, 1958](#); [VAUCOULEURS, 1959b](#); [BERGH, 1960b](#); [BERGH, 1960a](#); [SANDAGE, 1961](#); [BERGH, 1976](#); [BUTA, 2013](#)),

Within this scheme of components as building blocks of galaxy structure, it is relevant to quantify which structures are present in a given galaxy and what is their contribution to the total galaxy light compared to other components. There are several ways to accomplish that, in general by modelling each component in an analytical fashion and then trying a combination of them that best describes the galaxy light distribution ([CAON; CAPACCIOLI; D'ONOFRIO, 1993](#); [PENG et al., 2002](#); [SIMARD et al., 2002](#); [SOUZA; GADOTTI; ANJOS, 2004](#); [ERWIN, 2015](#)). This process can describe the galaxy photometry very precisely. However, there are some drawbacks. In cases of multicomponent, which are the majority of galaxies, the minimisation data-model is numerically unstable and converges only with the assistance of an experienced user, which limits the range of the model parameters. Furthermore, the joint component models fitted to the galaxy can be degenerate for different combinations of the parameters, giving the same residuals within the photometric errors, and thus are inconclusive. In some cases leading to situations where they are not physically reasonable.

These restrictions can be overcomed with user inspection, as mentioned. Nevertheless, the flood of photometric data that was been made available in the last two decades, for example since the first data release of SDSS ([ABAZAJIAN et al., 2003](#)) (to cite only one big survey) urged us to reinvent

our basic methods and tools to appropriate from all the physical information contained in it. Thus, a method which can infer the basic properties of the components of a given galaxy automatically and non-parametrically could greatly increase the amount of information we could gather from the survey's data. In this way, we introduce the **curvature of the galaxy's brightness profile** $\kappa(R)$ with the purpose of inferring the galaxy's structural components.

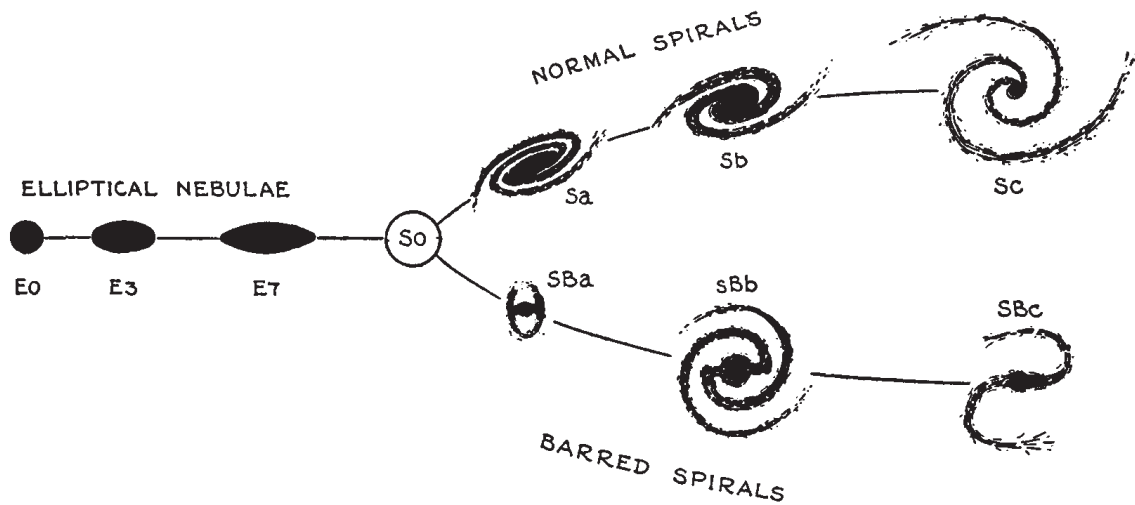
Visual classification of galaxies

Galaxy classification is the starting point from which it is possible to recognize signatures of the formation and evolution of galaxies from observations. It helps to unveil the process that drove the galaxy evolution ([BUTA, 2013](#)). The first attempts in a galaxy's classification has been accomplished with [Reynolds \(1920\)](#) and [Hubble \(1926\)](#), [Hubble \(1936\)](#) with the so called "Hubble sequence of galaxies", see [FIGURE 1](#). They focused their analysis in a visual approach where they divided elliptical galaxies (left of the diagram) – called early-type galaxies – from spiral galaxies (right of the diagram) – called late-type galaxies. In a few words, elliptical galaxies are systems with symmetrical shapes as well as continuous and smooth light distribution along radii. Moreover, they have symmetric shapes. Spiral galaxies on the other hand are objects that have noteworthy structures and can undergo to abrupt variations in the light distributions along radii, mainly because the spiral arms or the transition between components like bulge-bar-disc, for example. In [FIGURE 1](#) we also see a type of galaxy that is – in some sense, photometrically – a combination of elliptical galaxy with disk galaxy, which are called lenticular galaxies (S0's). Basically, they have a bulge contained inside a disk in absence of spiral arms, while others can have more components like bars, rings and lenses, for example.

It is very important to keep in mind that the Hubble sequence is not related to a time evolution diagram, in principle the galaxies in the left do not evolve to the galaxies in the right, neither the opposite. The galaxies are kept to be displayed in this way historically. The formation and evolution of disk/spirals and bulge/ellipticals was briefly discussed previously, but a more detailed study can be found in [Naab and Ostriker \(2017\)](#) for example.

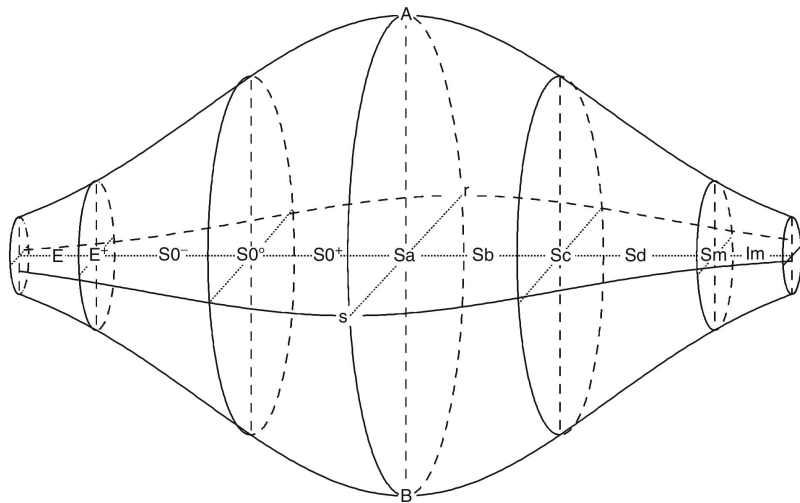
After the Hubble-Reynolds schema, [Vaucouleurs \(1959a\)](#) and [Sandage \(1961\)](#) introduced a new and more complete diagram to classify galaxies, called volume-classification schema, shown in [FIGURE 2](#). It is a tridimensional system which separates different morphologies in a continuous way . The most fundamental feature is the main axis, called **stage** or **T -type**. This is a numerical sequence comprehended in the interval $-5 \lesssim T \lesssim +10$. Elliptical galaxies are designed by $T = -5$, while $T = 10$

FIGURE 1 – The Reynold-Hubble classification scheme – “Tuning Fork”. It constitutes the basic of the Hubble sequence of galaxies – early (left) to late (right) types.



Source: Adapted from [Hubble \(1936\)](#)

FIGURE 2 – de Vaucouleurs-Sandage volume classification schema ([VAUCOULEURS, 1959a](#); [SANDAGE, 1961](#)).



Source: Adapted from [Keel and Oswalt \(2013\)](#).

are irregulars. The transition between ellipticals and So's in the diagram are represented by the interval $T = -\varsigma$ to $T = -I$.

This continuous way originated the following sub-classification for galaxies: morphologies S(B)a, S(B)b and S(B)c – (B) stands for barred, if not, normal/unbarred – have the intermediary groups S(B)ab and S(B)bc. Also, intermediary spirals SA(B)a, SA(B)ab, are differentiated from other spirals. The other axes of the schema are the **varieties** and **families**. These terminologies indicates

how notable are, for example, rings and bars, and how they differ from the main stage. Following ([BUTA; COMBES, 1996](#)), strong rings are labelled by (r), while in absence of rings or smooth rings (\equiv pseudorings) are labelled by (s) and (rs), respectively. Furthermore, there are other components such as lens, labelled by (l), outer rings , labelled by (R), and pseudorings, labelled by (R'). Complete details of these components and others can be found in [Buta and Combes \(1996\)](#) and in the review made by [Buta \(2013\)](#). After Hubble and de Vaucouleurs-Sandage schemas, others schemes were also taking in account for more details of galaxies, to cite only ([BERGH, 1960b](#); [BERGH, 1960a](#); [BERGH, 1976](#); [ELMEGREEN; ELMEGREEN, 1982](#); [ELMEGREEN; ELMEGREEN, 1987](#)).

Galaxy Photometry

The galaxy starlight is all electromagnetic energy emitted by stars, clouds, dust, etc. Computing the total light coming from a galaxy is one of the first ways we have to extract information about the structural properties of galaxies. Galaxy photometry was one of the first attempts in such study, to understand how the light distribution changes along the extension of a galaxy, seeking to find patterns of different structural components such as bulges, bars, disks and so on.

The remarkable work in the field was made by [de Vaucouleurs \(1948\)](#) where the first surface brightness profile techniques was introduced. The intensity of the light profile I of a galaxy can be defined as follows: consider a radial distance R of the galaxy in relation to its centre, then take ellipses with same isophotal intensities (galactic isophotes). In this sense, I can be defined as the variation of the mean intensities of these isophotes along one deprojected axis R of the isophotes . In general R is taken to be the semi-major axis of the elliptical isophotes, see ([FERRARI et al., 2004](#)). See also Section 4.3 for more information of how we determine $I(R)$ from the data im this work.

In [de Vaucouleurs \(1948\)](#), he selected a sample of elliptical galaxies and observed that most of them follow the empirical light profile of the form

$$I(R) = I_o \exp \left[- \left(\frac{R_\theta}{R} \right)^{1/4} \right] \quad (1.1)$$

where R_θ is a scale radii of the galaxy and I_o is the isophotal intensity at that point (i.e. $I(R_\theta) = I_o$).

After de Vaucouleurs's work, another singular one was accomplished with ([SÉRSIC, 1963](#);

SÉRSIC, 1968). He generalized equation (1.1) with¹

$$I(R) = I_n \exp \left\{ -b(n) \left[\left(\frac{R_n}{R} \right)^{1/n} - 1 \right] \right\} \quad (1.3)$$

where n is the Sérsic index. The quantity R_n is the radial distance that encloses half of the total luminosity of the profile and I_n is the isophotal intensity at R_n . The quantity $b(n)$ is defined in such way to ensure the definition of R_n holds, and given by (CIOTTI; BERTIN, 1999)

$$b(n) \approx 2n - \frac{I}{3}. \quad (1.4)$$

Sérsic's work was one of most cited papers in the field (GRAHAM; DRIVER, 2005), because equation (1.3) can describe well adequately the light profile of galaxies such as ellipticals (wide range of n) but also galactic components such as bulges (GADOTTI, 2009) (wide range of n), disks ($n \sim 1$, exponential profile) (FREEMAN, 1970) and bars ($n \sim 0.5$) (GADOTTI et al., 2007; GADOTTI, 2008) as well as other components such as rings and lens, where n can range between $n \sim 0.1$ and $n \sim 0.5$, see for example (KORMENDY; BENDER, 2012). An additional note is that not all disks follow a $n = 1$ profile (CAROLLO, 1999; LOTZ; PRIMACK; MADAU, 2004; LAURIKAINEN; PELETIER; GADOTTI, 2016). Furthermore, there are other types of galactic disks which are not represented by a unique well defined exponential disk profile, they are composition of multiple disks, usually an inner and an outer. These kind of disks are separated in two more classes: of type-II and type-III (MUÑOZ-MATEOS et al., 2013) (type I are the usual single disks.)

It is important to mention that many other mathematical functions have been defined in order to understand the shape of $I(R)$ in galactic data, for example: Plummer model (PLUMMER, 1911), King profile (KING, 1962), Jaffe model (JAFFE, 1983), Nuker law (LAUER et al., 1995) and the Core-Sérsic model (GRAHAM et al., 2003; TRUJILLO et al., 2004). Each mathematical form is used to describe different physical situations between galaxies and also between different structural components. For example, restricting ourselves only to (SÉRSIC, 1968), a pure Sérsic model describes effectively the light profile of an elliptical galaxy; a model with the sum of a Sérsic and a exponential disk ($n \sim 1$) describes the composition of a bulge and a disk, respectively, constituting then an bulged-disky galaxy (e.g. So).

Several techniques to distinguish galaxy components have been developed over the years. Basically they are classified whether they perform the modelling in the extracted brightness profile

¹ In reality, Sérsic generalized it as

$$I(R) = I_o \exp \left[- \left(\frac{R_o}{R} \right)^{\frac{1}{n}} \right]. \quad (1.2)$$

The expression (1.3) was introduced only later (see text).

of the galaxy ($1D$ modelling) or directly in the galaxy image ($2D$ modelling). The most widespread $1D$ approach is to fit ellipses to a set of isophotes – an evolution of aperture photometry done at the telescope (JEDRZEJEWSKI, 1987; JUNGWIERT; COMBES; AXON, 1997; ERWIN; SPARKE, 2003; CABRERA-LAVERS; GARZÓN, 2004; ERWIN, 2004; SALO; LAURIKAINEN; BUTA, 2005; GADOTTI et al., 2007; PÉREZ; SÁNCHEZ-BLÁZQUEZ; ZURITA, 2009).

For each isophote there is a collection of geometric and physical parameters that describe it, including the brightness profile (energy flux as a function of distance) which is later used to compare to a model of the components of the galaxy. As a side effect, this technique is often used to identify behaviour in the parameters (ellipticity, position angle, Fourier coefficients of the ellipse expansion) that may indicate the domain of different components or, in another context, to give hints of ancient interactions, mergers or cannibalism. Also with a similar purpose, other non-parametric approaches like unsharp masking (MALIN, 1977) (ERWIN; SPARKE, 2003; KIM et al., 2012) and structure maps (POGGE; MARTINI, 2002; KIM et al., 2012) are used. Unidimensional techniques are better suited to extract geometric information of individual isophotes, but incorporating the instrument response function (the PSF – point spread function) is not trivial. Furthermore, there is no consensus on which distance coordinate to use to extract the profile – major or minor axis or different combination of both – whose choice impacts the leading parameters (FERRARI et al., 2004).

Two-dimensional algorithms (see below) operate directly in the galaxy image, so there is no ambiguity in extracting the brightness profile. Real PSFs can be incorporated in the models and the process (convolution) in this conserves energy. Their disadvantage are the high computational cost – not so critical nowadays – and the instability to initial conditions. This instability raises wildly with the number of components and free parameters in the models. In some situations (e.g. a combination of bulge, bar and disc), the algorithm only converges if the initial parameters are very close to the final ones, which makes the algorithm itself unnecessary (HAUSSLER et al., 2007).

Regardless the method, $1D$ or $2D$, the galaxy is then modelled with a combination of components, usually described with a Sérsic function (SÉRSIC, 1968) with different n , scale lengths and intensity to resemble a bulge, a disk, a bar and so on. The most common fitting procedure is the bulge-disk decomposition, where to the bulge part of $I(R)$ it is associated a Sérsic law of parameters (n_b, I_b, R_b) (index “ b ” stands for bulge) and for the disk ($n_d \sim I, I_d, R_d$) (index “ d ” stands for disk). There are many works applying this kind of analysis (GAO; HO, 2017; TASCA, 2004; TASCA; WHITE, 2011; KENT, 1985; BAGGETT; BAGGETT; ANDERSON, 1998; JONG, 1996; CAON; CAPACCIOLI; D'ONOFRIO, 1993) and some of them in an automated fashion (GADOTTI et al., 2007; GADOTTI, 2008; DIMAURO

et al., 2018; SOUZA; GADOTTI; ANJOS, 2004; CHENG et al., 2011; LACKNER; GUNN, 2012; SIMARD et al., 2011; PENG et al., 2002; PENG et al., 2010; BRUCE et al., 2014b; ROBOTHAM et al., 2017; ARGYLE et al., 2018). Also, multiple other Sérsic profiles (n_{outer} , I_{outer} , R_{outer}) (“outer” stands for any other outer component) can be added to the fitting to model additional components, like bars, lenses, rings and so on (GADOTTI, 2008; KORMENDY; BENDER, 2012). This procedure can be used more robustly and for a large number of galaxies.

To perform this analysis, computational algorithms were developed to work with fittings procedures to these functions, in order to get the best fit parameters to each $I(R)$ of galactic components (bulges, disks, ...) (multicomponent fitting) and galaxies (single component fitting). Some standard algorithms are GALFIT (PENG et al., 2002; PENG et al., 2010), IMFIT (ERWIN, 2015), BUDDA (SOUZA; GADOTTI; ANJOS, 2004), GIM2D (SIMARD et al., 2002), MORFOMETRYKA (FERRARI; CARVALHO; TREVISAN, 2015), among others. These new tools for galaxy photometry have been developed to be semi-automated (because requires initial input parameter) and applied to a large data set of galaxies.

However, besides these improvements, automatise bulge-disk decomposition requires many efforts to be implemented, it allows us to obtain overall statistics of the galaxies in the data, neglecting fine details in their structures (BUTA, 2013) (the same applies for single-fits). Furthermore, many issues still remain and particular ones will be explored in this dissertation. For the moment we note that the main root of these difficulties are associated to the fact that, as stated by Lotz, Primack and Madau (2004), single and multiple component fitting assumes that the galaxies are well described by smooth and symmetric profiles. However, most of galaxies are not only a combination of bulge+disk components and are additionally formed by irregular, tidally disturbed components or merging galaxies. Therefore to fully study them it is required other methodologies which do not involve parametrized profiles.

Single Sérsic fit (effective profile)

A single Sérsic fit does not consider components separately and covers the entire galaxy profile. Such fits result in a single set of parameters $(n, I_n, R_n)_s$ ². These set of parameters: i) can describe very well the light profile if the galaxy is single component; ii) might describe the overall information of the galaxy structure if it is multicomponent. In this work we refer as the effective Sérsic parameter n_{eff} any Sérsic parameter obtained by a single Sérsic fit (no matter how many components the galaxy has).

² The subscript “*s*” stands for “single”.

A single component fit procedure sometimes is not robust for multicomponent galaxies since $I(R)$ changes its slope in the transition region of each component. There are though works in which a single Sérsic fits is used/considered (VIKA et al., 2013; HäUFLER et al., 2013). Mathematically, if $I(R)_{\text{eff}}$ is the effective profile, the relation between the single profile and the bulge-disk decomposed one is given by

$$I(R)_{\text{eff}} \sim I_B(R) + I_D(R) \quad (1.5)$$

$$\begin{aligned} I_{n,\text{eff}} \exp \left\{ -b(n_{\text{eff}}) \left[\left(\frac{R_{n,\text{eff}}}{R} \right)^{1/n_{\text{eff}}} - 1 \right] \right\} &\sim I_b \exp \left\{ -b(n_b) \left[\left(\frac{R_b}{R} \right)^{1/n_b} - 1 \right] \right\} \\ &\quad + I_d \exp \left\{ -b(I) \left[\left(\frac{R_d}{R} \right) - 1 \right] \right\}. \end{aligned} \quad (1.6)$$

To be more specific, consider the case of $I(R) = I_D(R) + I_B(R)$ where the transition between bulge and disk is abrupt. An effective profile could not be used because the natural shape of the Sérsic law is smooth along R and a single component does not cover effectively the transition between bulge and disk (the same applies to other components). On the other hand, still there are cases where a composition B+D has a smooth transition between both. In these cases and for elliptical galaxies³ a single Sérsic fit is sufficient to represent good enough all the light profile $I(R)$ along all radii. We will see briefly in Chapter 3 that effective profiles of this kind leads to misclassification of galaxies.

Galaxy Morphometry

Galaxy classification via visual approaches are widely used in astrophysics. The most known is probably the Galaxy Zoo Project⁴. However, as the resolution of the images becomes spatially lower, it became more difficult to distinguish different components by eye. In this case, the analysis might be limited to a sample of nearby galaxies. Also, to classify a large amount of galaxies by eye requires a significant number of classifiers.

The question is that these classifications by eye are susceptible to become subjective when we move to larger data sets. This is notably seen in the evolution of the Hubble diagram itself. In the beginning it encompassed few morphologies, however latter evolved to a more complex schema as more galaxies were discovered and studied (VAUCOULEURS, 1959a; SANDAGE, 1961) (SANDAGE; SANDAGE; KRISTIAN, 1975; VAUCOULEURS et al., 1991; ELMEGREEN; ELMEGREEN, 1982; ELMEGREEN; ELMEGREEN, 1987; BERGH, 1960a; BERGH, 1960b; BERGH, 1976).

³ Exception are for elliptical galaxies having a core component, see the Nuker-Core law (LAUER et al., 1995; KORMENDY et al., 1994; GRAHAM et al., 2003).

⁴ <https://zoo4.galaxyzoo.org/>.

Furthermore, measure the galaxy light between bulges and disk is challenging ([TASCA; WHITE, 2011](#)) and frequently lead to degeneracy issues⁵ ([LAURIKAINEN; PELETIER; GADOTTI, 2016](#); [ANDRAE; JAHNKE; MELCHIOR, 2011](#); [BRUCE et al., 2014a](#); [FISCHER; BERNARDI; MEERT, 2017](#); [JONG et al., 2004](#); [SAGLIA et al., 1997](#); [PENG et al., 2010](#); [SANI et al., 2011](#); [MEERT; BERNARDI; VIKRAM, 2013](#)). Because this, performing bulge+disk decompositions require some considerations and sophisticated procedures for the results be physical.

These questions have motivated the development of new techniques for galaxy classification, the so called **morphometry** or **non-parametric approaches**. They do not involve parameters and all information is obtained directly from statistical calculations above the imaging data (below, some of them will be reviewed). The quantities obtained are commonly called **morphometric indices**.

In summary, the main goals of morphometry are to be: i) independent of parameters or any analytical function which reduces the number of physical quantities to be interpreted in each result, and removes convergence issues; ii) based on statistical calculations above the imaging data; iii) flexible and computationally fast; iv) independent of initial guests and human interference (which is subjective), thus it is applicable to large data sets⁶.

Despite these advantages, there are some assumptions to be made, which gives some obstacles to the procedures (in particular to the concentration, asymmetry and smoothness, see their explanations in the next pages). As argued by [Lotz, Primack and Madau \(2004\)](#):

Because concentration is measured within several circular apertures about a predefined center, it implicitly assumes circular symmetry, making it a poor descriptor for irregular galaxies. Asymmetry is more sensitive to merger signatures than concentration, but not all merger remnant candidates are highly asymmetric, and not all asymmetric galaxies are mergers (e.g., dusty edge-on spirals). Finally, the clumpiness determination requires one to define a galaxy smoothing length, which must be chosen carefully to avoid systematic effects dependent on a galaxy image's point-spread function (PSF), pixel scale, distance, and angular size. ([LOTZ; PRIMACK; MADAU, 2004](#), p.164)

Because that, many improvements in each procedure is still in development.

One of the first procedures aimed for non-parametric quantities is attributed to ([MORGAN, 1958](#); [MORGAN, 1959](#)), where he measured the concentration of light in galaxy centres relating it with different spectral types of stars present there. Later on, a series o papers invested in non-parametric quantities ([KENT, 1985](#); [ABRAHAM et al., 1994](#); [BERSHADY; JANGREN; CONSELICE, 2000](#); [CONSELICE](#),

⁵ As an example, for multicomponent galaxies it is possible to build identical light profiles $I(R)$ with different combinations of the Sérsic law's parameters (n, R_n, I_n)

⁶ Photometry can also be automated to be independent of initial guesses and human interference in order to be applicable to large data sets, for example automated bulge+disk decompositions

(BERSHADY; JANGREN, 2000) introducing the indices of concentration of light C , asymmetry A . These two indices along with the smoothness S constitutes today the basis of morphometry – the CAS morphometric system. To enhance this set, new indices were introduced: the aforementioned smoothness S (CONSELICE, 2003), Gini G (ABRAHAM; BERGH; NAIR, 2003; LOTZ; PRIMACK; MADAU, 2004) and moment of light M (LOTZ; PRIMACK; MADAU, 2004), thus consolidating the CASGM system. Recently Ferrari, Carvalho and Trevisan (2015) added two more indices, spirality σ_ψ and the information entropy H . Together, they redefined the calculations of A , S and C . In this work we aim to add the curvature measure $\tilde{\kappa}$ to this morphometric system.

Morphometric indices are not just numerical and statistical indicators of some class of galaxy, they are related to microscopic and macroscopic physical processes in galaxy structures. For example, the concentration index C is related to the macroscopic distribution of light, describing how much the light is concentrated in the galaxy in relation to its centre (the higher the value, the more concentrated the light is). The smoothness S indicates the existence of small structures, for example revealing the presence of star formation regions. Spirality σ_ψ unveils existence of spiral and small scale structures too, or in general, distinguishes homogeneous system from heterogeneous. Many examples of physical relations with these and other indices can be found (CONSELICE; BERSHADY; JANGREN, 2000; CONSELICE, 2003; LOTZ; PRIMACK; MADAU, 2004; BERSHADY; JANGREN; CONSELICE, 2000; ABRAHAM; BERGH; NAIR, 2003; ABRAHAM et al., 1994). For completeness, a recent review of morphometry is presented by Conselice (2014) with a rich physical background in subjects of formation and evolution of galaxies (in cosmological context) relating to some of these indices.

The great advantage of morphometry is that it is able to reduce the difficult of interpretation of the results in relation to parametric approaches where many parameters might be involved in the extraction of information of a single data (which sometimes might be incoherent with physical observables and also can lead to non-physical models and results). In conclusion, non-parametric approaches helps in the task to recognize different structural components in a galaxy and separate different galaxy morphologies in an elegant way. Also, the steps to be taken in the use of these tools are still uncertain and are continuously being improved. Below, we review some of the well established procedures.

Concentration Index C

The concentration index is defined as the ratio between two circular radii that encloses a percentage of the total galaxy luminosity. For example, if R_f and R_i are the outer and inner radii, the concentration index C_{if} can be defined as

$$C_{if} \equiv \log_{10} \left(\frac{R_f}{R_i} \right). \quad (1.7)$$

where i and f stands for inner percentile ($i\%$) and outer percentile ($f\%$), respectively.

The most common concentration indices are defined as: i) with $R_f = R_{80}$ and $R_i = R_{20}$ – apertures that encloses 80% and 20% of the total luminosity, respectively; ii) and with $R_f = R_{90}$ and $R_i = R_{50}$. Thus

$$C_{28} = \log_{10} \left(\frac{R_{80}}{R_{20}} \right), \quad C_{59} = \log_{10} \left(\frac{R_{90}}{R_{50}} \right). \quad (1.8)$$

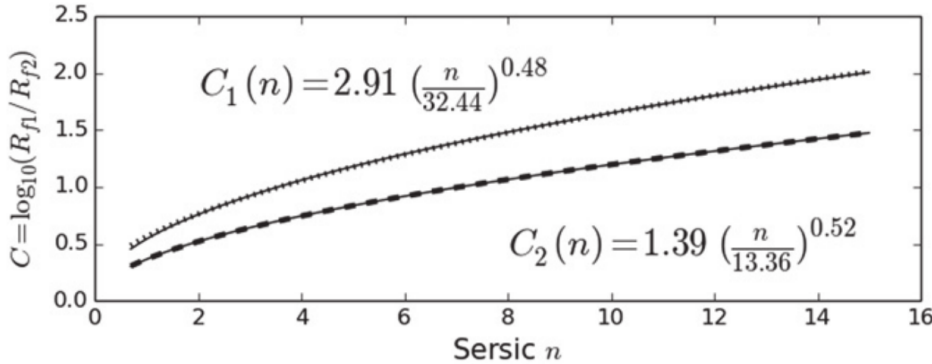
These are the new definitions of C made by [Ferrari, Carvalho and Trevisan \(2015\)](#), conveniently relabelled by $C_1 \equiv C_{28}$ and $C_2 \equiv C_{59}$. A note is that the definition of C in [Bershady, Jangren and Conselice \(2000\)](#) considers a factor ζ in front of \log_{10} .

There is a well defined correlation between C and the Sérsic index n ([ANDRAE; JAHNKE; MELCHIOR, 2011; GRAHAM; DRIVER, 2005; TRUJILLO; GRAHAM; CAON, 2001](#)), therefore both parameters (C, n) describe the concentration of light in the galaxy ([ZHAO; ARAGÓN-SALAMANCA; CONSELICE, 2015](#)). In [FIGURE 3](#) we have the plots of C_1 and C_2 as a function of n for single Sérsic profiles, a relationship between C and n well behaved. Similar results are found in ([TRUJILLO; GRAHAM; CAON, 2001; GRAHAM; DRIVER, 2005](#)). This relationship is also present in an analysis of SDSS, as showed by [Gadotti \(2009\)](#) in its Figure 5, top plot. The concentration calculated correlates well with the fitted values of n , and having a saturation point after $n \sim 4$.

Smoothness S

The smoothness S is an estimation to detect small structures in the galaxies ([CONSELICE, 2003](#)). Such regions can be regions of star formation, gas distribution and traces of a bar. S is calculated by means of the difference between two images: the original image I and the original image attenuated by a filter σ , label I^σ . The final result is obtained by normalizing the last step. New definitions of S have been made by [Ferrari, Carvalho and Trevisan \(2015\)](#), in terms of the Pearson $p(x, y)$ and Spearman $s(x, y)$

FIGURE 3 – Relation between $C_1 (\equiv C_{2g})$ and $C_2 (\equiv C_{5g})$ as a function of n .



Source: Adapted from [Ferrari, Carvalho and Trevisan \(2015\)](#).

correlation indices of I and I^σ ,

$$S_2 = I - p(I, I^\sigma), \quad S_3 = I - s(I, I^\sigma). \quad (1.9)$$

Asymmetry \mathcal{A}

The asymmetry quantifies how asymmetric are the structures in a galaxy ([CONSELICE; BERSHADY; JANGREN, 2000](#)). \mathcal{A} is calculated by means of the difference between two images: the original image I and the original image rotated by π radians, label I^π . In general, \mathcal{A} is obtained normalizing this difference by the original image. In the same way as S , [Ferrari, Carvalho and Trevisan \(2015\)](#) redefined the calculation of \mathcal{A} in terms of p and s (the same as before in S) of the images I and I^π ,

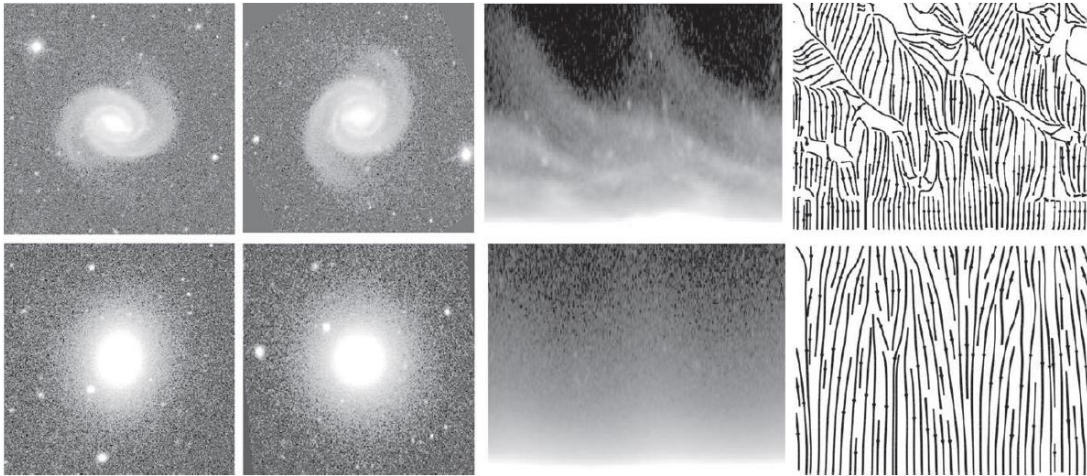
$$\mathcal{A}_2 = I - p(I, I^\pi), \quad \mathcal{A}_3 = I - s(I, I^\pi). \quad (1.10)$$

Information Entropy H

The information entropy H ([SHANNON; WEAVER, 1949](#)) is a measure of used in information theory. Consider a discrete random variable u_i , containing information about some quantity of a system. The quantity of information we can extract from this variable is related to the degree of probability $p(u)$ that a certain value has to happen. The information measure is obtained from H

$$H\{u_i\} = - \sum_i p(u_i) \log_2 [p(u_i)]. \quad (1.11)$$

FIGURE 4 – Example of calculation of spirality σ_ψ for a spiral and an elliptical galaxies.



Source: Adapted from [Ferrari, Carvalho and Trevisan \(2015\)](#).

This measure was introduced to morphometry to quantify the information of a given galaxy image ([FERRARI; CARVALHO; TREVISAN, 2015](#)), by

$$H(I) = - \sum_k^K p(I_k) \ln[p(I_k)] \quad (1.12)$$

where I_k is the intensity of light in the k -pixel, $p(I_k)$ is its probability of occurrence and K is the dimension of the distribution. The entropy can be normalized by the maximum value of H , which is of that a uniform distribution, $H_{\max} = \ln K$, hence

$$\widetilde{H}(I) = \frac{H(I)}{\ln K}. \quad (1.13)$$

Spirality σ_ψ

In the same way as S and A , the spirality σ_ψ , introduced by [Ferrari, Carvalho and Trevisan \(2015\)](#), allows to unveil the existence of symmetric and non-symmetric structures in galaxies, mainly bars and spiral arms. To calculate σ_ψ , as an example see FIGURE 4, the galaxy image is standardized to have the ratio of the semi axis (minor and major) equal to one, $q = 1$. After the image is decomposed in polar coordinates (R, ϑ) and the gradient ψ is taken on $I(R, \vartheta)$. Each structural component shows a distinct pattern in the image, contributing in different ways for ψ . It is seen that the bulge in the top spiral galaxy is characterized by a homogeneous strip in the inner region and the field lines of ψ are almost horizontal. In the spiral region, on the other hand, we see that the lines have different orientations because the spiral arms vary their orientations along R and ϑ .

The spirality quantifies the deviations of these directions, and for each horizontal line of pixels, it is calculated the standard deviation of all orientations of the field and then the scalar of σ_ψ is obtained. Therefore, symmetric and non-symmetric systems shows, respectively, small and high spirality values. According to [Ferrari, Carvalho and Trevisan \(2015\)](#), early-type galaxies $\sigma_\psi \lesssim 0.2$ while late-types $\sigma_\psi \gtrsim 0.3 - 0.4$

2

JUSTIFICATION & OBJECTIVES

“The task is not to see what has never been seen before, but to think what has never been thought before about what you see everyday.”

Erwin Rudolf Josef Alexander Schrödinger

2.1 Justification

In this work we aim to study the structure of galaxies with a novel approach – the curvature $\tilde{\kappa}$. The fundamental goal is to understand the spatial configuration of a galaxy in terms of its structural components, for example, bulges, bars, disks, rings, among others. The key point in any study that recognises these structures and separate them by their spatial domain regions is that it opens a possibility to understand the formative and evolutionary mechanism that drove the galaxy and its components. Knowing the exact structure of a galaxy is significant because, as we have seen, each structure is related to some particular formative and evolutionary mechanism. The obstacle then appears if a component is inferred in a given galaxy, but in fact it is not present, consequently misleading conclusions will be drawn about the evolutionary history of the galaxy

The curvature $\tilde{\kappa}(R)$ can be used to identify if a galaxy is single or multicomponent, and in this case, it would inform the radial scale length of each component. This is possible because $\tilde{\kappa}$ calculated on the radial profile is a measure of its steepness, and a priori each component has its own. We argue that this new approach is more physically motivated than previously ones because it is independent of parameters. In this work we are firstly introducing the concept and analysing the results in an non-automated way, the automation and improvements is left for a next work.

2.2 General Objectives

Following these considerations, our general objective in this work is to, given the galaxy light profile $I(R)$, discern when the galaxy is single or multicomponent. Our approach is to calculate the curvature $\tilde{\kappa}(R)$ of $I(R)$ in order to identify the existence of bulges, bars, disks, etc. (see Chapter 4.1 and Section 5.2.1). The curvature is a non-parametric measure of the steepness of an arbitrary function (discrete or continue). As we will show, since each component in a galaxy have different steepness in $I(R)$, the curvature change significantly from one component to another.

We aim in this work to introduce the curvature looking for a way to automate the detection of different structural components in a galaxy, allowing to know how many they are and characterize them morphologically. Such concept will be helpful to other methodologies that perform multicomponent decompositions, since they need priori information (sometimes well not constrained) of what/many components are present in a given galaxy.

2.3 Specific objectives

If it is known that a galaxy is multicomponent, we should be able to extract information of each structure individually. In general lines, our parallel goals are to predict the scale length of each galactic component using the curvature. This is possible since in general each structure has a intrinsic shape in $I(R)$, therefore changes in $\tilde{\kappa}(R)$ might be related to different components. Also, we explore the shape of $\tilde{\kappa}(R)$ in each predicted region correspondent to each component, unveiling with what kind of galaxy components it is related. Anticipating some results of our work, pseudobulges, bars and rings have an intrinsic shape in $\tilde{\kappa}$, which in general are featured by narrows and negatives valleys in the values of $\tilde{\kappa}$, see for example FIGURE 17 (see also Section 5.3).

The motivation for a tool that discern muticomponents comes from a previous work we have made ([LUCATELLI; FERRARI, 2016](#)). Our premise results and still parallel to this work, is to investigate the behaviour of the concentration index C and the single-Sérsic fits calculated in multicomponent galaxies. We analyse and explain why there are galaxies with high values of C , but they are classified as spiral galaxies (see TABLE 2 and Section 3.1). The same behaviour also seems to appear in the Sérsic index (but less pronounced). For the above topics, original results have been found and will be discussed throughout the work.

These questions clearly outlines the importance of knowing if a galaxy is single or multicomponent, since a high value of C would imply in an elliptical or bulge-dominated galaxy (i.e., as far as we know, a single component) which is not in general. Therefore, the insight of the galaxy structure by a second methodology probably will avoid such misclassification.

3

MISCLASSIFICATION OF SPIRALS AND DISKS GALAXIES BY C AND n

“We are trying to prove ourselves wrong as quickly as possible, because only in that way can we find progress.”

Richard Phillips Feynman

Every methodology for morphology and structural analysis of galaxies has its own gaps. We conduct here a brief discussion of our rationale that led us to recognize how spiral and disk galaxies are misclassified by the concentration index C and the Sérsic parameter n . Also, this was our motivation to introduce a new way to recognize whether galaxies are or not multicomponent.

3.1 Effective Sérsic Index and misclassification

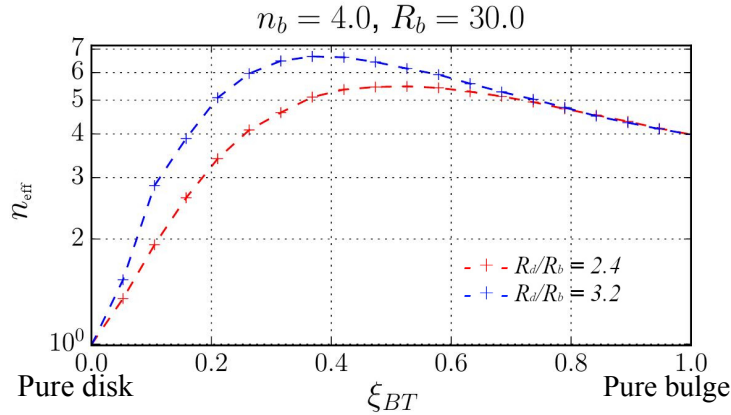
It is observed that the parameters obtained from a single fits usually are affected in systematic ways if the galaxy is multicomponent. From our comments on equation (1.6), we quantify the behaviour for the single Sérsic parameter n_{eff} . Consider FIGURE 5, where it shows the values of n_{eff} obtained for a set of simulated mock images constituted of different combinations of bulges and disks. The horizontal axis is the bulge-to-total ratio ξ_{BT} , o is a pure disk while i is a pure bulge. This quantity is given in terms of the ratio of total luminosity of bulge and disk, L_B and L_D , respectively. For example,

$$\xi_{BT} = \frac{L_B}{L_D + L_B}, \quad \xi_{DT} = \frac{L_D}{L_D + L_B}. \quad (3.1)$$

The relation between $\xi_{BD} = L_B/L_D$ and ξ_{BT} is

$$\xi_{BD} = \frac{\xi_{BT}}{I - \xi_{BT}}. \quad (3.2)$$

FIGURE 5 – Effective Sérsic index calculated for a B+D composition of simulated mock images, in terms of ξ_{BT} , with $n_b = 4$ and $R_d/R_b = 2.4$ (red) and 3.2 (blue).



Source: Adapted from [Lucatelli and Ferrari \(2016\)](#).

The vertical axis is the effective (single) Sérsic index calculated using MFMTK ([FERRARI; CARVALHO; TREVISAN, 2015](#)). For all galaxies we have used $n_b = 4$ and $R_d/R_b = 2.4$ (red) and $R_d/R_b = 3.2$ (blue). The curves indicates how the effective Sérsic parameter changes as a function of the morphology from disks to bulges. The main aspect to be noted is that there are regions where n_{eff} is smaller than n_b , but in others it is higher. The effective parameter for a pure disk coincides (naturally) with the one of a disk, $n_{\text{eff}} = n_d = 1$. However, as ξ_{BT} increases, n_{eff} also does and around $\xi_{BT} \sim 0.2$, n_{eff} becomes higher than n_b . Note that this also depends on the value of R_d/R_b – i.e. the relative width of the bulge and disk: it is higher as R_d/R_b increases. For the two cases after $\xi_{BT} \sim 0.2$, n_{eff} is always higher than $n_b = 4$. When $\xi_{BT} \rightarrow 1$, n_{eff} converge to $n_b = 4$, as expected.

This implies that a single surface photometry calculated on multicomponent galaxies may result in higher effective Sérsic parameters than if they are calculated separately to each component (in the case above the bulge). What does mean? Consider a galaxy which is not well resolved spatially and most probably to be multicomponent. A single fits would result in a high n (say, > 4). However since the components are difficult to differentiate, the final conclusion is to think that the high value of n is naturally physical. The same applies for galaxies that are forced to be single component during a fit. Since elliptical galaxies (single components, but not general) have – by nature – high values of such parameters, multicomponent ones can also be placed in the same group of elliptical because the parameters obtained from a single photometry analysis will result in such similar high n_{eff} . Furthermore, the same systematics can be present in automated procedures for large data sets, regardless of whether or not the structures are well resolved, where the images do not have a final inspection, either visually or by other methodology, to see if they are single or multicomponent.

Table 1 – Examples of galaxies with high n_{eff} supposed to be misclassified by inappropriate single Sérsic fit.

Other	PGC	Reference	n_{eff}	$n_{\text{eff}}^{\text{mfmtk}}$	Morph.
U 8237-r	45583-r	(VIKA et al., 2013)	5.11	3.50	(R)SBb
N 6314-r	59638-r	(VIKA et al., 2013)	4.79	4.87	SA(s)a

The above results seems not to be explained or discussed in other works. For example, in Vika et al. (2013, p.636), they comment that: “[...] an $n \sim 4$ bulge together with an exponential disk of similar brightness, will usually result in intermediary n for the single-Sérsic fit, e.g. $n \sim 2.5$.“ Note however that this affirmation is stated for components (bulge+disk) with similar brightness. But as discussed in our result in FIGURE 5, this is not the case, n_{eff} is smaller than 2.5 only for $\sim \xi_{BT} \lesssim 0.15$, for disk-dominated galaxies. For components of the same brightness $0.4 \lesssim \xi_{BT} \lesssim 0.6$, n_{eff} is significantly higher. From FIGURE 5, it is clear that the effective Sérsic parameter becomes a function of the intrinsic quantities of the galaxy, that is n_b , ξ_{BT} and R_d/R_b ,

$$n_{\text{eff}} = n_{\text{eff}}(\xi_{BT}, n_b, R_d/R_b). \quad (3.3)$$

In conclusion, spirals and So galaxies for example, in some cases will be misclassified as ellipticals according to what is informed by n , because both will result in similar values of n . In this purpose, we introduce in TABLE 1 some galaxies with high values of the parameter n_{eff} (according to the reference) for observed galaxies. We obtained our single Sérsic fits with MORFOMETRYKA for comparison. Note that these galaxies are not ellipticals, but spirals. In Section 5.4 we return to these galaxies analysing the curvature.

Some works that point some issues related to high effective Sérsic parameters are listed in the following lines. In Head, Lucey and Hudson (2015) they comment that for 3-component galaxies, a forced single Sérsic fits would lead to high values of n_{eff} , ~ 8 , peaking around ~ 4 . In the work made by Simard et al. (2011), their histogram (Fig. 14) clearly shows an increasing in the frequency of high values for single Sérsic indices, after ~ 7.0 . Under inspection of some of these galaxies (with high n)¹, it is not clear to say if they are multicomponent, because great part of galaxies are in low spatial resolution (as they comment). Also, the fits themselves might be affected due to this, making the high values themselves uncertain.

In Bruce et al. (2014b), they argue that high values of a single-Sérsic fit does not have preferential ξ_{BT} and depend only on the ratio between the dimensions of each component (R_d/R_b). However

¹ <<http://vizier.u-strasbg.fr/viz-bin/VizieR?-source=J/ApJS/196/11>>

this affirmation is contradictory, because: R_b and R_d are related to an having a certain area ($\propto \pi R_d^2$ and $\propto \pi R_b^2$). This area contains a certain amount of starlight, which implies in a certain luminosity, therefore the luminosities are proportional to R_d and R_b (hence to R_d/R_b). In consequence, R_d and R_b are naturally related to ξ_{BT} and ξ_{DT} . If we look again at FIGURE 5, we see that n_{eff} in fact depends on both ξ_{BT} and R_d/R_b .

In [Vika et al. \(2012\)](#) they make a comparison between different Sérsic parameters calculated for single and multiple fits of different works (with the galaxies being ellipticals and So's). Generally it seems that the single Sérsic parameters are always higher than the related parameter of the bulge (that is, for a multicomponent fit). Hence, it is in agreement with our discussion.

Next, how we are sure that these high effective values are a result of a true physical phenomena or in the worst of the cases, a result of a non physical set of parameters which does not result from a optimized convergence of the fitting? In other words, implicated by an improper use of a single Sérsic fits for a multicomponent galaxy when equation (1.5) does not hold? To explore this answer we need a quantity that is independent of model assumptions and fitting procedures. That quantity is the concentration index, since, in the same ways as n , it quantifies the concentration of light in the galaxy.

3.2 Concentration C and Misclassification

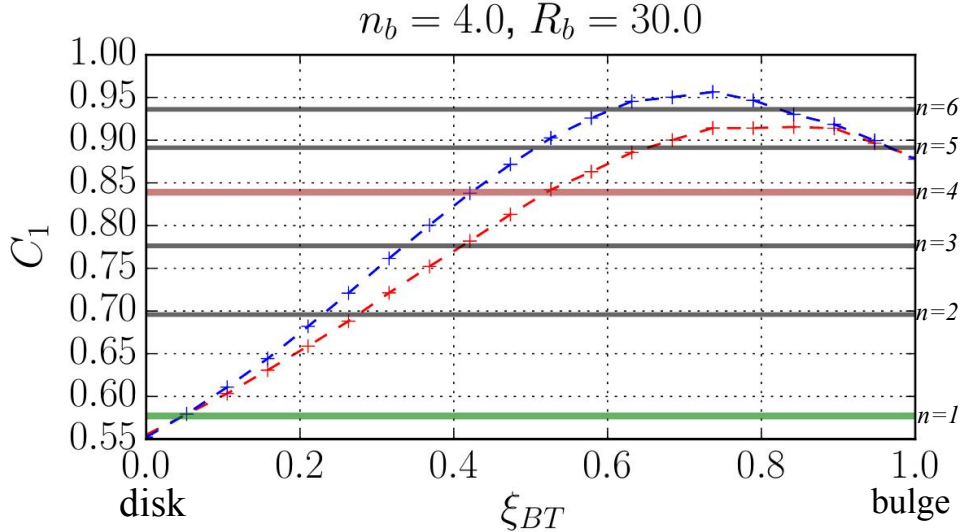
As discussed above, the question is: are high values of a single Sérsic parameter an effect related to a poor convergence of the parameters or a true physical effect of the galaxy light distribution? For inappropriate uses of a single Sérsic-fit applied to a multicomponent galaxy may lead to this effect, however in other cases (where it is possible use a single-fit with a good fitting converging) this answer remains unknown. So, we use C to explain.

Since C is a non-parametric measure, it is applicable to the majority of morphologies, therefore we inspect how C differs from multicomponent and single component galaxies, first for simulated mock images (as in FIGURE 5) and secondly for a sample of observed galaxies. Consider FIGURE 6, the values of $C_{2g} (\equiv C_i)$ are calculated from mock images from $\xi_{BT} = 0$ to $\xi_{BT} = 1$. The horizontal lines specifies the values of C_i for pure bulges, from $n = 1$ to $n = 6$ spaced one by one².

For small ξ_{BT} (disk-dominated), C_i is close to the concentration of a disk. The concentration

² Note however that at the extremes C_i does not coincides exactly with the numerical result (horizontal line) because the relation showed in FIGURE 3 is computed to a model extended to infinity, but C_i calculated by MFMTK uses truncated profiles at $2R_p$ (see equations 4.6 and 4.7).

FIGURE 6 – Similar to FIGURE 5, here we have the concentration C_i vs. the bulge-to-total ratio. Horizontal lines display the values of C_i for single Sérsic components with $n = 1, 2, 3, 4, 5$ and 6 (bottom to top, respectively). Multicomponent galaxies have increased concentration values in relation to single component ones.

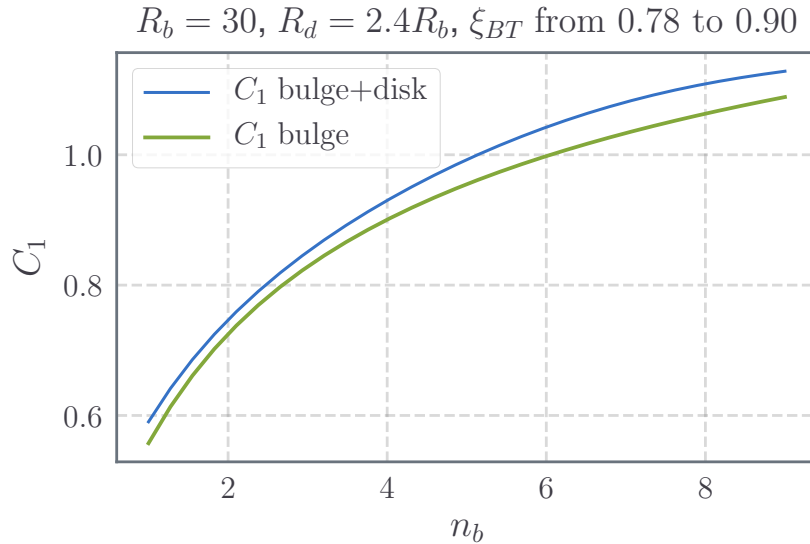


Source: Adapted from [Lucatelli and Ferrari \(2016\)](#).

coincides with the one of a $n \sim 2$ bulge for $\xi_{BT} \sim 0.25$. It is higher than a $n \sim 4$ bulge from $\xi_{BT} \sim 0.4 - 0.45$, depending on the value of R_d/R_b . After this region C_i is always higher than a single component $n \sim 4$, this demonstrates that multicomponent galaxies have increased concentration values in relation to single components ones. Additionally, the concentration of simulated B+D profiles as a function of the Sérsic parameter of the bulge n_b is presented in FIGURE 7. The purpose here is to compare C for a bulge only and a bulge perturbed by a disk. We see that all curve along n_b related to a bulge+disk (blue) combination is higher than the one related to the same bulge only. This seems to be a small contribution, however we will see next that it makes a great difference in final analysis for observed galaxies, in the same way as FIGURE 6.

These results on simulated images shows that multicomponent galaxies can have in some cases higher C than single component. Hence, this is not a fitting effect but rather a true physical consequence of the light distribution of a galaxy. To further support our findings, we extend this same analysis to observed galaxy images, exploring C of the ones that are single and multicomponent. The consequence of this is the misclassification of spiral galaxies as ellipticals. So we have sorted some galaxies with the higher concentration indices of the EFIGI sample ([BAILLARD et al., 2011](#)) for analysis (see Section 5.1 for the introduction of the data) TABLE 2 introduces these galaxies: the ones sorted for C , are in the left and for C_2 at the right. Each table contains the galaxy identification under the (N, I, U)

FIGURE 7 – Concentration index calculated for a pure bulge (with n varying) and for a bulge with the same morphology but combined with a disk. Regard that the line of C corresponding to a profile B+D is above the curve of a pure bulge, therefore multicomponents have higher concentration. Note also that, since n_b is varying (with the other parameters constants), the value of ξ_{BT} changes from 0.78 for $n_b = 1$ to ξ_{BT} for $n_b > 9$ (this is what we mean for “ ξ_{BT} from 0.78 to 0.90” in title of the figure). In conclusion we have higher C in multicomponent galaxies.



General Catalogue³ (first column), PGC Catalogue (second), the values of C_1 and C_2 (third and fourth) and the galaxy morphology according to [Vaucouleurs et al. \(1991\)](#) in the last column. Furthermore, note that the high sorted values of C_2 are also associated to higher values in C_1 (all > 0.93), the opposite also is true, but less pronounced.

As expected, the majority of the galaxies are spirals or/and multicomponent, with only a few number of ellipticals. It is exactly the effect we have explained for simulated images, which multicomponent galaxies acts to increase the value of C , making it to reaching similar values that of ellipticals. This effect appears here as an intrinsic property of C in observed galaxies. Therefore, if they are not studied with another methodology, the probability to be classified as ellipticals, rather than spirals/So etc, increases.

To be more quantitative, we display in FIGURE 8 the results of C_1 and C_2 for more than one million of galaxies of different samples (EFIGI, NA, LEGACY, LEGACY-zr) processed by [Ferrari, Carvalho and Trevisan \(2015\)](#). According to the Galaxy-Zoo classification⁴, the red lines refer to spirals and the blue to ellipticals. As it is clearly seem, there is an interval of values of C where ellipticals and spirals overlap in the histogram, which means that is there is a specific range that contains both spirals

³ N stands for NGC, I for IC and U for UGC.

⁴ <http://zoo1.galaxyzoo.org/>

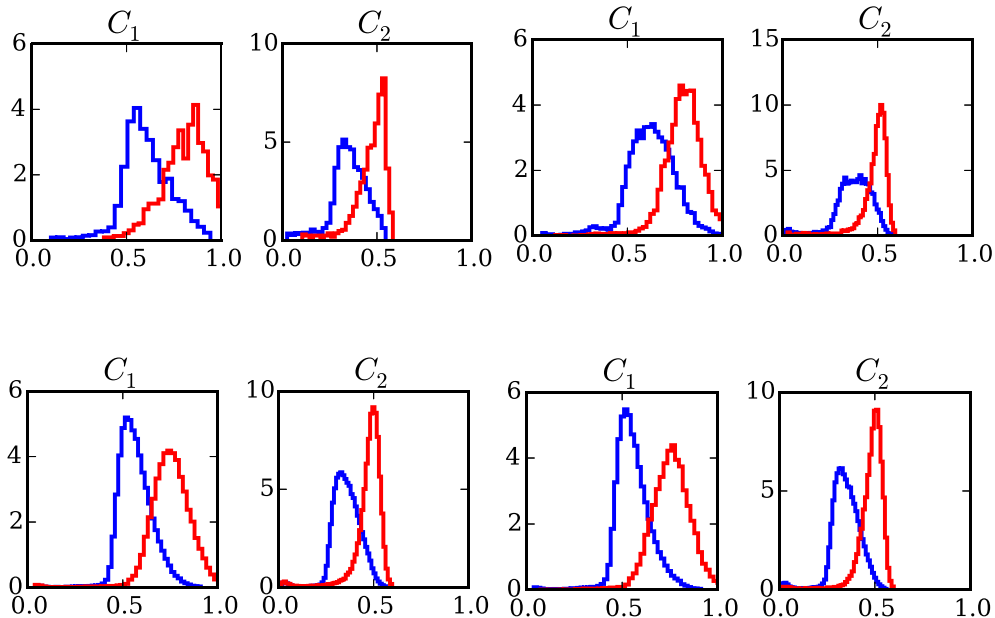
Table 2 – Some galaxies of EGIFI with the highest values in C_1 (left) and C_2 (right).

G.C.	PGC	C_1	C_2	Morph.	G.C.	PGC	C_1	C_2	Morph.
N 3032	28424	1.23	0.55	SABo(r)	U 9826	54815	0.93	0.72	SBc
U 1321	6835	1.20	0.54	So	I 1209	57796	0.99	0.65	So
N 3921	37063	1.19	0.59	(R)SAo(s)	—	57139	0.95	0.63	E
N 2681	24961	1.18	0.51	(R)SABo(rs)	I 1054	52752	1.04	0.63	So
N 7603	71035	1.15	0.57	SA(rs)	N 2599	23941	1.08	0.61	SAa
U 5432	29249	1.12	0.43	E	U 8347	46206	0.97	0.61	So
N 2599	23941	1.08	0.61	SAa	N 2880	26939	0.98	0.60	SBo
N 359	3817	1.08	0.50	So/E	N 426	4363	1.00	0.60	E/cD
N 3872	36678	1.08	0.58	E	I 708	35720	1.04	0.60	E
—	38740	1.06	0.51	cD	N 4754	43656	1.01	0.60	SBo

and ellipticals, from intermediary to high values of C . We argue that this merging of the histograms is a general extension of what we have discussed so far, and both cases are in agreement. High concentration indices are related to ellipticals and spiral galaxies, but intermediary values are also related to both spirals and ellipticals. All values of C are significantly increased, therefore the concentration index is contaminated and often misclassifying galaxies if they are not studied by a second analysis, which in here we use the curvature (see Chapter 4).

Starting from all these questions, we take it as a motivation to introduce a new way to identify the presence of multicomponents in galaxies. From our discussions, it was demonstrated that it is crucial to recognize the cases in which a given galaxy is or not multicomponent. Such knowledge is able to avoid future misclassifications, so even if a galaxy having a high C (or n) it will be known that it is multicomponent. In the next chapter we introduce the curvature of the galaxy brightness profile with the aim to differentiate different structures in a galaxy.

FIGURE 8 – Distribution of the values of $C_{28} (\equiv C_1)$ and $C_{59} (\equiv C_2)$ for a sample of galaxies processed by Ferrari, Carvalho and Trevisan (2015). Red lines refer to elliptical galaxies and blue lines refer to spiral galaxies, as classified by Galaxy Zoo. Note that the effect seen in FIGURE 6 is implicit here: elliptical and spiral can assume same values of C and because that the histograms are overlapping from ~ 0.70 for C_1 and ~ 0.4 for C_2 .



Source: Adapted from Ferrari, Carvalho and Trevisan (2015).

4

CURVATURE OF THE GALAXY BRIGHTNESS PROFILE

One prerequisite for originality is clearly that a person shall not be inclined to impose his preconceptions on the fact as he sees it. Rather, he must be able to learn something new, even if this means that the ideas and notions that are comfortable or dear to him may be overturned.

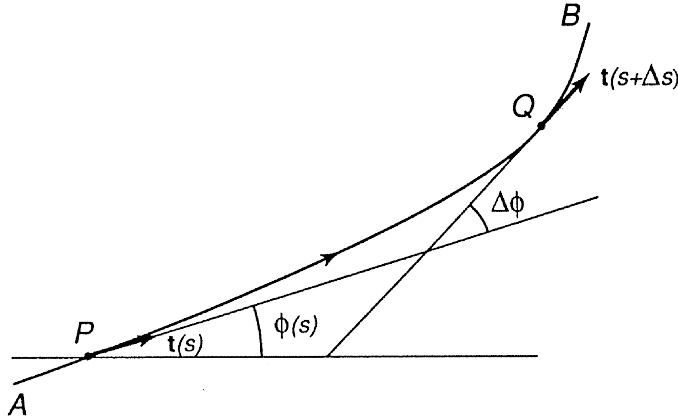
On Creativity – David Bohm

The curvature itself, as far as we know, has not been used in the context of galaxy structural analysis, nevertheless it has been used in different fields of science in a similar manner. In medicine, for example, it is used to recognize the existence of breast tumors ([LEE et al., 2015](#)), where it is applied on the imaging data of the photograph of each patient's breast in order to classify the tumors. [Luders et al. \(2006\)](#) used the curvature to study the process of brain gyration according genre, a process present on the cerebral cortex which forms folds, composed by peaks and valleys (see their methodology for details). They have used the mean curvature as a external measure of how the normal vector of the surface of the brain changes across it. The idea behind it is similar to ours, because here the curvature $\kappa(R)$ specifies how the normal vector of $I(R)$ changes along radius, giving information of what kind of component is present in each specific region of the profile. Other works using curvature were found on dental studies ([ZHANG, 2015](#); [DESTREZ et al., 2018](#)) and in general medicine ([PREIM; BOTHA, 2014](#)).

4.1 Mathematical Definitions

With the purpose to identify galaxy substructures non-parametrically we introduce the **curvature of the brightness profile** $\kappa(R)$. The concept of curvature comes from differential geometry ([TENEN-](#)

FIGURE 9 – Representation of how to measure the curvature of a path – unidimensional function. It is given in terms of how the angle ϕ changes along the parameter s of the surface in relation to two points P and Q .



Source: Adapted from [Casey \(1996\)](#).

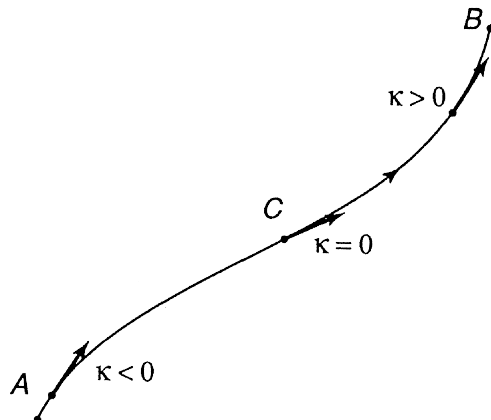
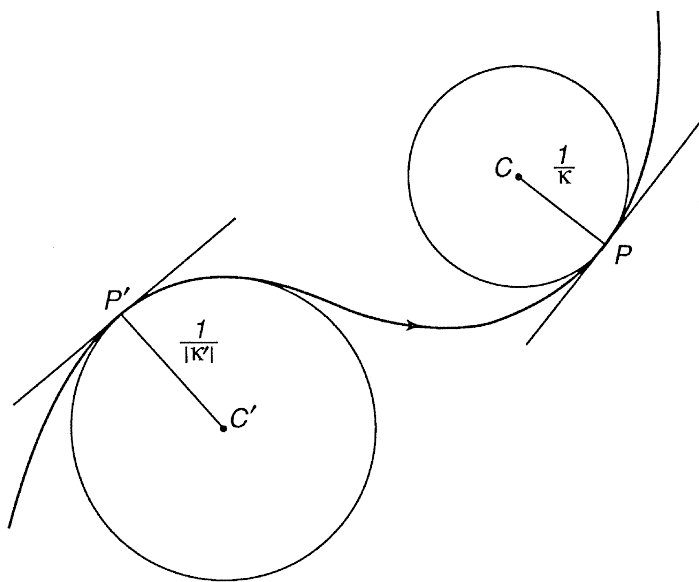
[BLAT, 2008](#)): given a function $f = f(x)$ it is possible to measure how it deviates from a straight line (the same reasoning can be extended to higher dimensional spaces) by means of a curvature measure on f , that is $\kappa[f(x)] \equiv \kappa(x)$. To clarify these concepts of curvature, consider FIGURE 9. The curve t is parametrized by the parameter s , the points P and Q represent two different locations in the curve. The normal vector \mathbf{t} of the path changes direction as we move from point P to Q , which is from $\mathbf{t}(s)$ to $\mathbf{t}(s + \Delta s)$. The difference between the normal vectors at s and $s + \Delta s$ can be represented by the variation in the angle $\Delta\phi$ where $\phi(s)$ is the angle between the end point $\mathbf{t}(s + \Delta s)$ with the horizontal direction (see the figure). It is noted that the notion of how the curve the segment is, is related to the variation of ϕ according to s , that is $\Delta\phi/\Delta s$. In fact, the curvature of the path at a point P is defined as (see for example ([CASEY, 1996](#)))

$$\kappa = \lim_{\Delta s \rightarrow 0} \frac{\Delta\phi}{\Delta s} = \frac{d\phi}{ds}. \quad (4.1)$$

The scheme demonstrating how the curvature κ changes along a parametrized curve near three points A, C and B is shown in FIGURE 10.

For completeness, a further understanding of curvature is the following. Consider that the path in which the curvature is measured is the arc length of a circle of radius \mathcal{R} , therefore $\Delta s = \mathcal{R}\Delta\phi$. Hence using this in equation (4.1) it is obtained that

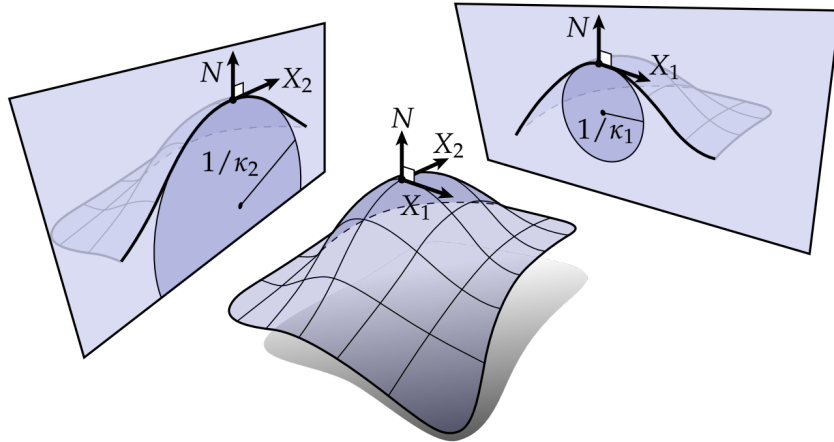
$$\kappa = \frac{I}{\mathcal{R}} \lim_{\Delta s \rightarrow 0} \frac{\Delta s}{\Delta s} = \frac{I}{\mathcal{R}}. \quad (4.2)$$

FIGURE 10 – Variation of the curvature along a path represented by three points A , C and B .Source: Adapted from [Casey \(1996\)](#).FIGURE 11 – The curvature and its associated osculating circle for a unidimensional curve. At each different point P in a path or curve, an osculating circle can be placed in which it passes through P and some of its neighbour points. The radius, and so the curvature, of this circle changes as we move to another different point P' .Source: Adapted from [Casey \(1996\)](#).

Now taking different points P along the path we can place a circle of radius $1/\kappa$ at each different one. This circle is called of **osculating circle**. Hence the radius of this circle will be the curvature of the arc length at P . For a graphical visualization, consider FIGURE 11 and FIGURE 12. In this way we can understand how curve is a function/path in terms of circles (osculating circles) passing through the neighbour points of a fixed point P .

To put these concepts in a mathematical form, lets return to the case of a unidimensional

FIGURE 12 – Similar to FIGURE 11, but extended to a bidimensional surface. \mathbf{N} stands for the normal vector at each point P .



Source: Adapted from [Crane et al. \(2013\)](#).

function $f(x)$. In this work we take $f(x)$ to be the radial brightness profile $I(R)$ of the galaxy (more details below). The curvature of I (or any other function $f(x)$) is defined by

$$\kappa(R) = \frac{\frac{d^2 I(R)}{dR^2}}{\left[1 + \left(\frac{dI(R)}{dR} \right)^2 \right]^{3/2}}. \quad (4.3)$$

Equation above is a particular case when we have a one-dimensional continuous function. However, in this work we will deal with non-continuous quantities, which are the discrete data of light profiles of the galaxies. Therefore, we seek for a discrete curvature measure on our data which involves numerical operations. For two discrete vectors representing two quantities, say I and R , the curvature is defined as

$$\kappa = \frac{\delta R_i \delta^2 I_i - \delta I_i \delta^2 R_i}{(\delta R_i^2 + \delta I_i^2)^{3/2}} \quad (4.4)$$

where δ represents the numerical differentials (derivatives) between the discrete i -values of R and I .

As commented previously, the curvature is inversely proportional to the osculating circle of radius R referent to a certain point P . This means that in any arbitrary scale, both x -axis and y -axis variables must have the same units. In other words, one variation in x need to have the same length as y (the norm of the basis vector must have the same length), consequently we can trace an osculating circle for a set of points near to a centred point P . Otherwise we would have an ellipse instead of a circle, and the curvature definition's does not hold any more, since it is not possible to drawn an osculating circle in the $x - y$ space.

This makes sense in defining the curvature of a spatial surface because x and y describes positions in that space. However, when these two quantities does not have the same physical meaning, like intensity I and radius R , some modifications are needed. Given two different quantities I and R with distinct scales, it is necessary to transform them into a space having equal metric. This is accomplished finding a normalization to the equations (4.3) and (4.4). An example of normalization is to confine both $I(R)$ and R to vary in an equal interval, for example the unitary one $[0, 1]$.

Before we proceed to the normalization, there is a particular result from the curvature for we should take into account: it is zero for a straight line and non zero for other general cases. A galactic disk generally follow an exponential profile (FREEMAN, 1970), see equation (1.3). Then in log space, this profile is a straight line and we can conclude that the curvature of a disk in log space is close to zero. With this in mind we argue that is more useful to normalize the logarithm of $I(R)$, $\log[I(R)]$, instead of $I(R)$. Our point is that we will be able to easily distinguish disks from non disks using $\tilde{\chi}$. Hence a normalization $\nu(R)$ for $\log[I(R)]$ in the range $[0, 1]$ is

$$\nu(R) \equiv \frac{\log[I(R)] - \min(\log I)}{\max(\log I) - \min(\log I)}. \quad (4.5)$$

The next step is the normalization for R . We need to change the variation of the dimensional variable R to another quantity that is dimensionless and confine it in the range $[0, 1]$. Generally, observations do not reach the faintest parts of a galaxy, so it is usual to define a galaxy size. One common choice is the Petrosian radius R_p (PETROSIAN, 1976), defined by the radius where the Petrosian function

$$\eta(R) = \frac{\langle I \rangle(R)}{I(R)} \quad (4.6)$$

has a definite value, i.e.

$$\eta(R_p) = \eta_o. \quad (4.7)$$

Here $\langle I \rangle(R)$ is the mean intensity inside R and $I(R)$ the intensity at R . Following (BERSHADY; JAN-GREN; CONSELICE, 2000; BLANTON et al., 2001; FERRARI; CARVALHO; TREVISAN, 2015) we use here $\eta_o = \zeta$ with $2R_p$ as the size of galaxy. The normalization of R now reads

$$\chi = \frac{R}{2R_p}. \quad (4.8)$$

The curvature in terms of normalized variables measures the rate of change of $\nu(R)$ in terms of the new variable χ . So the complete normalized curvature is obtained taking the derivative of $\nu(R)$ with respect to χ . The relationship between the differentials of dR and $d\chi$ is

$$d\chi = \frac{dR}{2R_p}. \quad (4.9)$$

With

$$\frac{d\nu}{d\chi} = {}_2R_p \frac{d\nu}{dR} \quad \text{and} \quad \frac{d^2\nu}{d\chi^2} = {}_4R_p^2 \frac{d^2\nu}{dR^2} \quad (4.10)$$

we obtain the **normalized curvature** as

$$\tilde{\kappa}(R) = {}_4R_p^2 \frac{d^2\nu}{dR^2} \left[I + {}_4R_p^2 \left(\frac{d\nu}{dR} \right)^2 \right]^{-3/2}. \quad (4.11)$$

We will use expression (4.11) in Section 4.2 to derive the curvature for a Sérsic profile.

Returning to the discrete case in Eq. (4.4), the discrete normalized curvature in terms of the new variables is

$$\tilde{\kappa} = \frac{\delta\chi_i \delta^2\nu_i - \delta\nu_i \delta^2\chi_i}{(\delta\chi_i^2 + \delta\nu_i^2)^{3/2}}. \quad (4.12)$$

As an example, Figure FIGURE 14 shows $\tilde{\kappa}$ measured for the EFIGI galaxy NGC 1211/PGC 11670 (see Section 4.4), together with the normalized profile $\nu(R)$ and the related derivatives of $\nu(R)$ (raw and filtered, see Section 4.4) used to calculate the curvature (details will be given later in Section 4.5).

The rationale behind using the brightness profile curvature $\tilde{\kappa}$ to identify structural subcomponents in galaxy light is based on the fact that the curvature of disks will be null whilst that of bulges will be positive and dependent on its Sérsic index; regions highly affected by the PSF would tend to be negative in $\tilde{\kappa}$; the transition between different components would be manifested in curvature changes; galaxies with disks (either inner or outer) will present $\tilde{\kappa}$ that are zero over the region dominated by the disk (see next section).

In the next subsections, we develop a detailed understanding on how $\tilde{\kappa}$ behaves for different combinations of galaxy subcomponents. In Section 4.5 we initialize this study using $\tilde{\kappa}$ with a detailed analysis to galaxies NGC 1211 and NGC 1357, respectively. In Section 5.2.1 we extend the analysis to all galaxies of our selected sample, TABLE 3.

4.2 Curvature of a Sérsic Law

Here we derive the curvature of a Sérsic law for a single component. As commented, to remove the scale on I , we use the normalization given in (4.5). Taking the logarithm of equation (1.3) we have

$$\nu(R) \equiv \log I(R) = \log I_n + b(n) \left[I - \left(\frac{R}{R_n} \right)^{1/n} \right]. \quad (4.13)$$

Since we consider galaxies extending up to $2R_p$, the maximum and minimum are at $R = o$ and $R = 2R_p$, respectively, hence

$$\max \log I = I(o) = \log I_n + b(n) \quad (4.14)$$

$$\min \log I = I(2R_p) = \log I_n + b_n \left[I - \left(\frac{2R_p}{R_n} \right)^{1/n} \right] \quad (4.15)$$

thus, inserting these into (4.5) gives

$$\nu(R) = I - \left(\frac{R}{2R_p} \right)^{1/n}. \quad (4.16)$$

This result is independent of I_n and R_n because of the normalization on I and on R . The first and second derivative are

$$\frac{d\nu(R)}{dR} = -\frac{I}{2R_p n} \left(\frac{R}{2R_p} \right)^{\frac{1-n}{n}} \quad (4.17)$$

$$\frac{d^2\nu(R)}{dR^2} = \frac{n-I}{4R_p^2 n^2} \left(\frac{R}{2R_p} \right)^{\frac{1-2n}{n}}. \quad (4.18)$$

Using these two result in equation (4.11) we obtain the normalized single Sérsic curvature:

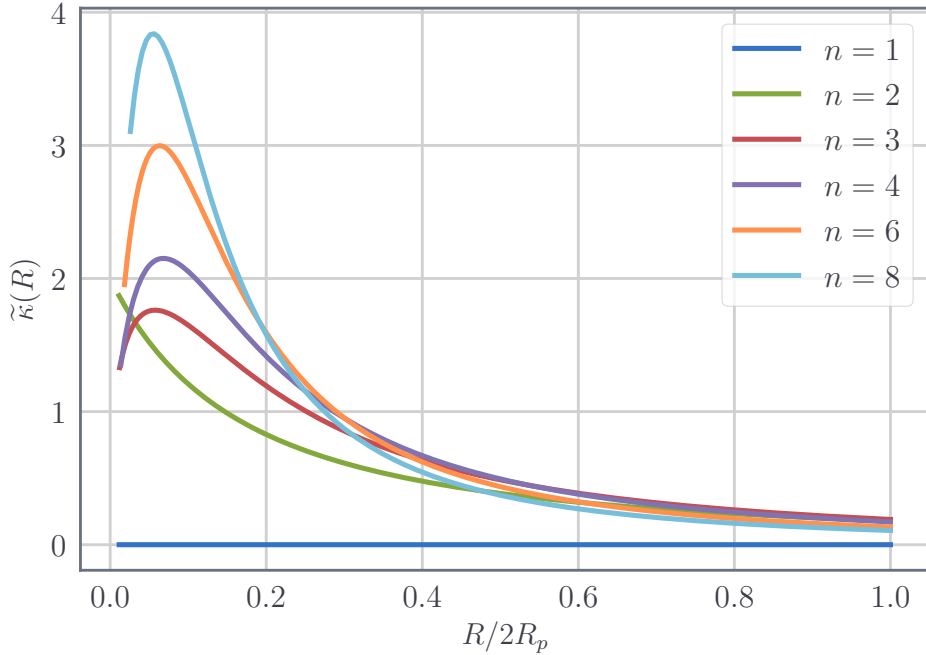
$$\tilde{\kappa}(R) = \frac{n-I}{n^2} \left(\frac{R}{2R_p} \right)^{\frac{1-2n}{n}} \left[I + \frac{I}{n^2} \left(\frac{R}{2R_p} \right)^{\frac{2-2n}{n}} \right]^{-3/2} \quad (4.19)$$

FIGURE 13 shows plots of (4.19) for different values of n against the normalized variable $\chi = R/(2R_p)$. For a disk, which frequently follows an $n = 1$ law, we obtain that $\tilde{\kappa} = o$ because the numerator vanishes. For $n > 1$, $\tilde{\kappa}$ is correlated to n , the higher the n the higher the curvature (in the inner regions), for outer regions the Sérsic law becomes more flat and $\tilde{\kappa}$ behaves a disk.

4.3 Measuring $I(R)$ with MORFOMETRYKA

The brightness profile is measured as part of the processing done by MORFOMETRYKA ([FERRARI; CARVALHO; TREVISAN, 2015](#)). MORFOMETRYKA is an algorithm designed to perform several photometric and morphometric measurements on a galaxy image in an automated way with no user interaction. The inputs are the galaxy image stamp and respective point spread function (PSF) image. It then measures the background in an iterative way, segmentates the image – separating galaxy, other objects and background – and measure basic geometric parameters of the segmented region, like the centre, the position angle, major and minor axis. Based on this information, it performs aperture

FIGURE 13 – Plots of Equation (4.19) for different Sérsic indices. The higher is n , the higher is $\tilde{\kappa}$ in the inner regions, which is reasonable because high n represent inner components. Note that for large R , the $\tilde{\kappa}$ profiles are similar.



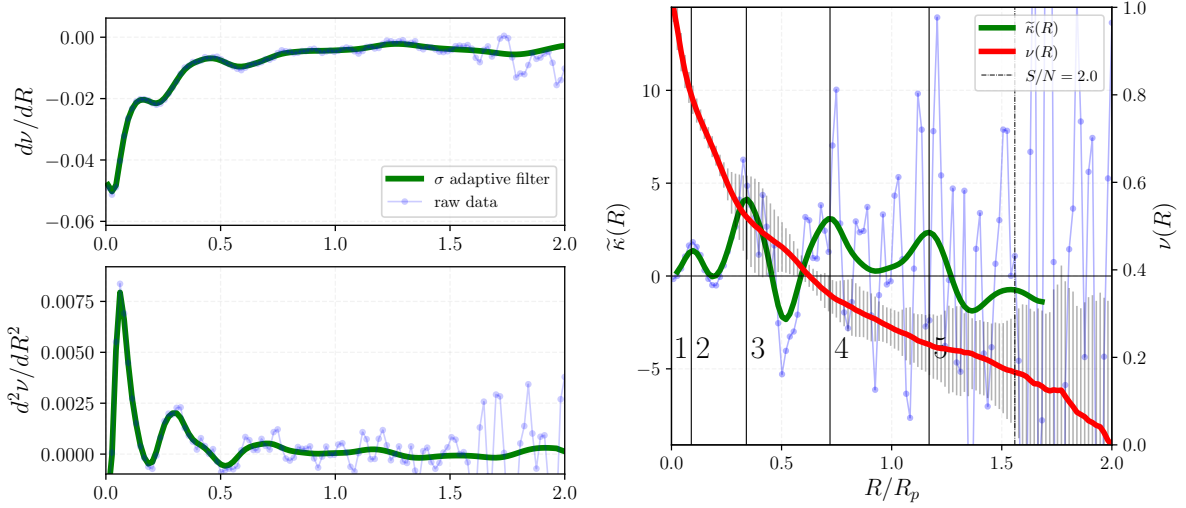
photometry on similar ellipses from the centre up to $2 R_p$ (the Petrosian radius), spaced 2 pixel apart and having the width of 1 pixel. The brightness profile $I(R)$ is the azimuthally averaged value of the ellipses aforementioned; the error is the standard deviation of the same pixel set.

4.4 Filters for $\tilde{\kappa}$

Measuring the curvature, according to Eq. (4.3), would be just a matter of evaluating the first and second derivatives of the brightness profile. In practice, with discrete points for $I(R)$ contaminated by noise, the direct estimation of $d\nu/dR$ and $d^2\nu/dR^2$ are worthless because the noise in $I(R)$ is amplified by the derivative operator (a high pass filter). FIGURE 14 shows this noise magnification that yield a very scattered curvature (blue points).

One way to overcome the limitations imposed by the noise is to use a filter to enhance the signal-to-noise of the data. Many linear filters attenuate the signal as well as the noise. For our purpose, we need a filter that attenuates the noise but keeps the overall structure present in the data. In general, the signal-to-noise ratio is higher in inner regions of the galaxy data and decreases to outermost regions. Therefore, the best solution to use in the filtering task is an adaptive filter, which takes into account

FIGURE 14 – Example of the procedure to calculate $\tilde{\kappa}(R)$ for the EFIGI/SDSS data of galaxy NGC 1211/PGC 11670. **Left Top:** first derivative of $I(R)$, raw (blue) and filtered (green). **Left Bottom:** the same but for the second derivative of $I(R)$. **Right:** log-normalized brightness profile $\nu(R)$ (red) and the raw (blue) and filtered (green) curvature. The solid vertical lines represent the possible transition between regions dominated by different components, and will be explained latter on Section 4.5. The vertical dashed line delimit the regions where the signal-to-noise S/N goes below 2 and we avoid to interpret profiles outside that region.



the level of the dispersion and adapts the level of the smoothing accordingly.

We adopt a simple adaptive Gaussian filter G , which changes the Gaussian dispersion σ according to the local signal to noise ratio. We write a linear relation between σ and the radial distance R , assuming that inner regions are less noisy and constituted by small structures, and outer regions, more noisy and large structures, which is true for the majority of galaxies. We then write

$$\sigma(R) = (\sigma_{\max} - \sigma_{\min}) \frac{R}{2R_p} + \sigma_{\min} = (\sigma_{\max} - \sigma_{\min}) \chi + \sigma_{\min} \quad (4.20)$$

where σ_{\min} is the standard deviation of the filter at the centre of the data and σ_{\max} in the outermost region. Generally $\sigma_{\min} \lesssim 2$ and $\sigma_{\max} \sim 0.1 \times (2R_p)$. We performed tests with this design and verified that a single step of filtering in $\nu(R)$ is enough to remove effectively the noise from the data; to overcome edge effects caused by the filter when smoothing points at the edges, we discard the points corresponding to $2\sigma_{\min}$ at the beginning and $2\sigma_{\max}$ and the end of $\tilde{\kappa}$. – note that the green line of $\tilde{\kappa}(R)$ in FIGURE 14 ends at $R/R_p \sim 1.7$.

4.5 Case Studies

In this Section we introduce in practice how to use $\tilde{\kappa}(R)$ for structural analysis.

Curvature of NGC 1211

We begin by analysing the $\tilde{\kappa}$ and components for galaxy NGC 1211 (PGC 11670) of the EFIGI sample. NGC 1211 is classified as (R)SB(r)o/a ([VAUCOULEURS et al., 1991](#)), i.e. barred spiral/lenticular with rings. In [FIGURE 15](#) it is shown the SDSS galaxy r image (top left), the residual from a single Sérsic fit by [MORFOMETRYKA](#) (top right) and the curvature $\tilde{\kappa}$ on the bottom. The behaviour of $\tilde{\kappa}$ is related to the transition between regions dominated by different components. In the galaxy image on the top panel, the size of the yellow dotted lines overlaid were determined by the local peaks in the curvature plot (bottom), signalled as vertical solid lines. They delimit the regions (identified by the labels) that are dominated by different components.

Starting from the central region, we have two local peaks in $\tilde{\kappa}$ at $R/R_p \sim 0.1$ and $R/R_p \sim 0.3$. The region inside the first peak (label 1) seems to be a small structure inside the bulge which is represented by region 2. However, both components have small values in curvature compared to the maximum amplitude (at $R/R_p \sim 0.4$), the bulge in region 2 reaches values close to zero, therefore this indicates that the Sérsic index of this component is close to 1 (this can also be seen by the straight brightness profile in the region – red curve in bottom plot). This may indicate that the bulge of NGC 1211 is a pseudobulge. Note also that the component in the innermost region also has a small $\tilde{\kappa}$. In [Méndez-Abreu et al. \(2017\)](#) they comment that NGC 1211 has an internal structure called “barlenses”, which is a component different of a bulge contained inside the bar ([LAURIKAINEN et al., 2010](#)). [Gadotti et al. \(2007\)](#) also observed a nuclear structure in this galaxy. Therefore, the signature in $\tilde{\kappa}$ in regions 1 and 2 are not of a classical bulge, but indicate the presence of the nucleus and a pseudobulge.

The second peak at $R/R_p \sim 0.3$ is the transition between the bulge with the bar+inner ring – a narrow and negative valley in $\tilde{\kappa}$. Usually bars and inner rings are associated with narrow valleys in $\tilde{\kappa}$. For inner rings they are negative and for bars they can be negative or not, however in general both have narrow valleys. The third peak at $R/R_p \sim 0.75$ defines the end of the bar and the start of the outer region of the galaxy, label 4 and 5. The transition $4 \rightarrow 5$ is indicated by the local peak at $R/R_p \sim 1.2$. The intermediate regions of 4 shows $\tilde{\kappa} \sim 0$ regarding a disk like structure. As indicated by [Buta \(2013\)](#), NGC 1211 has two outer rings, the inner outer is red and the outer outer blue (see his Figure 2.30).

FIGURE 15 – Top Left: SDSS r image for NGC12II from the EFIGI sample. The yellow lines represent each component of the galaxy. These regions were drawn from the local peaks in the green line of $\tilde{\kappa}(R)$ (see below). The numbers in the yellow ellipses and in the $\tilde{\kappa}$ plots refer to the same regions. **Top Right:** Residual from a single Sérsic fit to the image above made with MORFOMETRYKA. For both, yellow dotted lines correspond to regions identified in the curvature plot below; yellow dot-dashed line is the $2R_p$ region. **Bottom:** Normalized log-brightness profile (red curve) and curvature $\tilde{\kappa}$ calculated from it (green curve). The solid vertical lines delimit regions of different components (see text for details). The vertical dashed line is the limit of confidence of $\text{SNR}=2$.

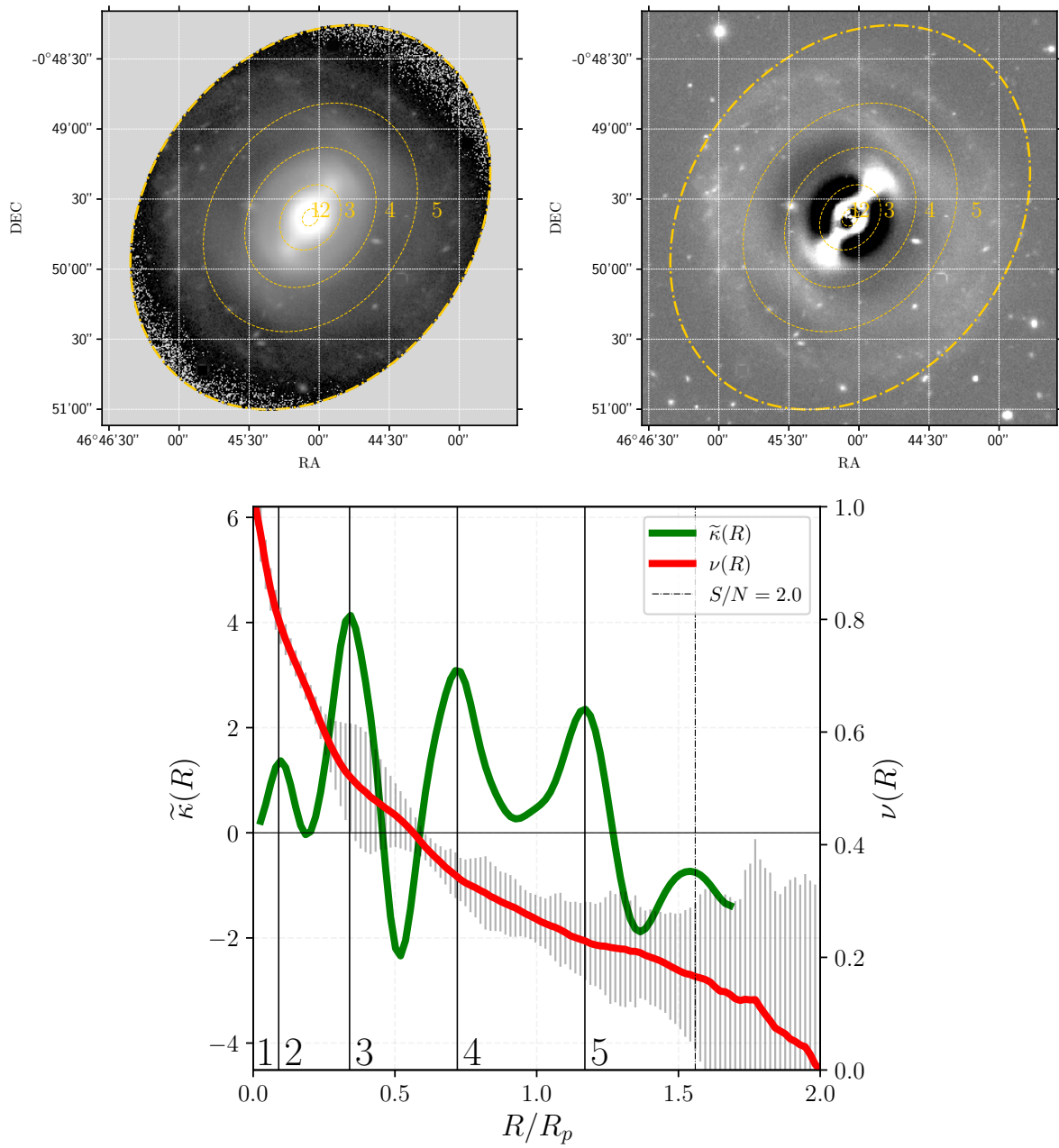
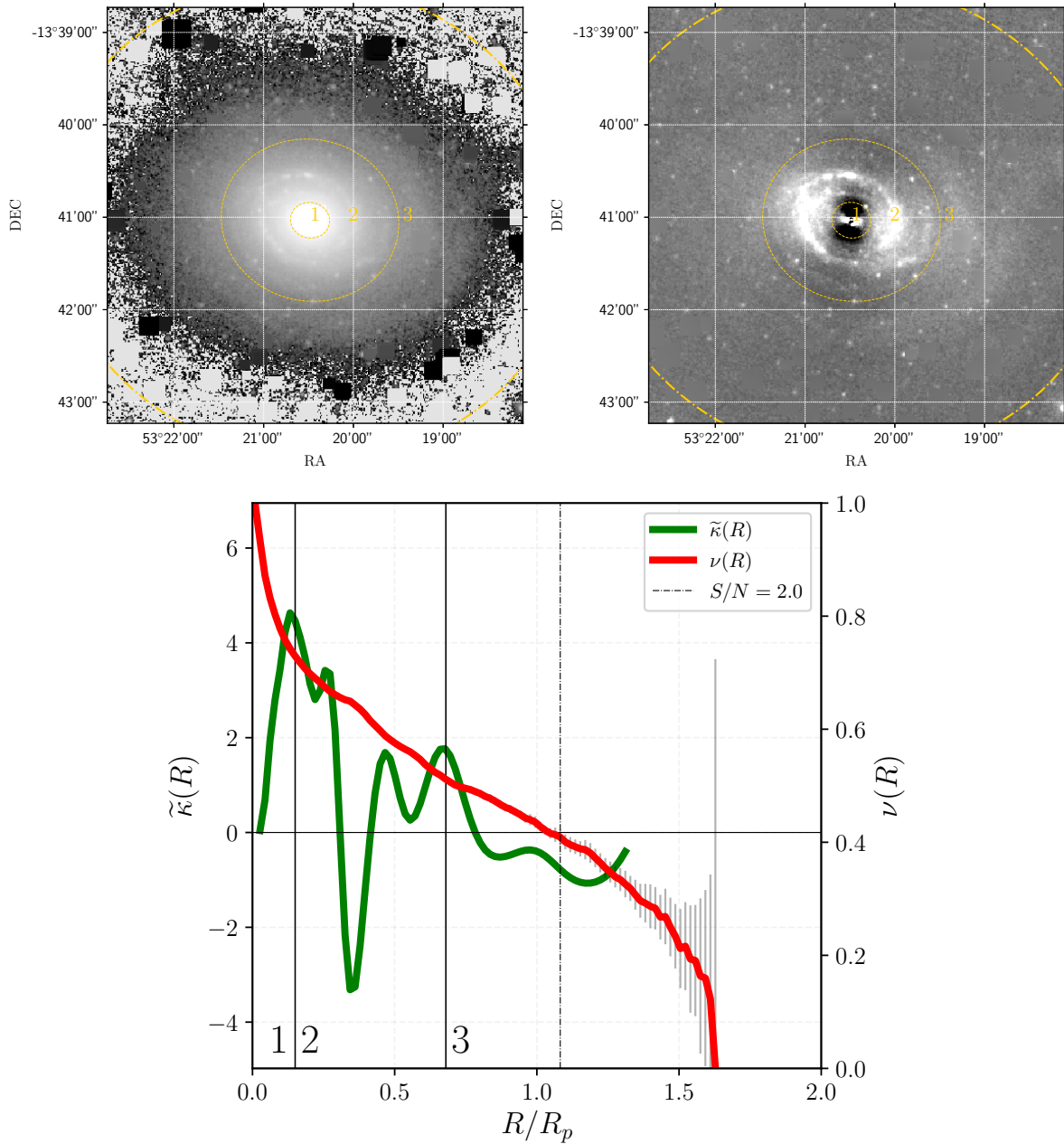


FIGURE 16 – Near infrared band ($3.6\mu\text{m}$) of NGC 1357 from Spitzer telescope. Labels and graphic positions are the same as FIGURE 15, and the same for the remaining figures. Region 1 is the bulge (high and large peak in $\tilde{\kappa}$). Region 2 is the disk with spiral arms and the outer disk is region 3 with low values in curvature. Again, the dashed vertical line ($\text{SNR}=2$) is our limit of confidence. See the text for further details of this galaxy.



Curvature of NGC 1357

NGC 1357 is a non-barred spiral galaxy classified as SA(s)ab ([VAUCOULEURS et al., 1991](#)). [Gao and Ho \(2017\)](#) considered that the galaxy has two disks: an inner blue disk which contains well defined spiral arms, and an outer red disk with no spiral arms. [FIGURE 16](#) shows the curvature for NGC 1357.

The bulge is indicated by the region of high curvature (1); the valley at (2) is related to the tight shape of the spiral arms, having a ring-like shape. The valley in $\tilde{\chi}$ is an evidence of the ring structure, pointed out by [Li et al. \(2011\)](#), [Gao and Ho \(2017\)](#). We found that a high and narrow negative gradient in curvature is characteristic of ring and bar components – which corresponds to Sérsic index lower than unity. The transition of this ring with the spiral structure corresponds to the middle inwards part of region 2. However, all spiral structure is contained inside region 2 which is the inner disk.

The transition between the inner and the outer disk is underpinned by the decrease in the oscillations after the local peak at $R/R_p \sim 0.65$, therefore region 3 corresponds to the outer disk with no spiral arms. As mentioned before, a disk has values of $\tilde{\chi}$ close to zero. In Chapter 5, we extend the same analysis for the rest of the sample, separating them according to each morphological type.



RESULTS & DISCUSSIONS

“There is no good in anything until it is finished.”

Temüjin (Genghis Khan)

5.1 Data

The main data¹ in the present study is constituted by galaxies that already have been studied in terms of structural decompositions and multicomponent analysis. We have selected galaxies contained in the following works (WOZNIAK; PIERCE, 1991; PRIETO et al., 2001; CABRERA-LAVERS; GARZÓN, 2004; LAUER et al., 2007; GADOTTI et al., 2007; GADOTTI, 2008; GADOTTI, 2009; COMPÈRE; LÓPEZ-CORREDOIRA; GARZÓN, 2014; SALO et al., 2015; GAO; HO, 2017; YILDIRIM et al., 2017) (individual references bellow). The imaging data were extracted according to their availability in NED and other databases. These are: EFIGI survey (BAILLARD et al., 2011), Hubble Space Telescope Archive (HLA²), SPITZER Telescope (DALE et al., 2009), Pan-STARRS-I telescope³ (CHAMBERS et al., 2016) and Cerro

¹ The main data refers to the galaxies that we will conduct a detailed analysis with $\tilde{\chi}(R)$. For any other complementary data, information about will be given in the moment they are used, for example, TABLE 1 and TABLE 2.

² Based on observations made with the NASA/ESA Hubble Space Telescope, and obtained from the Hubble Legacy Archive, which is a collaboration between the Space Telescope Science Institute (STScI/NASA), the Space Telescope European Coordinating Facility (ST-ECF/ESA) and the Canadian Astronomy Data Centre (CADC/NRC/CSA).

³ The Pan-STARRS1 Surveys (PS1) and the PS1 public science archive have been made possible through contributions by the Institute for Astronomy, the University of Hawaii, the Pan-STARRS Project Office, the Max-Planck Society and its participating institutes, the Max Planck Institute for Astronomy, Heidelberg and the Max Planck Institute for Extraterrestrial Physics, Garching, The Johns Hopkins University, Durham University, the University of Edinburgh, the Queen’s University Belfast, the Harvard-Smithsonian Center for Astrophysics, the Las Cumbres Observatory Global Telescope Network Incorporated, the National Central University of Taiwan, the Space Telescope Science Institute, the National Aeronautics and Space Administration under Grant No. NNX08AR22G issued through the Planetary Science Division of the NASA Science Mission Directorate, the National Science Foundation Grant No. AST-1238877, the University of Maryland, Eotvos Lorand University (ELTE), the Los Alamos National Laboratory, and the Gordon and Betty Moore Foundation. <<https://outerspace.stsci.edu/display/PANSTARRS/Pan-STARRS+data+archive+home+page>>

Tololo Inter-American Observatory 0.9m (CTIO 0.9m) telescope⁴.

TABLE 3 introduces the following information for each galaxy: the complete references, where the data was taken, the filter used and the morphological classification found in the literature. Most of galaxies are in the *r* band, corresponding to a wavelength around 6250 angstroms. NGC 4251 is in the *i* band, with a wavelength around of 7760 angstroms. For the HST images we have the filter f160w, which corresponds to the *H* band with a wavelength peak of 1.545 microns⁵. For the Spitzer galaxies, the filter correspond to the IRAC3.6 band with a wavelength around of 3.6 microns.

We have limited our study to a small set of 16 galaxies in order to lead a careful analysis with curvature. We selected galaxies in each general morphology: ellipticals, lenticular, disk/spiral (with and without bar). The sample cover the following diversity:

1. galaxies with complex structure, e.g. bars, rings, arms, disks, which are notably seem: NGC 1211 (BUTA, 2013), NGC 0936 (WOZNIAK; PIERCE, 1991), NGC 1512 (LAURIKAINEN et al., 2006; COMPÈRE; LÓPEZ-CORREDOIRA; GARZÓN, 2014), NGC 2967, NGC 7723 (PRIETO et al., 2001);
2. galaxies with fine structures, e.g. core, smooth bars or arms + So galaxies with smooth disks which barely can be identified: NGC 0384 (YILDIRIM et al., 2017), NGC 1052 (LAUER et al., 2007), NGC 2767 (NAIR; ABRAHAM, 2010; YILDIRIM et al., 2017), NGC 4251 (WOZNIAK; PIERCE, 1991; MOLAEINEZHAD et al., 2017), NGC 4267 (WOZNIAK; PIERCE, 1991), NGC 1357 (LI et al., 2011; GAO; HO, 2017), NGC 2273 (CABRERA-LAVERS; GARZÓN, 2004), NGC 6056 (TARENghi; GARILLI; MACCAGNI, 1994; PRIETO et al., 2001);
3. galaxies with well known structure in shape, for example ellipticals: NGC 472, NGC 1270 (YILDIRIM et al., 2017);

With this set we investigate the behaviour of $\tilde{\kappa}(R)$ for each representative galaxy morphology, recognizing how the curvature differs between each type.

5.2 Analysis of $\tilde{\kappa}$ for individual galaxies

Now we will study the behaviour of $\tilde{\kappa}(R)$ for galaxies presented in TABLE 3 with the aim of distinguishing galaxy multicomponents and decipher different morphologies. Each galaxy in our sample

⁴ <http://www.ctio.noao.edu/noao/>.

⁵ http://www.stsci.edu/hst/wfc3/ins_performance/ground/components/filters.

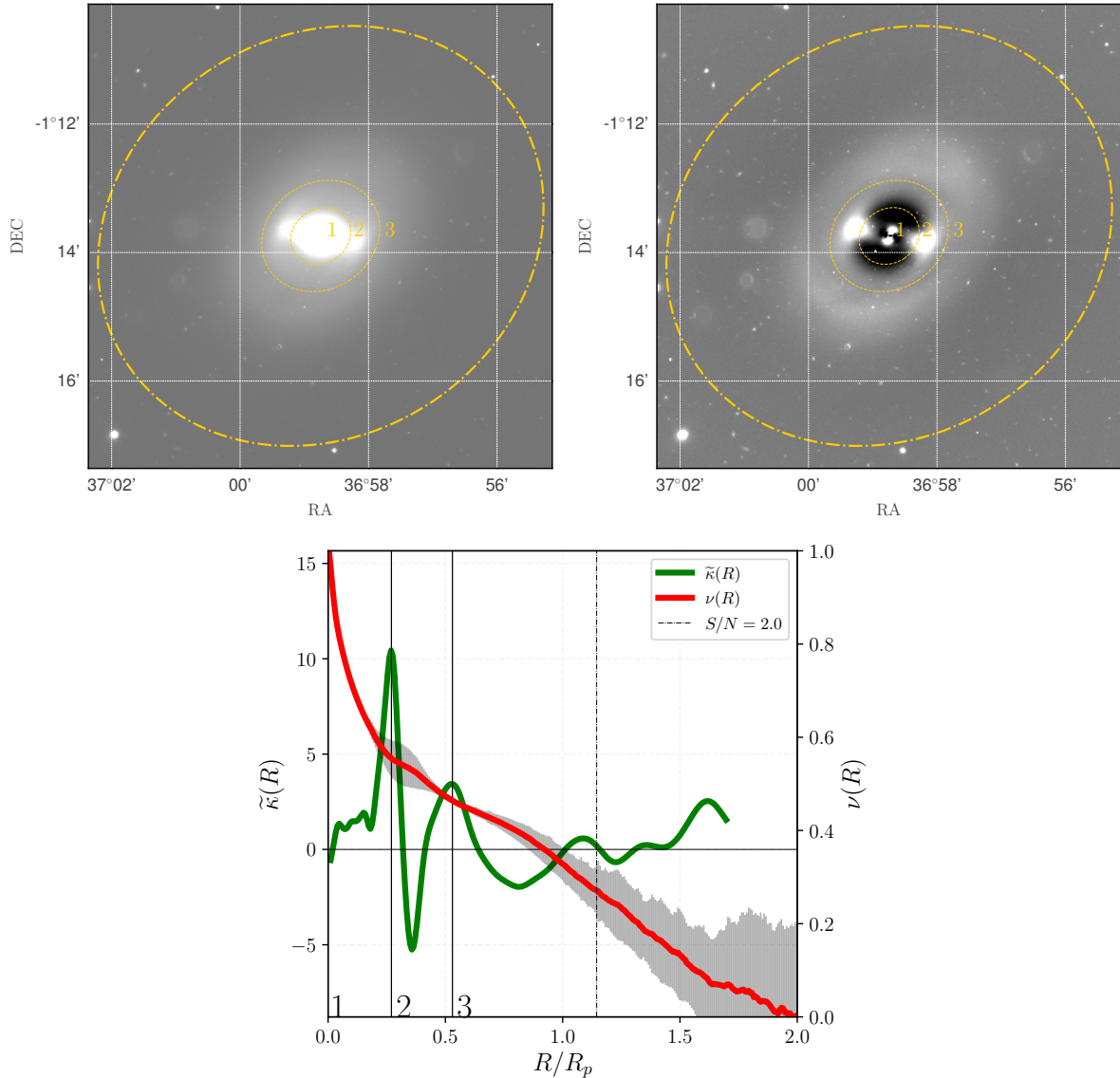
Table 3 – Data sample used in this work.

<i>i</i>	Galaxy Name + filter	Morphology	Origin	Reference of the data
1	NGC0384-f16ow	So ³ /E ^{1,2}	HST	(YILDIRIM et al., 2017)
2	NGC0472-f16ow	VY CMPT ²	HST	(YILDIRIM et al., 2017)
3	NGC0936- <i>r</i>	SBo ⁴	EFIGI	(BAILLARD et al., 2011)
4	NGC1052- <i>r</i>	E ^{1,5} (+core ⁶)/So ⁵	EFIGI	(BAILLARD et al., 2011)
5	NGC1211- <i>r</i>	SBo/a(r) ⁷	EFIGI	(BAILLARD et al., 2011)
6	NGC1270-f16ow	E'/VY CMPT ²	HST	(YILDIRIM et al., 2017)
7	NGC1357-3.6μm	SA(s)ab ¹	SPITZER	(DALE et al., 2009; SHETH et al., 2010)
8	NGC1512- <i>r</i>	SB(r)a ¹	CTIO	(MEURER et al., 2006)
9	NGC2273- <i>r</i>	SB(r)a ¹	Pan-STARRS	(CHAMBERS et al., 2016)
10	NGC2767- <i>r</i>	E'/So ⁸	HST	(YILDIRIM et al., 2017)
11	NGC4251- <i>i</i>	SBo ⁴	SDSS-drII	(ALAM et al., 2015)
12	NGC4267- <i>r</i>	So ³ /SBo ^{4,5}	EFIGI	(BAILLARD et al., 2011)
13	NGC4417- <i>r</i>	SAoa ⁹	EFIGI	(BAILLARD et al., 2011)
14	NGC4452- <i>r</i>	SB(l)oc ⁹	EFIGI	(BAILLARD et al., 2011)
15	NGC6056- <i>r</i>	SB(s)o ^{1,10} /So/a ¹¹	EFIGI	(BAILLARD et al., 2011)
16	NGC7723-3.6μm	SB(r)b ^{1,10}	SPITZER	(DALE et al., 2009; SHETH et al., 2010)

¹ (VAUCOULEURS et al., 1991).² (YILDIRIM et al., 2017).³ (NILSON, 1973).⁴ (WOZNIAK; PIERCE, 1991).⁵ (SANDAGE; TAMMANN, 1981).⁶ (LAUER et al., 2007).⁷ (GADOTTI et al., 2007).⁸ (NAIR; ABRAHAM, 2010).⁹ (KORMENDY; BENDER, 2012).¹⁰ (PRIETO et al., 2001).¹¹ (TARENghi; GARILLI; MACCAGNI, 1994).

will be discussed individually in separated sections, divided by their global morphologies, e.g. lenticular (Section 5.2.1), spirals (Section 5.2.2) and ellipticals/spheroidal components (Section 5.2.3). The procedure of study for the rest of galaxies of TABLE 3 will be the same as Section 4.5. For each galaxy (see the model reference FIGURE 15), we present the broad band image of the galaxy in the top left panel. In the top right panel we show the residual map from a single Sérsic fit to the broad band image made with MORFOMETRYKA – for the structures are easily visualized on it. For both, yellow dotted lines correspond to regions identified in the curvature plot and yellow dot-dashed line mark the zR_p region. The bottom panel shows the normalized brightness profile $\nu(R)$ (red curve – scale in the axis at right) and curvature $\tilde{\chi}(R)$ calculated from it (green curve – scale on axis at left). The solid vertical lines delimit regions of different components (discussed below for each galaxies); they correspond to the yellow ellipses in the images, but are inferred from the $\tilde{\chi}$ behaviour. Vertical dashed line is the limit of confidence of $\text{SNR} = 2$.

FIGURE 17 – The same as FIGURE 15, but for r band of NGC 936 from EFIGI. See text for details.

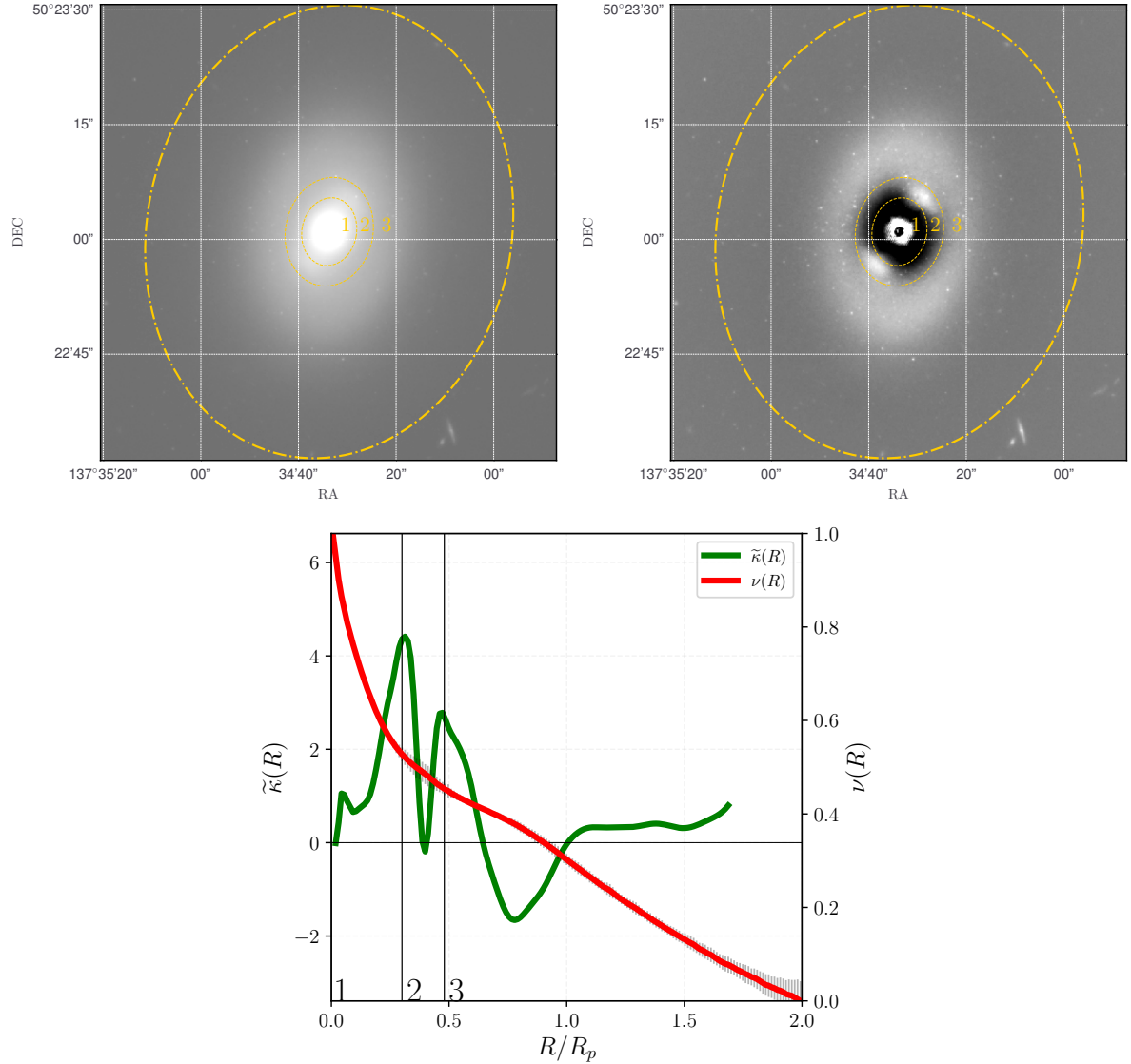


5.2.1 Lenticular Galaxies

NGC 936

NGC936 is classified as barred lenticular galaxy SBo (WOZNIAK; PIERCE, 1991), formed by a structure of bulge+bar+disk. In FIGURE 17 we infer from $\tilde{\kappa}$ that the bulge dominates region 1, while the bar becomes dominant in region 2 – indicated by the strait valley and negative $\tilde{\kappa}$. It ends close to $R/R_p \sim 0.5$. Bar properties were also extracted by Muñoz-Mateos et al. (2013), regarding the bar length. The peak in $\tilde{\kappa}$ at $R/R_p \sim 0.5$ indicating the end of the bar seems to be in agreement with the outer limit found by the authors (see their figure 3). The bar of NGC 936 was also studied by Erwin and Sparke (2003) together

FIGURE 18 – The same as FIGURE 15, but for NGC 2767 from HST (f160w).



with a nuclear ring inside the bar region. Returning back to the inner component, $\tilde{\kappa}$ is nearly constant and ~ 1 . This suggest that the inner region is not a classical bulge, rather being a pseudobulge, which also contains a nuclear ring.

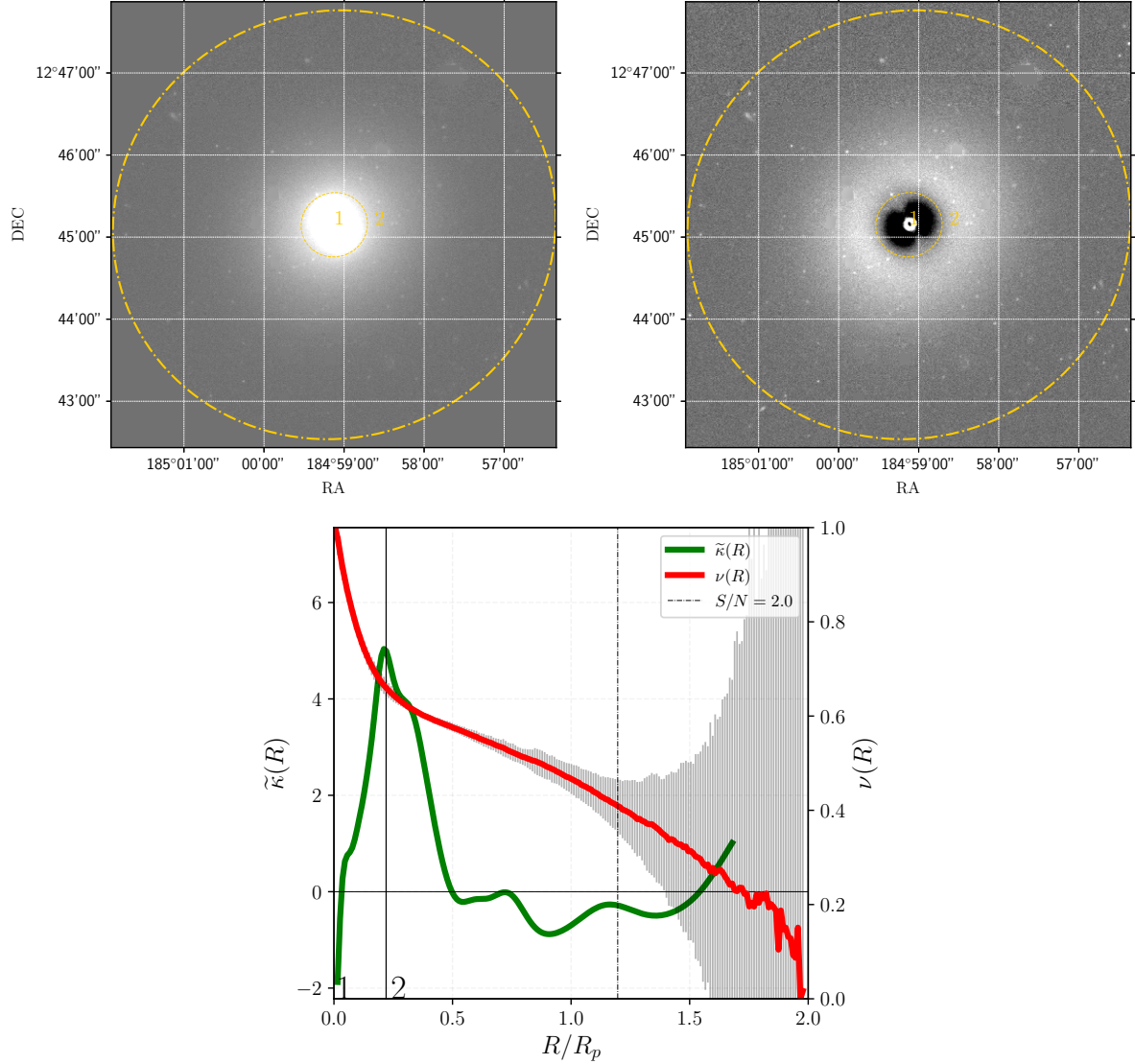
In region 3 (around $R/R_p \sim 0.8$) we see a broad and smooth valley of negative curvature, and subsequently being close to zero for $R/R_p > 1.0$ – this pattern appears because the disk is of type II (ERWIN; POHLEN; BECKMAN, 2008; MUÑOZ-MATEOS et al., 2013) which explains the broad valley. It is possible to discriminate a valley in $\tilde{\kappa}$ entailed by the disk of Type II morphology and one related to a ring or a bar. Valleys for bars and rings have high negative gradient in $\tilde{\kappa}$ and are thin in width (see additional examples in FIGURES 15, 16, 17, 18, 22, 23, 24 and 25).

NGC 2767

NGC 2767 is classified as an elliptical ([VAUCOULEURS et al., 1991](#)) and as an So ([NAIR; ABRAHAM, 2010](#)). However, the structure of this galaxy is not trivial to be resolved. [Yıldırım et al. \(2017\)](#) comment that the PA twist in the centre of the galaxy may imply the existence of a bar and a dust disk. Examining $\tilde{\alpha}$ in [FIGURE 18](#) shows the existence of two peaks and a narrow deep valley, revealing that the galaxy has at least three components (regions 1, 2 and 3). The bulged central part is demarcated by 1. The valley in 2 ($R/R_p \sim 0.4$), even not being negative (but ~ 0), is much smaller than the neighbouring peaks in terms of amplitude, therefore pointing to a bar component. The region 3 seems to be of a disk structure of type II, very similar to NGC 936 (note that after $R/R_p \sim 1.0$, the curvature almost vanishes). A final note is that, photometrically, the bulge of this galaxy is indicated to be pseudobulge due to the behaviour of $\tilde{\alpha}$ in the inner part of the profile – it takes some distance from the centre to increase significantly until the transition region at $R/R_p \sim 0.4$. Summarizing, in agreement with [Yıldırım et al. \(2017\)](#), the curvature entail that the galaxy may have a bulge+bar+disk structure. The residual image in the top right panel of [FIGURE 18](#) demonstrates these structures well within the delimited regions gathered from the curvature in bottom plot.

NGC 4267

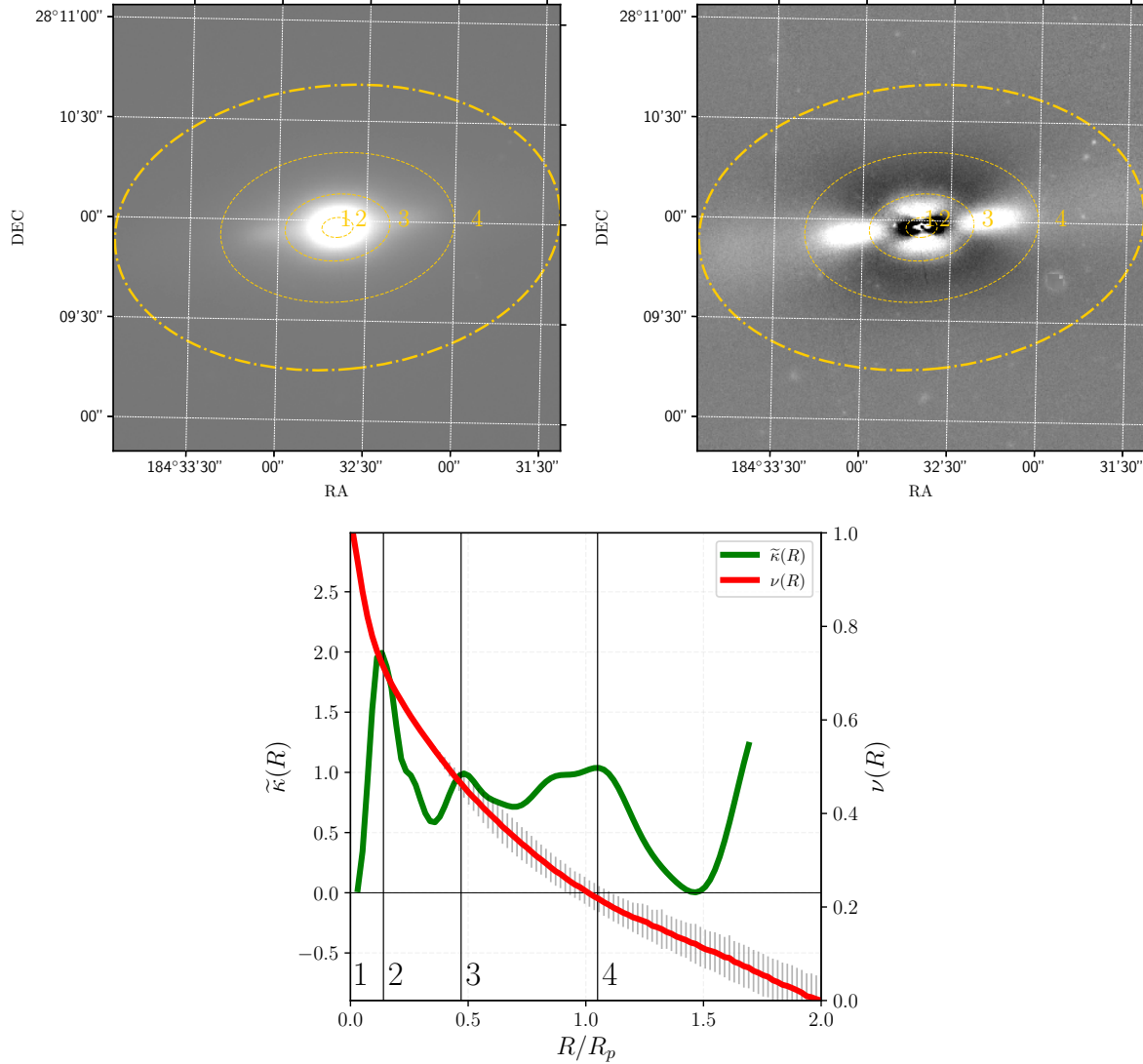
In earlier catalogues ([NILSON, 1973](#)) NGC 4267 was classified as So but the presence of a bar is also suggested ([SANDAGE; TAMMANN, 1981; WOZNIAK; PIERCE, 1991; JUNGWIERT; COMBES; AXON, 1997; Gadotti; de Souza, 2006; ERWIN; POHLEN; BECKMAN, 2008](#)) – SBo. The shape of $\tilde{\alpha}(R)$ is shown in [FIGURE 19](#). In comparison to NGC 2767, NGC 4267 exhibit an akin radial profile, however $\tilde{\alpha}$ is considerably different. Region 1 around $R/R_p \sim 0.3$ refers to the bulge while the disk takes part in the remaining of the profile in region 2 (lower $\tilde{\alpha}$ below zero). In respect to the bar, the curvature does not trace a sign of it because the pattern of a narrow valley is not exhibited. Also combining together the curvature and the residual image (middle panel of [FIGURE 19](#)), shows no evidence of a photometric bar component. In relation the bulge and the disk, the transition of both is highlighted by the peak in $\tilde{\alpha}$ at $R/R_p \sim 0.3$. The inner region shows an abrupt increasing of $\tilde{\alpha}$ from zero to the transition region with the disk, therefore this points that the bulge is a classical bulge. This is in agreement with [Fisher and Drory \(2010\)](#) (see their Table 2).

FIGURE 19 – The same as FIGURE 15, but for r -band of NGC 4267 from EFIGI.

NGC 4251

NGC 4251 is classified as So ([NILSON, 1973; SANDAGE; TAMMANN, 1981](#)) and SBo ([VAUCOULEURS et al., 1991](#)), but the confirmation of a bar component is not direct. [Wozniak and Pierce \(1991\)](#) performed a multicomponent analysis and reaffirmed its existence, having oval shape similar to the bulge. [Molaeinezhad et al. \(2017\)](#) indicates the presence of a bar based on the kinematics of the galaxy. [Fisher \(1997\)](#) noted that there is no bar in this system. The bar pattern for $\tilde{\kappa}$ does not appear in FIGURE 20, still we delimit the galaxy in regions. Region 1 and 2 (the part of the bulge) shows that the inner structure has a spheroidal shape. Analysing the residual image, great part of region 3 is supposed to be the bar, while 4 is the disk, since $\tilde{\kappa}$ decrease – do not account for $R/R_p > 1.5$, where $\tilde{\kappa}$ increases again, because of the filter. For this galaxy the limit $S/N \sim 2$ is externally to the cutted profile. Also, the

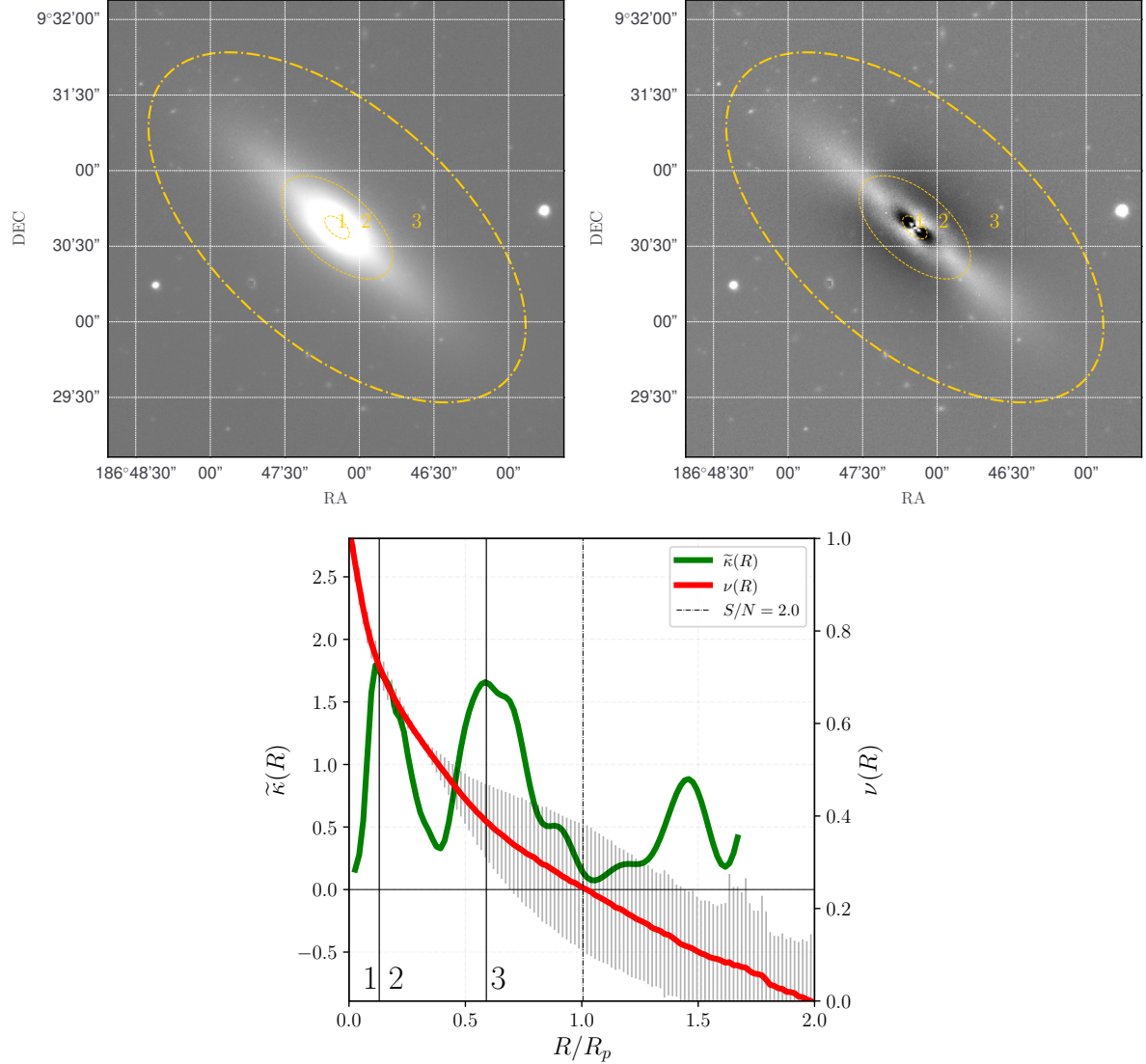
FIGURE 20 – The same as FIGURE 15, but for *i*-band of NGC4251 from SDSS.



pattern for bars found in other galaxies is not present in NGC4251.

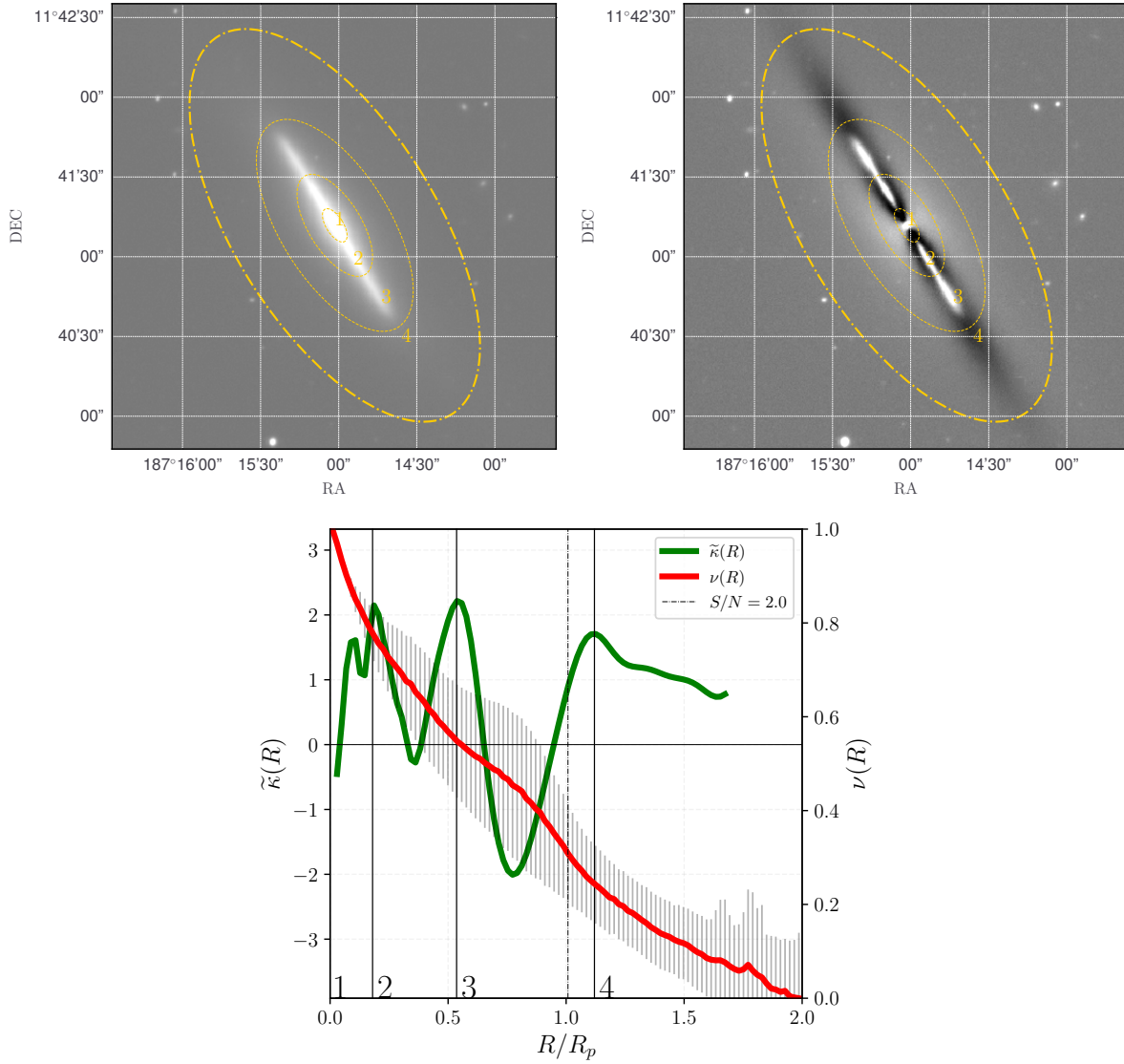
NGC 4417

NGC4417 is classified as SBo:edge-on ([VAUCOULEURS et al., 1991; HINZ; RIEKE; CALDWELL, 2003](#)) and also So:edge-on ([SANDAGE; TAMMANN, 1981; NILSON, 1973](#)). In the curvature plot of FIGURE 21, two peaks stand out in the first half of the R_p region: 1 and 2 seems to have a bulge morphology, while 3 is a disk. Analysing $\tilde{\kappa}$, it seems plausible that it distinguish two components inside $R/R_p \sim 1.0$, the first part identified by the first peak and the second by the second peak. Both components have small $\tilde{\kappa}$ (the values in the intermediary region are lower than the transitions). [Kormendy and Bender \(2012\)](#)

FIGURE 21 – The same as FIGURE 15, but for r band of NGC4417 from EFIGI.

argued that the inner part is an inner disk and 2 is the bulge⁶ with a boxy shape due to a faint bar. This seem reasonable to confirm here because the behaviour in $\tilde{\kappa}$ resembles a bar, as we are arguing here. However, in this case we could not differentiate the bulge from the bar. In the residual image it is clear that there are signs of two components, in 1 a more oval shape while in 2 a boxy one. A final comment is related to the peak in $\tilde{\kappa}$ close to $R/R_p \sim 1.5$. Due to the signal-to-noise limit and considering that this region is close to the edge of the galaxy, we do not treat it as a transition of components.

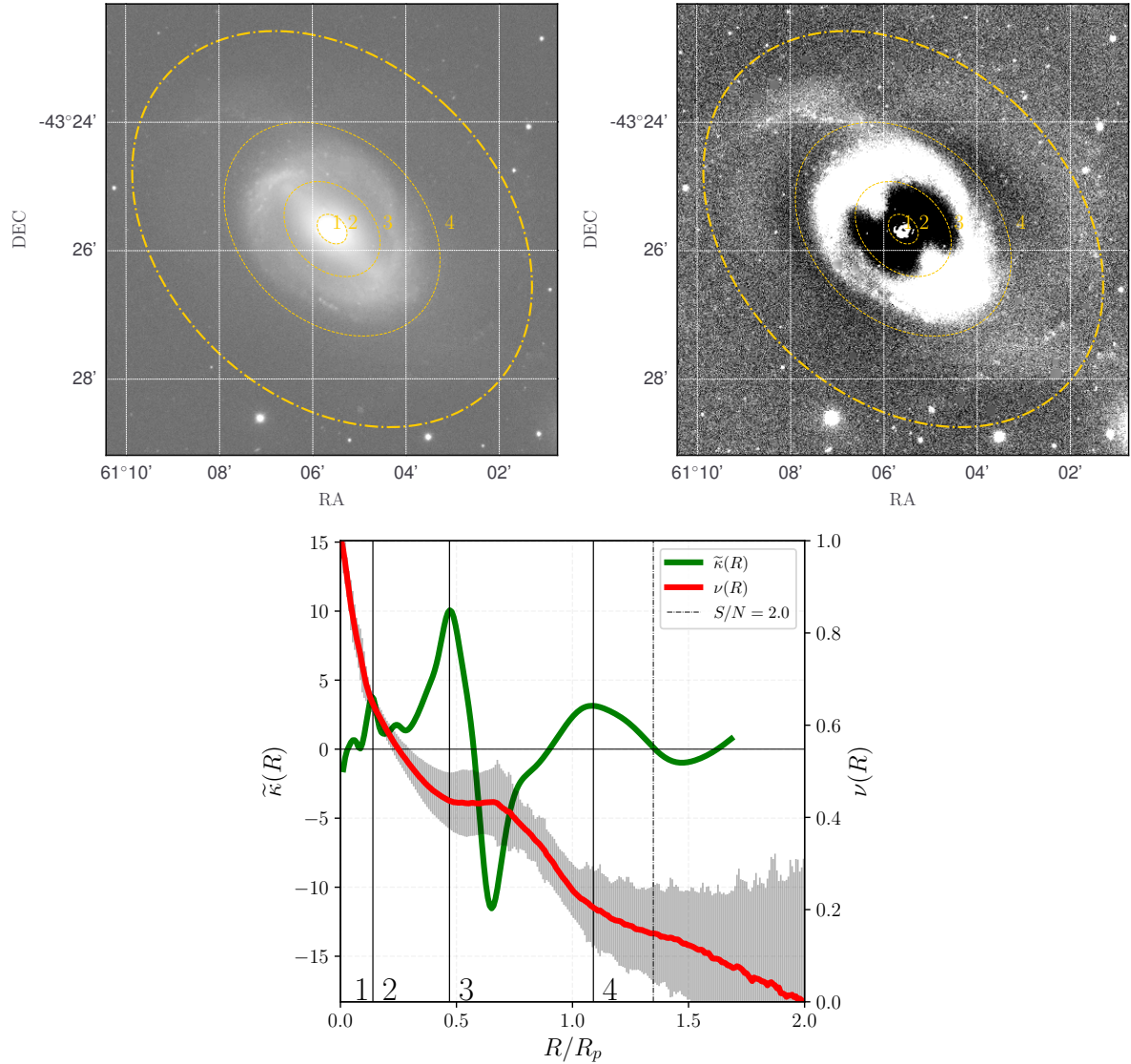
FIGURE 22 – The same as FIGURE 15, but for r band of NGC4452 from EFIGI.



NGC4452

NGC 4452 is an edge-on SBo(l) galaxy having a small pseudobulge ([KORMENDY; BENDER, 2012](#)). In the curvature plot of FIGURE 22 is seen a small component at the centre ($R/R_p \lesssim 0.15$). Since the first component has a small $\tilde{\kappa}$ and does not increase immediately, it is confirmed a pseudobulge component, however not being well pronounced due to the few data points. From that point to $R/R_p \sim 0.5$ the value of $\tilde{\kappa}$ reaches negative values and has the bar pattern, as exposed by [Kormendy and Bender \(2012\)](#). The bar extension goes to $R/R_p \sim 0.53$, marking the transition between the bar and the lens ([KORMENDY; BENDER, 2012](#)). The third smooth peak at $R/R_p \sim 1.1$ indicates the emergence of an outer disk with low positive value in curvature.

⁶ [Kormendy and Bender \(2012\)](#) found a prominent bulge ($B/T \sim 0.88$) to this galaxy.

FIGURE 23 – The same as FIGURE 15, but for r band of NGC 1512 from CTIO telescope.

5.2.2 Spirals

NGC1512

NGC 1512 is classified as a barred spiral galaxy SBa ([VAUCOULEURS et al., 1991](#)), however there are many references bringing up other components in its morphology: rings, pseudorings, nuclear ring and pseudobulge, see for example ([LAURIKAINEN et al., 2006; FISHER; DRORY, 2008](#)). According to [Compère, López-Corredoira and Garzón \(2014\)](#), who conducted a deep study on this galaxy, it has a bulge, a bar and a disk.

FIGURE 23 shows the results for $\tilde{\chi}$. The region inside $R/R_p < 0.5$ shows two components delimited by the local peak at $R/R_p \sim 0.15$, and both shows small $\tilde{\chi}$ compared with the overall curvature profile, therefore one must consider a pseudobulge component. From ([LAURIKAINEN et al., 2006](#); [COMPÈRE; LÓPEZ-CORREDOIRA; GARZÓN, 2014](#)), the innermost region (1) is a nuclear ring. Region 2 is dominated by the bulge. If fact, by the shape of $\tilde{\chi}$ it is a pseudobulge, which is in agreement with [Fisher, Drory and Fabricius \(2009\)](#), [Fisher and Drory \(2010\)](#).

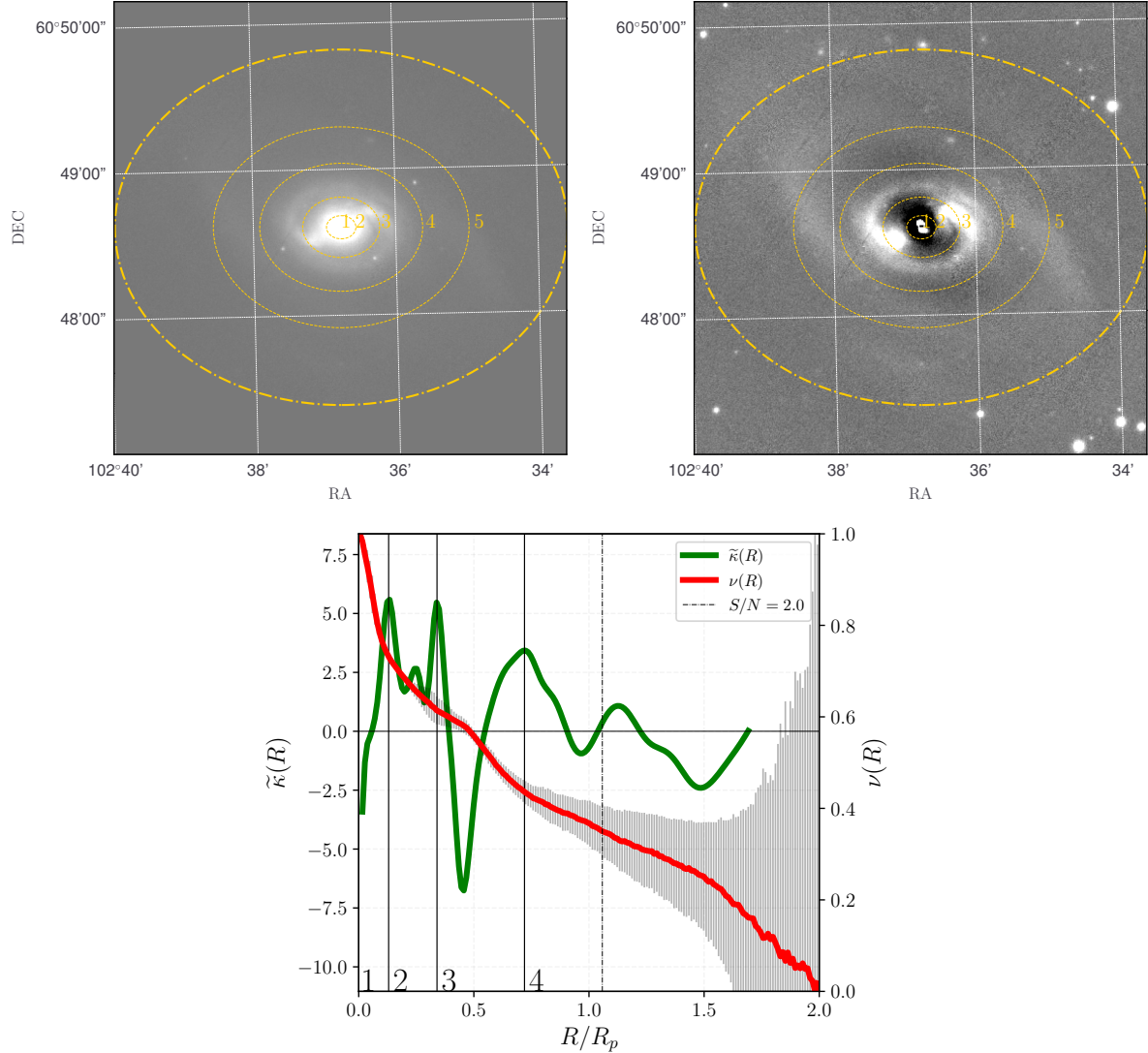
Regarding the bar, it seems that pseudobulge and bar coexist (the change in the position angle and ellipticity between the bulge and the bar is very smooth, see figure 4 of ([JUNGWIERT; COMBES; AXON, 1997](#))), with the bar connecting the pseudobulge and the outer ring – according to [Fisher and Drory \(2008\)](#), a pseudoring (region 3). This does not allow $\tilde{\chi}$ to distinguish the bar from the pseudobulge – in region 2 there is not a significant narrow valley to indicate it. [Fisher and Drory \(2008\)](#) also did not fit a bar component separately to NGC 1512 and considered only a Sérsic+Exp fit to it.

What is noticeably is the outer ring, the peak at $R/R_p \sim 0.5$ points to the transition between the pseudobulge+bar with this ring, which is dominant in region 3. The last smooth peak at $R/R_p \sim 1.1$ bound the dominance of the outer ring with a faint disk ($\tilde{\chi}$ approaches to zero).

NGC 2273

NGC 2273 is classified as SBa ([NILSON, 1973](#)) and SB(r)a ([VAUCOULEURS et al., 1991](#)). In FIGURE 24 the curvature indicates a small bulge contained inside $R/R_p \sim 0.1$ (region 1). Considering the valley in region 2, it retain a significant gradient in $\tilde{\chi}$ in comparison to the first and second peaks, this suggest a bar component. The next valley in region 3 is formed by two tightly wound spiral arms ([LAURIKAINEN; SALO, 2017](#)), which behaves like a ring. The fourth peak at $R/R_p \sim 0.5$ makes the transition of this ring with the outermost region of the galaxy.

[Cabrera-Lavers and Garzón \(2004\)](#) worked on in details considering the previous structures, adding a lens component and assuming that the outer region is a disk. Also, they argue that the bulge is prominent, nevertheless $\tilde{\chi}$ advises that the bulge is not too prominent. [Erwin and Sparke \(2003\)](#) says that this galaxy is four-ringed, two of them outer rings (outer region). The curvature give a picture of these rings in regions 4. The evidence that the bulge is not to prominent can be explained by the fact that the inner region can be formed by other components: [Moiseev, Valdés and Chavushyan \(2004\)](#) noted that the bar is of large scale; [Erwin and Sparke \(2003\)](#) and [Moiseev, Valdés and Chavushyan \(2004\)](#) also assert that the innermost region can be built by a nuclear spiral while [Mulchaey, Regan](#)

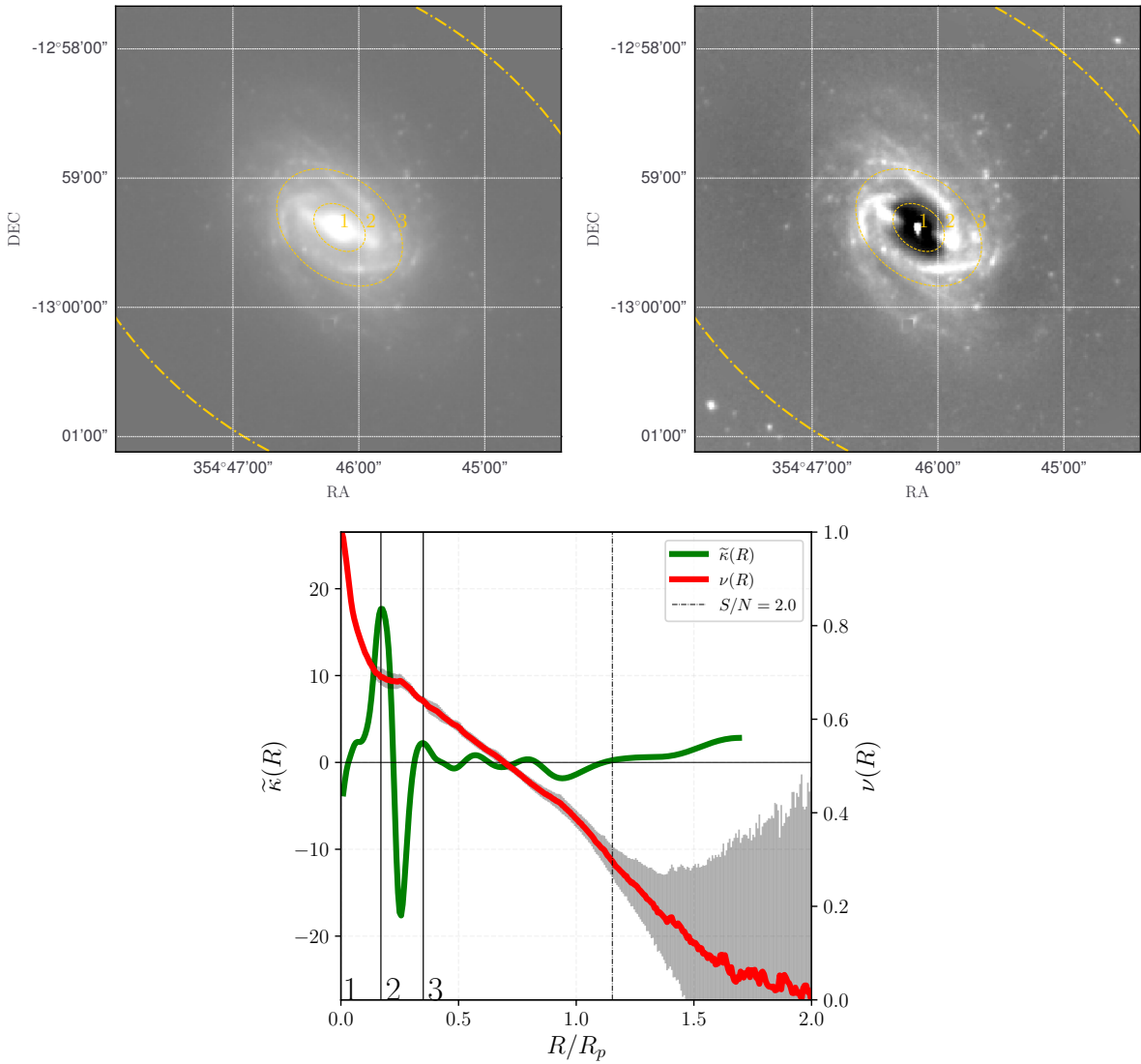
FIGURE 24 – The same as FIGURE 15, but for r band of NGC 2273 from Pan-STARRS survey.

and Kundu (1997) says that it is a secondary bar. Therefore, an acceptable constrain that $\tilde{\kappa}$ gives for NGC 2273 is a bulge+bar+ring/disk structure.

NGC 7723

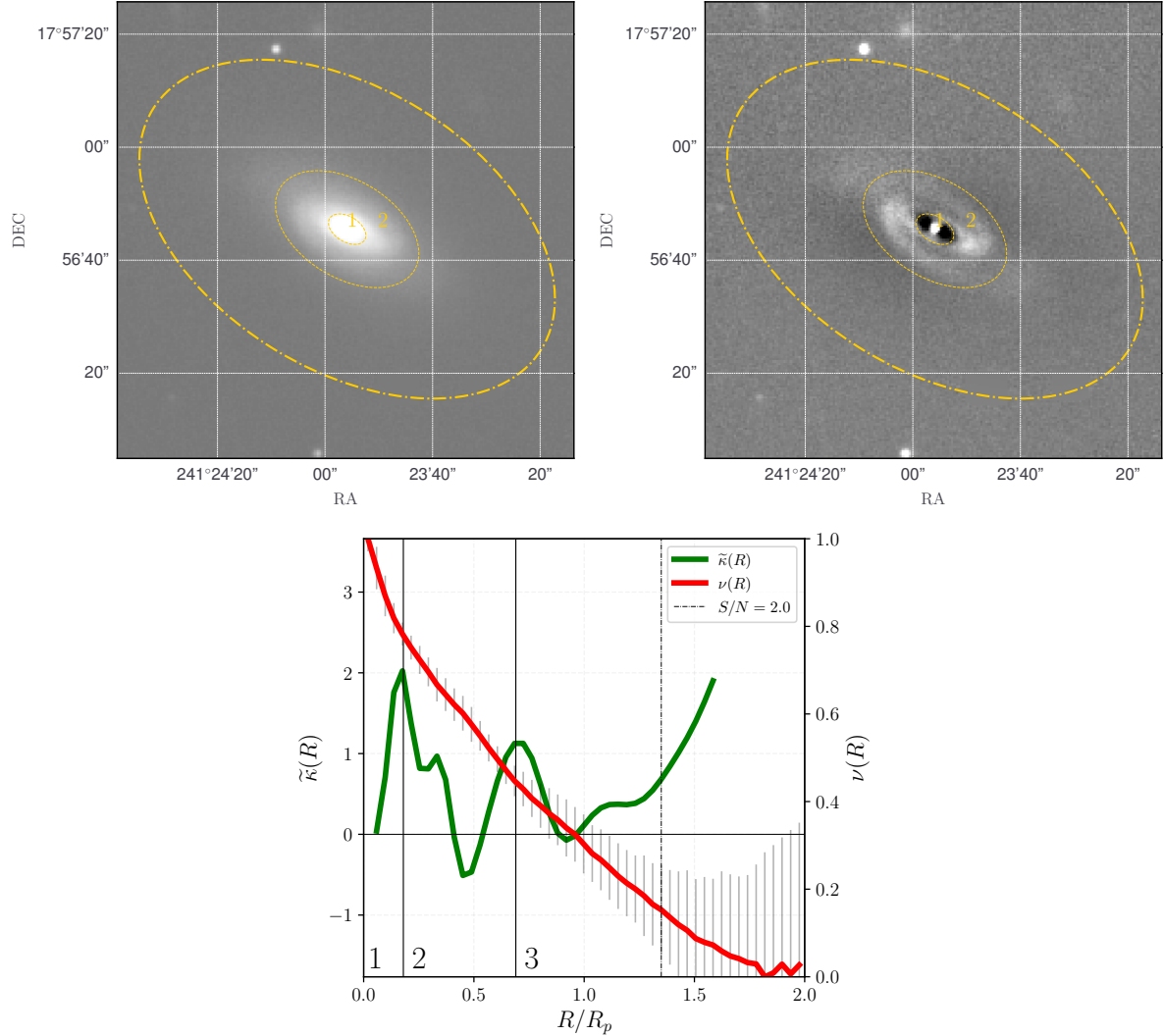
NGC 7723 is classified as SB(r)b/SB(rs) (VAUCOULEURS et al., 1991; COMERÓN, 2013). FIGURE 25 shows the result of the curvature for NGC 7723. The bulge is contained inside the region 1 delimited by $R/R_p \sim 0.1$. Eskridge et al. (2002) says that the central part of this galaxy is composed by a boxy bulge with a symmetric nucleus embedded in. As indicated by $\tilde{\kappa}$, it has a pseudobulge – note that $\tilde{\kappa}$ does not increase continuously and fast, it took up to $R/R_p \sim 0.2$ to grow abruptly until the transition region at the peak. This hint of a pseudobulge is in agreement with Prieto et al. (2001) (they found an

FIGURE 25 – The same as FIGURE 15, but for near infrared band ($3.6\mu\text{m}$) of NGC 7723 from Spitzer telescope.



unitary Sérsic index in r -band).

Analysing the valley in region 2 together with the residual image we see that it is related to a bar and a ring. However, the bar is much more prominent (PRIETO et al., 2001) than the later and it becomes non-trivial to demonstrate the existence of a ring. In fact, this component is considered to be a pseudoring formed by the way the spiral arms emerges from the bar (RÍO; CEPA, 1998; RÍO; CEPA, 1999; PRIETO et al., 2001; ESKRIDGE et al., 2002). In Aguerri et al. (2000) and Prieto et al. (2001) they mentioned the ring structure but in their structural decomposition they have not taken it into account. The spiral arms begin at $R/R_p \sim 0.35$ – observe the oscillations in $\tilde{\kappa}$. Río and Cepa (1998) made another commentary arguing that there is a disk outside the spiral arms, which is seen in $\tilde{\kappa}$ after $R/R_p \sim 1.0$ because $\tilde{\kappa} \sim 0$.

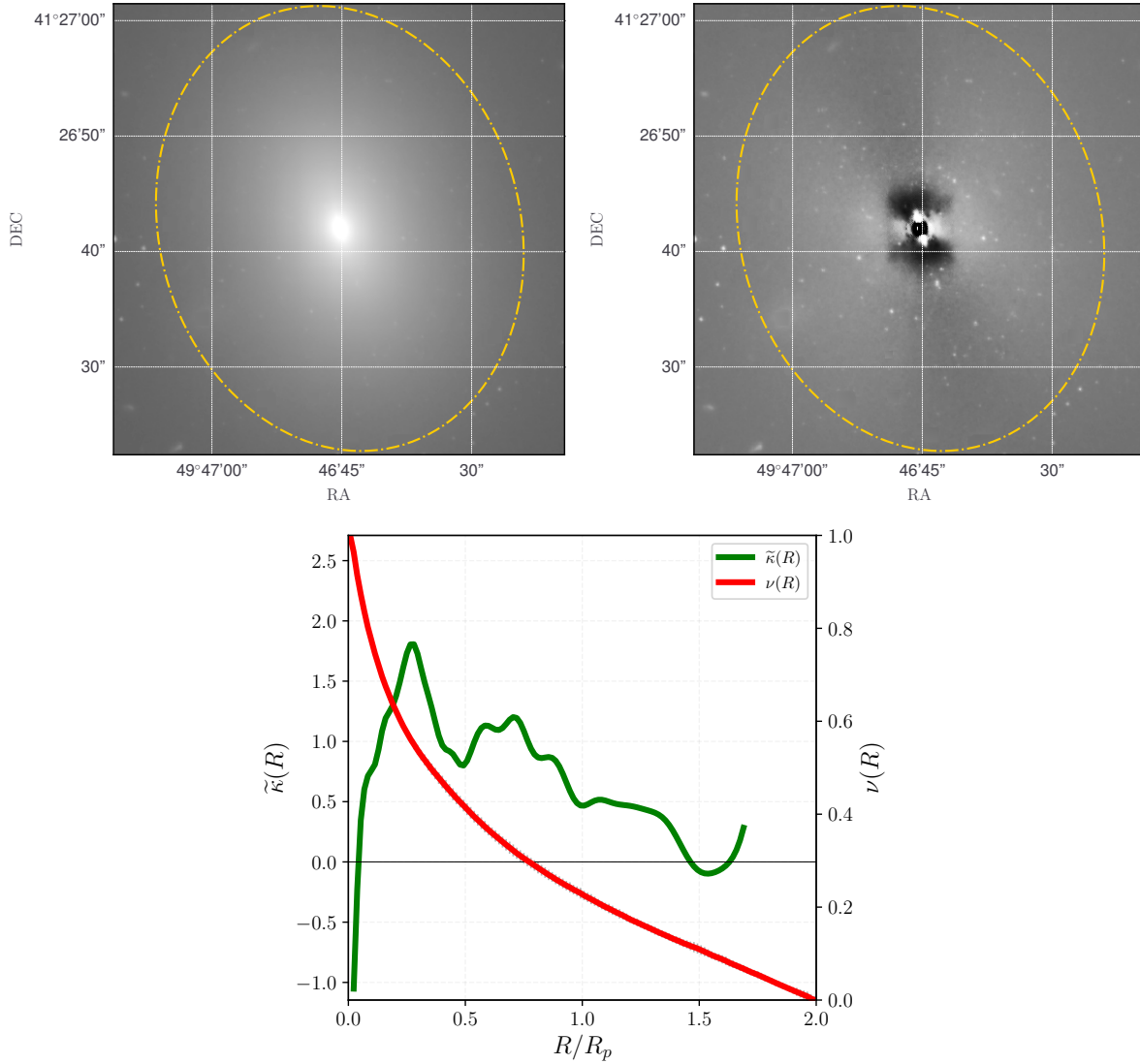
FIGURE 26 – The same as FIGURE 15, but for r band of NGC 6056.

NGC 6056

This galaxy is considered to be a barred spiral with an internal bulge (SB(s)o) ([VAUCOULEURS et al., 1991](#); [PRIETO et al., 2001](#)) and also non-barred (So/a) ([TARENGHI; GARILLI; MACCAGNI, 1994](#)). In $\tilde{\kappa}$ of FIGURE 26, the bulge is within $R/R_p \lesssim 0.18$ (first peak). The valley in 2 is the bar (the same behaviour in $\tilde{\kappa}$ as the other galaxies), and confirmed by ([PRIETO et al., 2001](#)). The transition of the bar with the outer disk (spiral) is the local peak at $R/R_p \sim 0.6$.

A pseudobulge component was pointed by [Prieto et al. \(2001\)](#) and they found a Sérsic fit of $n = 1.1$ in the r band. This is the only galaxy in our sample (but quite similar to NGC 4452) that the pseudobulge part does not show the same behaviour in $\tilde{\kappa}(R)$ as the other galaxies. We may attribute this to the low resolution of the galaxy image – note that there are few data points in the region pertaining to the bulge.

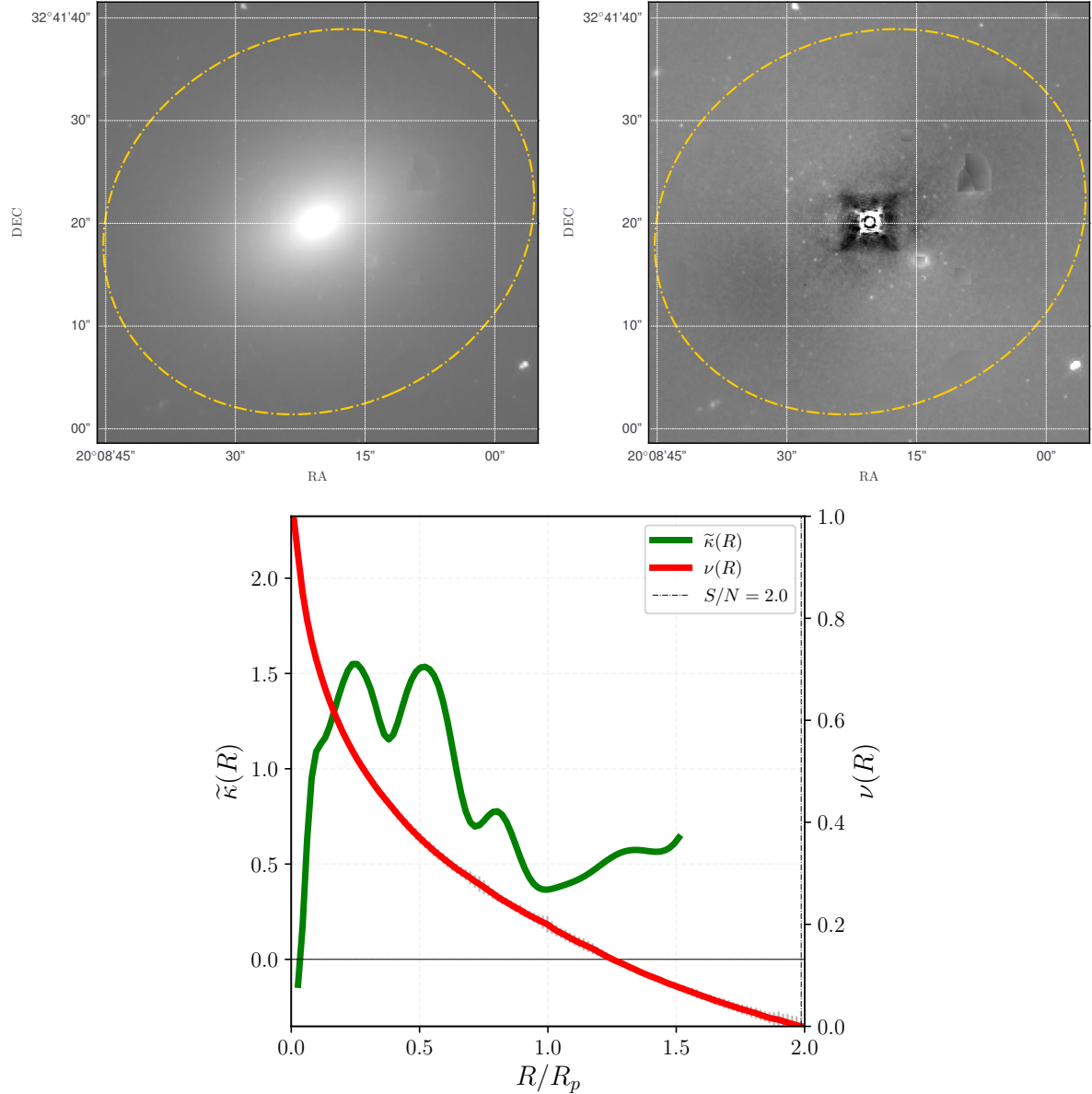
FIGURE 27 – The same as FIGURE 15, but for NGC 1270 from HST (f160w).



5.2.3 Spheroidal components

Unlike spiral and lenticular galaxies, whose components are structurally very diverse (bulge, bar, spiral arms and disk, for example), in the case of spheroidal galaxies (the various kind of ellipticals, bulges and some lenticular) the differences in the components are much more subtle. Consider, for instance, that many elliptical galaxies substructures cannot be seen in raw images, but rather, reveal themselves after image manipulation techniques, such as unsharp masking, brightness profile modelling and so on. In this way, we may regard that the effects that the different component of elliptical galaxies have on the curvature are more faint than for spiral galaxies.

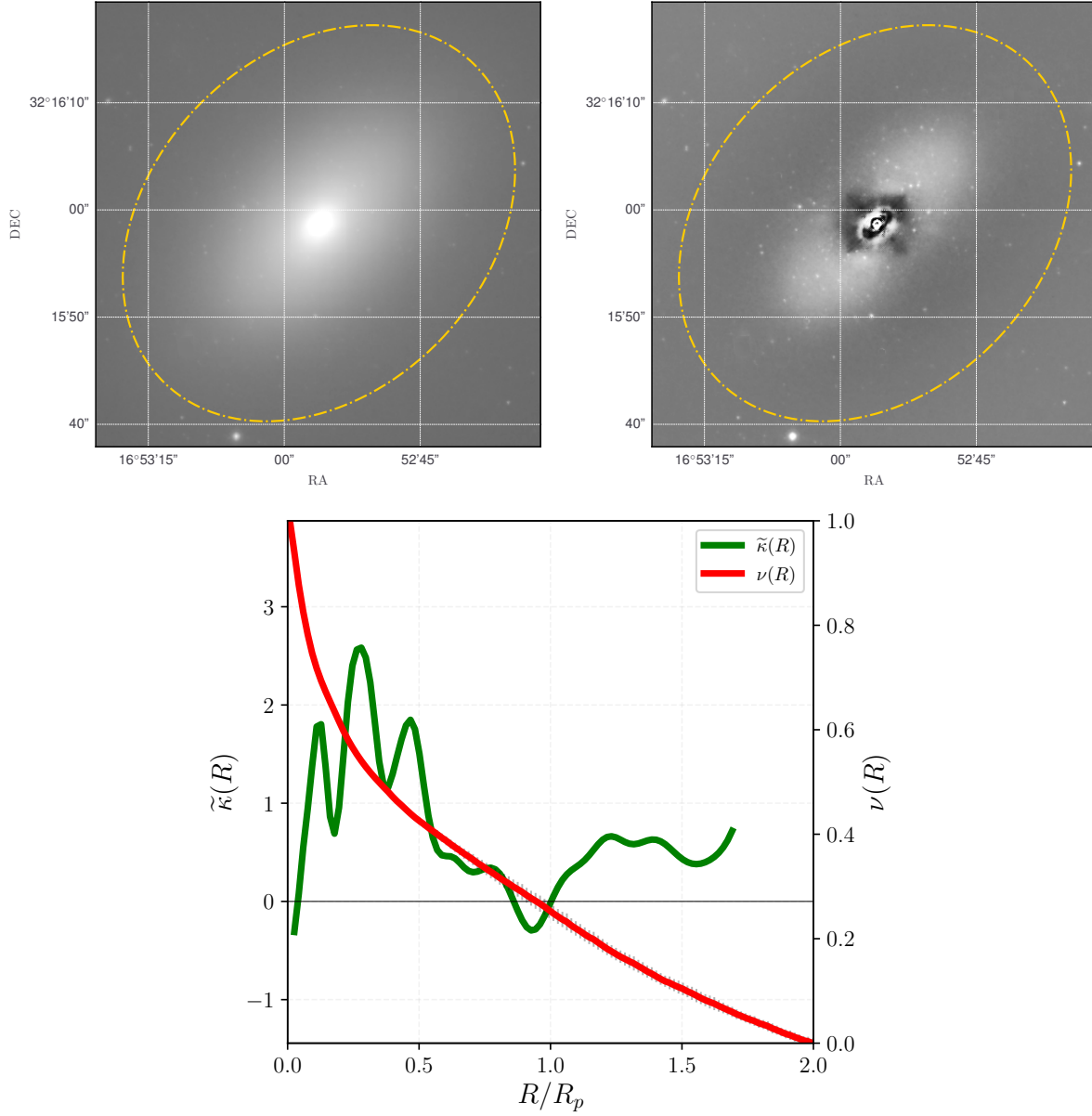
FIGURE 28 – The same as FIGURE 15, but for NGC 472 from HST (f160w).



NGC 1270

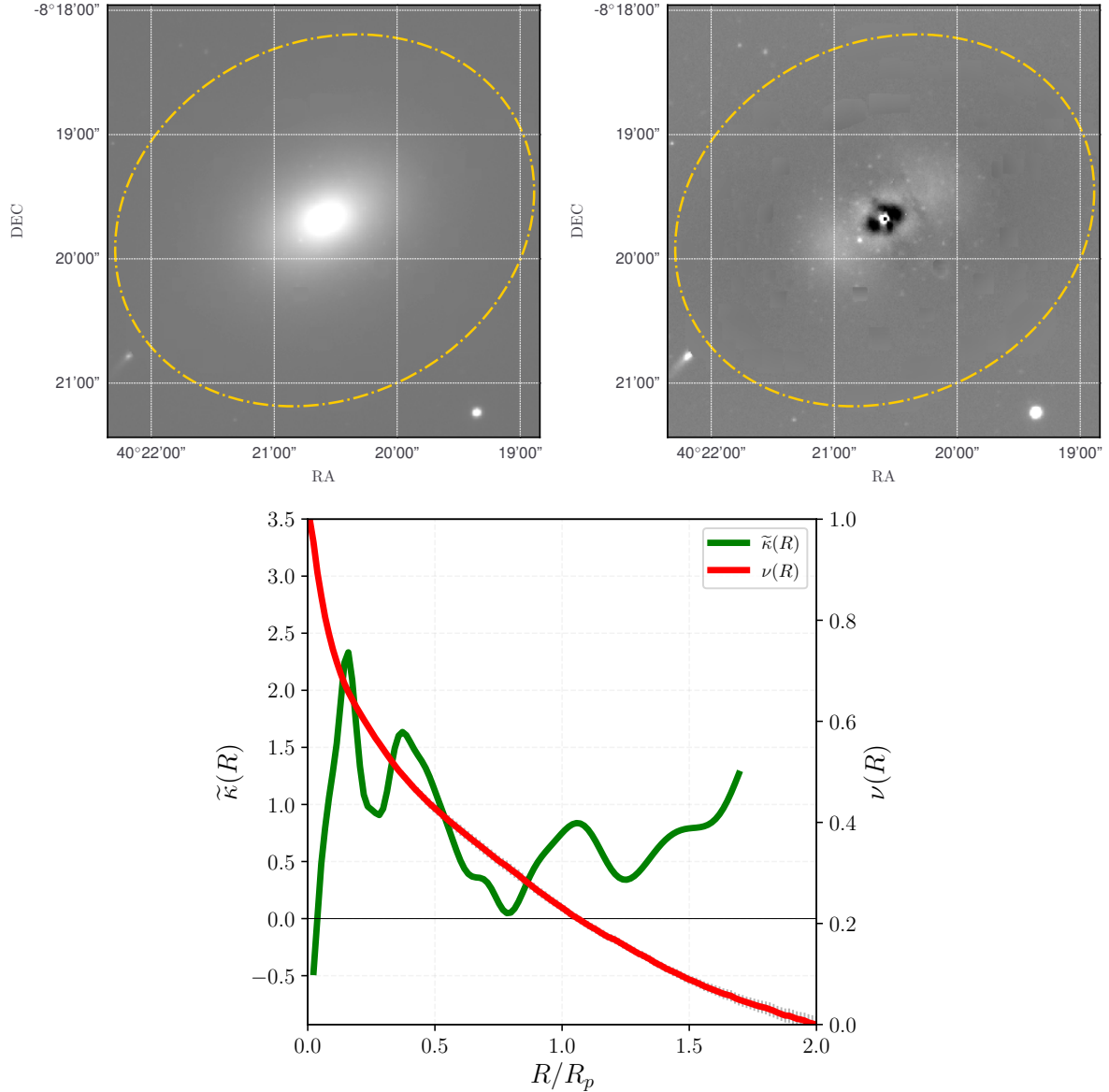
NGC 1270 is classified as an elliptical galaxy ([VAUCOULEURS et al., 1991](#)) and further as a compact elliptical galaxy ([YILDIRIM et al., 2017](#)). The curvature $\tilde{\kappa}(R)$ is displayed in FIGURE 27, its shape is not continuous (as expected) and having small oscillations of low scale. However, the curvature has a smooth overall shape, is high in inner regions (around $R/R_p \sim 0.2$) and drops to near zero at large radius. As can be seen in the residual image, the central region ($R/R_p \lesssim 0.25$) indicates an inner spheroidal component with different properties compared to the main body of the galaxy (missing light regarding the model for the main body). There is a sign of a small disk within $R/R_p \lesssim 0.1$ aligned with the apparent main axis of the galaxy.

FIGURE 29 – The same as FIGURE 15, but for NGC 384 from HST (f160w).



NGC 472

NGC 472 is a compact elliptical galaxy (YILDIRIM et al., 2017). Similar to NGC 1270, it does show some perturbations in the inner regions – the two local peaks are attributed to inhomogeneities – but the shape of $\tilde{\kappa}$ follows an overall shape resembling a pure component, which is smooth and increases in the inner region and decreases for the outermost part. A single Sérsic fit of $n = 5.8$ returned a robust representative model, since there is no residual structures in the outer regions.

FIGURE 30 – The same as FIGURE 15, but for r band of NGC 1052 from EFIGI.

NGC 384

NGC 384 is classified in literature as E ([VAUCOULEURS et al., 1991](#); [YILDIRIM et al., 2017](#)) but also So ([NILSON, 1973](#)). In comparison to NGC 472 and NGC 1270, $\tilde{\kappa}(R)$ is quite different (FIGURE 29) due to the emergence of the substantial oscillations in the region $R/R_p \lesssim 0.5$. These delineates some internal and small structure. In the residual image of FIGURE 29 it is readily seem such structure with a disk oval shape.

NGC 1052

NGC1052 is found as an elliptical galaxy in ([VAUCOULEURS et al., 1991](#)) and as E/So in ([SANDAGE; TAMMANN, 1981](#)). [Lauer et al. \(2007\)](#) indicates the presence of a core. In [FIGURE 30](#) the curvature suggests some possibly transition around $R/R_p \sim 0.15$, in which, therefore, might be between the core structure and the remaining structure of an elliptical. [Milone, Rickes and Pastoriza \(2007\)](#) (and references therein) conclude that NGC 1052 has a rotating disk. The curvature seems to indicate such kind of component because it has small values around $R/R_p \sim 0.75$, this is also seem in the residual image.

5.3 Identifying galaxy structures with curvature

We now bring together the behaviours of the curvature found in our data, exploring similarities between different galaxies. The curvature showed to be similar between components of the same morphology in different galaxies

Bars

Bars and rings show a depression pattern in $\tilde{\chi}$ where these components dominate. For NGC 936 and NGC 2767 ([FIGURE 17](#) and [FIGURE 18](#) respectively) the bars have a distinct valley between the two local peaks $1 \rightarrow 2$ and $2 \rightarrow 3$, respectively. These bars are represented by the narrows valleys in $\tilde{\chi}$ (note the difference between a narrow valley in $\tilde{\chi}$ related to a bar and a broad valley related to a disk type II in region 3 of NCG 936). For the faint bar of NGC 2273 ([FIGURE 24](#)), the curvature exhibit a deep but non non-negative valley in region 2 (between the two local peaks). We found that the depression in $\tilde{\chi}$ for bars is not always negative , but considerably lower than the local peaks. Galaxies NGC 1512 ([FIGURE 23](#)) and NGC 4251 ([FIGURE 20](#)) does not have a clear indication of a bar in (region 2 and 3, respectively). Despite this, considering that the bar exists in fact – according to the literature – for both galaxies, bulge and bar appear to show a subtle transition.

Rings

Galaxies NGC 1512 (FIGURE 23), NGC 2273 (FIGURE 24) and NGC 7723 (FIGURE 25) have rings. They exhibit a high and narrow negative gradient in region 3(first two) and region 2 (last one). These ring structures are also likely to be formed by the tight morphology of the spiral arms after the end of the bar. Between rings and bars, the rings showed more pronounced narrow valleys in $\tilde{\kappa}$.

Disks and spiral arms

The most notable galactic disk absent of spiral arms that shows values of $\tilde{\kappa}$ close to zero is that of NGC 4267 (FIGURE 19). For NGC 936 (FIGURE 17) the disk is of Type II, therefore it shows a valley in region 3, but the outer part approaches zero. A similar result is found for NGC 2767 (FIGURE 18). Another case is NGC 4417 (FIGURE 21) which in region 3 shows a decreasing $\tilde{\kappa}$ and reach small values, regarding that not all galaxy disks follows a $n = 1$ Sérsic law, therefore there are disk components that exhibit $\tilde{\kappa} > 0$ or $\tilde{\kappa} < 0$.

NGC 1357 (FIGURE 16), NGC 2273 (FIGURE 24), NGC 7723 (FIGURE 25) and NGC 6056 (FIGURE 26) have spiral arms. For NGC 7723 the spirals arm are well identified by $\tilde{\kappa}$ at the inner to middle part of region 3, due to the homogeneous oscillations. Galaxy NGC 1357 also shows two oscillations of this kind from the middle onwards part of region 3. For NGC 2273, the pattern in $\tilde{\kappa}$ is not well defined, but we still get an indication of a perturbed disk in region 4. The spiral galaxy in which the spiral structure does not appear clearly is NGC 6056.

Spheroidal

For our elliptical galaxies the curvature behaviour also revealed interesting results. For NGC 384 (FIGURE 29) $\tilde{\kappa}$ revealed an inner component due to the in the region $R/R_p < 0.5$, which is a inner dust disk. For NGC 472 (FIGURE 28), NGC 1052 (FIGURE 30) and NGC 1270 (FIGURE 27) $\tilde{\kappa}$ also indicates perturbations of $I(R)$. This behaviour indicates that these galaxies are not a complete homogeneous system but are formed by heterogeneous light distribution. This means that even in systems with subtle variations of the brightness profile, we can unveil the existence of perturbations in the galaxy's structure.

Pseudobulges

Another important result we found on this work is the behaviour of $\tilde{\kappa}$ for pseudobulges. Inner regions that shows small values of curvature compared to the values of posterior regions might infer pseudobulge components. In our sample the cases are NGC 1211 (FIGURE 15), NGC 936 (FIGURE 17), NGC 2767 (FIGURE 18), NGC 1512 (FIGURE 23), NGC 2273 (FIGURE 24) and NGC 7723 (FIGURE 25). For NGC 2273 this pattern is not too clear. For NGC 2767 there is no reference in literature indicating that the bulge is pseudo – here we point that it is.

In summary, in pseudobulges the curvatures displayed a distinct pattern. Since pseudobulges are more similar to disks, having nearly-exponential surface brightness profiles ([LAURIKAINEN; PELETIER; GADOTTI, 2016](#)), the curvature might in general shows a behaviour that resembles a disk, we mean this by having small values in inner regions and no abrupt variations (fast increasing) in some range of R .

Constraining scale length of galaxy components

We have seen in this work that $\tilde{\kappa}(R)$ is able to indicate the transition region of galactic components, in general by physical local peaks. The point of maximum of these peaks can be translated to the averaged radial width of each component, therefore we can constrain their scale lengths. This can be fundamental for automatized multicomponent analysis. Today, some number of fittings routines need beforehand information for initial guesses, which may come from visual inspection by an expert. However, covering a large space of initial values to these parameters imposes some limitations: restrict the analysis to a small data sample, some results leads to non-physical models, fitting routines may not converge, among others.

Hence, constraining the radial scale length of galaxy components can provide an initial parameter space that is physically motivated and can help in these routines. The curvature can be adapted and designed for that purpose if: i) we use it to infer how many components a galaxy does have; ii) what kind of morphology it has (because there is a clear distinction between (pseudo)bulges, disks and bars); and iii) the scale lengths. However, in order to keep the focus of this dissertation, this analysis is left for a future work (in preparation).

FIGURE 31 – Results of $\tilde{\kappa}(R)$ for sorted galaxies under C_1 (left) of TABLE 2. The three elliptical galaxies are PGC 29249, PGC 38740 and PGC 36678 while the others have a very different behaviour in $\tilde{\kappa}$, indicating that they are multicomponent.

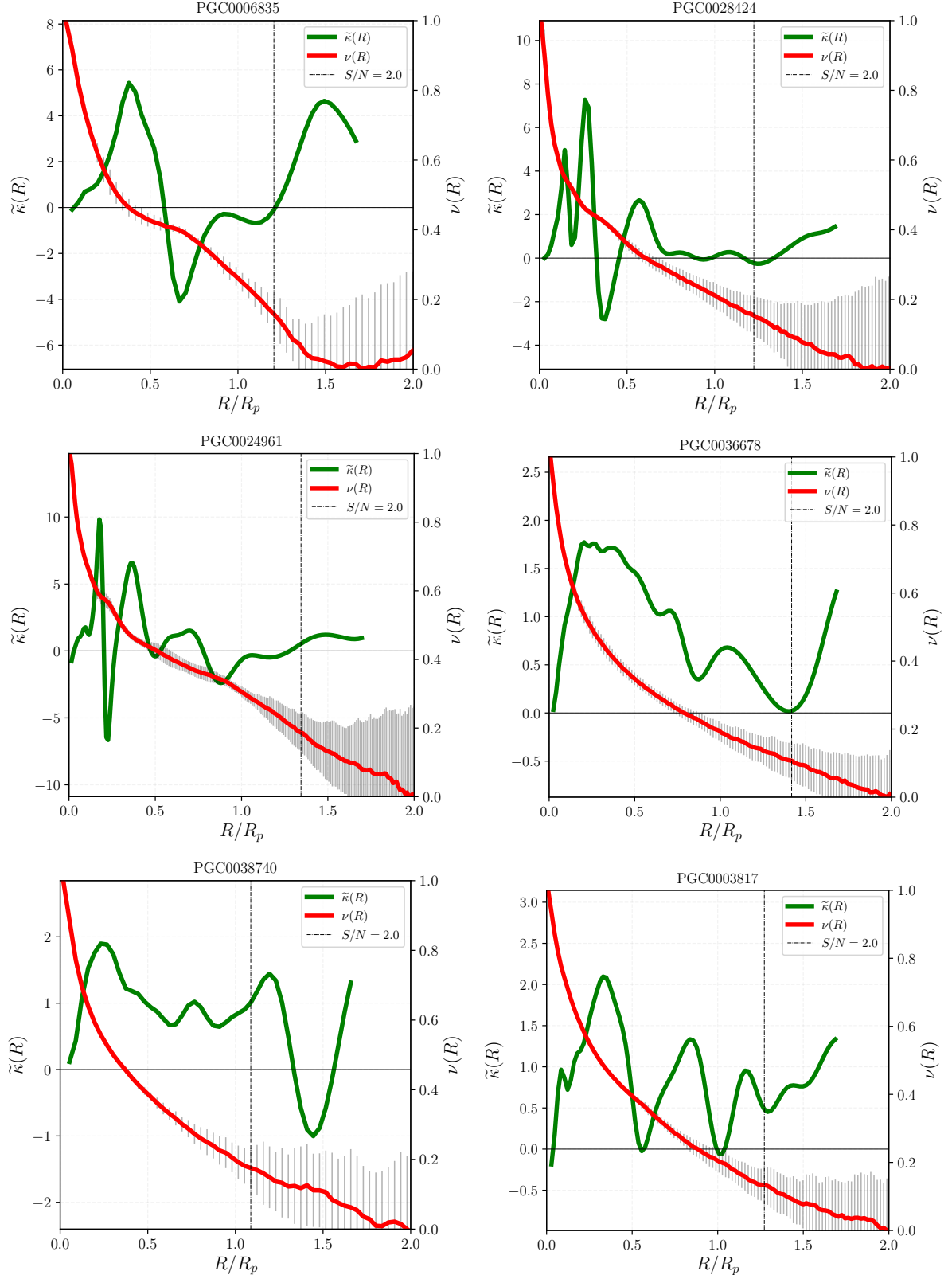
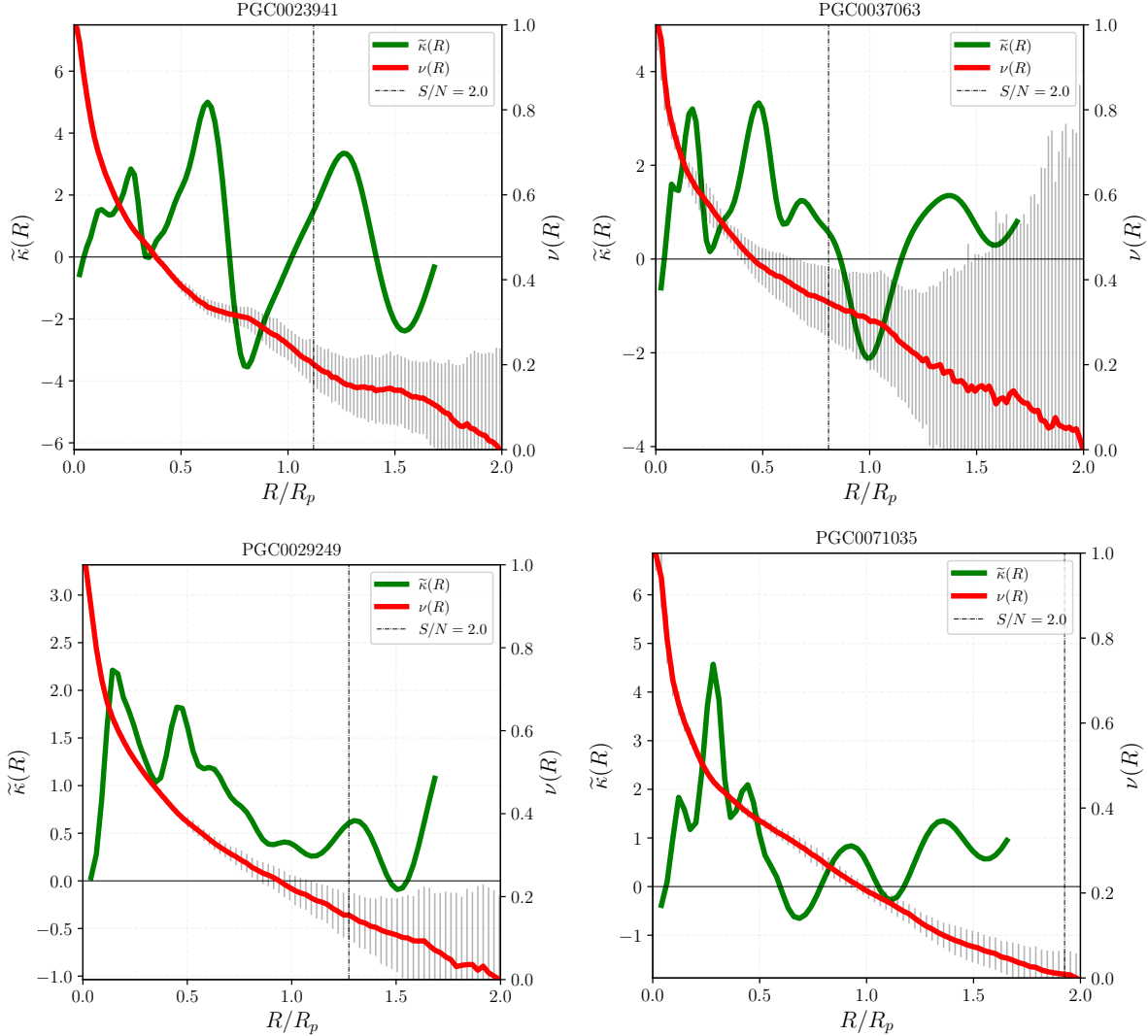


FIGURE 3I – continued.

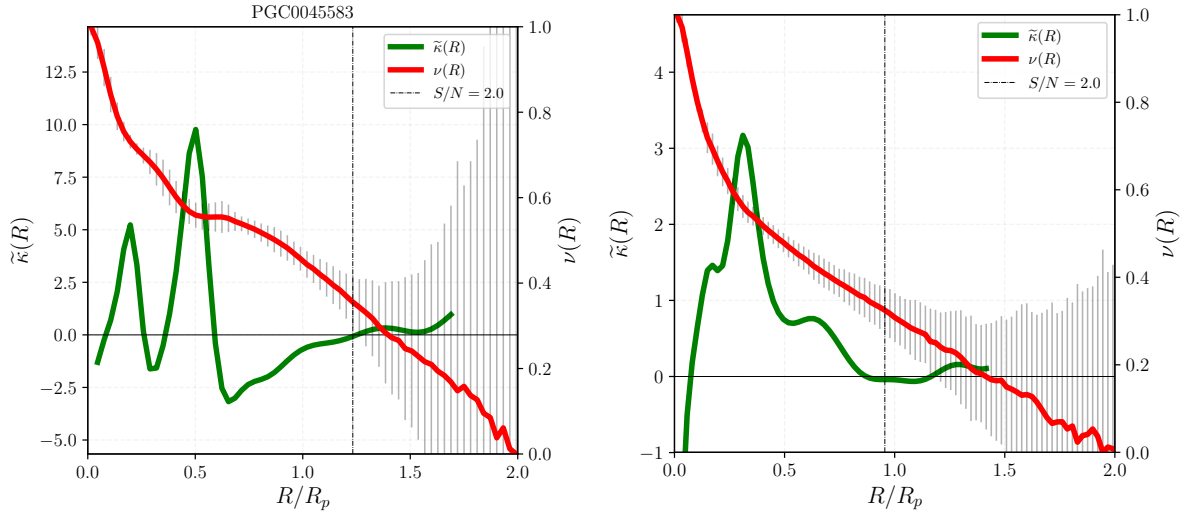


5.4 Misclassification of galaxies using C and n

In Section 3.1 we have discussed the issues of C and n that leads to misclassification of galaxies. In TABLE 2 we displayed some galaxies from the EFIGI sample that have high C , and most of them are not ellipticals, but spirals and $S\alpha$. Here we use $\tilde{\kappa}(R)$ to investigate its behaviour for these galaxies. The results are displayed in FIGURE 3I for the sorted galaxies under C_i . For the three elliptical galaxies, PGC 29249, PGC 38740 and PGC 36678 the curvature is in some sort similar between each other, but very different in relation of other galaxies in the table respective to C_i . The differences are exactly because they are multicomponents.

For PGC's 6835, 28424, 24961 and 37063 we see the ring/bar behaviour in $\tilde{\kappa}$; disks are also noted for the first three and for PGC 71035 (it is less notable for PGC 23941). For PGC 3817 (undetermined E

FIGURE 32 – Curvature calculated for the galaxies with high Sérsic indices of TABLE I.



or So) we see that $\tilde{\kappa}$ shows a perturbed structure in the galaxy, which is different of an elliptical and also different of a $n = 1$ disk in the outer part.

In relation to the high effective Sérsic indices presented in TABLE I, the results of $\tilde{\kappa}(R)$ are displayed in FIGURE 32. For PGC 45583 we see the pseudobulge + bar/ring behaviour in $\tilde{\kappa}$ and the outer disk; for PGC 59838 we see the classical bulge + disk behaviour in curvature.

In consequence of we demonstrated earlier, the concentration and the Sérsic parameter have particular cases that can mistakenly predict morphological types of galaxies. In the cases of a high C/n found, it is probably that the physical content of it is not plausible. One could wrongly say that a galaxy has a high C/n but it does not have at all, because it might have two or more components which were not taken into account. This acts to increase the value of C and n . However, since dealing with n is a non-linear procedure resulting sometimes in complications, and also since the data acquisition of such single fits from public data bases is poor or unavailable , we restrict ourselves to establish the final discussions under C . The fact is that, the increasing of values are more clearly pronounced in the concentration index, because its calculation is less complicated and more directly than n .

Our conclusions and as a consequence for what we discussed here are the following: galaxies might have high values of C in two situations:

1. there are the ones which are truly concentrated, for example UGC 5432, PGC 57139, NGC 3872, PGC 38740, NGC 426 and IC 708, which is an assumption of that ellipticals are high concentrated galaxies;
2. and the ones that are not spatially concentrated but multicomponent galaxies, the rest of galaxies

in TABLE 8.

This kind of physical configuration of components acts to increase the values of C and potentially misclassify spirals and disk galaxies into bulges and ellipticals.

At this stage we are confident that the effect mentioned until now is present in galaxies – to be confirmed in a more solid way with an extended analysis in a future work. Furthermore when a galaxy shows high C , a second study should be conducted to see if it is single or multicomponent. Additionally, when high values of a single Sérsic fits are found, we must doubt about it worrying if the value is a physical intrinsic property of the galaxy. These concepts already appeared in some works as we commented, but never were discussed before in a clear form. Here we have established one explanation of why bulge+disk can have higher values of C in comparison to a single component, such as a pure bulge or an elliptical.

So that our result do not get confused, we are not arguing that all multicomponent galaxies have increased C , higher than for elliptical, however for a considerable number of galaxies. Returning to the FIGURE 8 this becomes very clear, note that still there are spiral galaxies in a domain of small C

In summary, some notes are draw to pay attention:

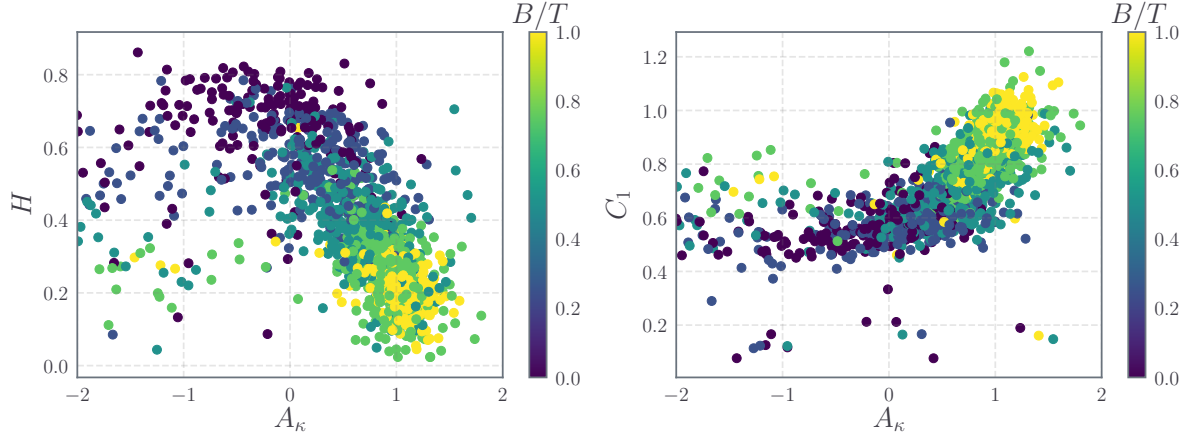
- C is most likely to be affected in more situations therefore we suggest that the calculation of C should to be accompanied by another structural analysis with the aim to break this degeneracy;
- when performing single Sérsic fits, it should be used carefully due to its sensibility to multicomponent galaxies. Therefore high values should be reviewed;
- when the measured properties leads to indication of these behaviours, the related galaxies should be studied with more detailed methodologies, to analyse the possibility if they are multicomponent.

5.5 Further Analysis

Area under curvature

To make our results more quantitatively we explore properties of the global shape of $\tilde{\chi}$ for many galaxies. The area under the curvature A_{χ} is supposed to be related to specific morphologies. A priori, high

FIGURE 33 – Diagnostic diagram for: **Left:** the information entropy H versus the integrated area under $\tilde{\kappa}$ for ~ 1600 galaxies of the EFIGI sample. **Right:** the concentration index C_I versus the integrated area under $\tilde{\kappa}$ for the same sample.



concentrated galaxies might show high values of A_{κ} because $I(R)$ is more steep than low concentrated. Hence, since in disk galaxies $\tilde{\kappa} \sim 0$ a priori we have $A_{\kappa} \sim 0$. Bulge+disk+barred galaxies can have the values of A_{κ} around zero, positive or negative, depending on the component that dominates.

We can define A_{κ} as the integral of $\tilde{\kappa}$ over the axis $\chi = R/2R_p$,

$$A_{\kappa} = \int_0^L \tilde{\kappa} d\chi. \quad (5.1)$$

in which in practice it is calculated with a discrete sum⁷. To understand the behaviour of A_{κ} , we compare its values with the concentration index C (CONSELICE, 2003; FERRARI; CARVALHO; TREVISAN, 2015) obtained for part of the EFIGI sample. We also compare it with the the information entropy H (FERRARI; CARVALHO; TREVISAN, 2015). We use the values of bulge-to-total ratio ξ_{BT} derived from the EFIGI catalogue by (BAILLARD et al., 2011).

FIGURE 33 displays the relation of A_{κ} with H (left) and A_{κ} with C (right) for a set of the EFIGI sample of galaxies. In the $A_{\kappa} - H$ diagram, low values of H ($\lesssim 0.25$) with positive A_{κ} ($\gtrsim 1$) represent elliptical and bulge dominated galaxies. On the opposite, small ($\lesssim 0.5$) or negative A_{κ} with high H ($\gtrsim 0.5$) are disk galaxies. In $A_{\kappa} - C$ diagram, high C_I ($\gtrsim 0.8$) and A_{κ} indicates ellipticals/bulge-dominated galaxies, while small C_I ($\lesssim 0.6$) and A_{κ} implies disk galaxies.

⁷ We use the `trapz` function from the Python Scipy library (<https://docs.scipy.org/doc/numpy/reference/generated/numpy.trapz.html>).

6

FINAL REMARKS

The avalanche of no future transcends into aimlessness

The foundation of whole mankind crumbles to a point of no return

Hesitation binders and takes it's toll, swaying and falling they lose control

Mindless zoo of fools.

Eloy - Point Of No Return

We summarise bellow our final remarks of the work. We have introduced the curvature of the brightness profile of galaxies as a tool to identify and study their different structural components, most notably bulges, bars, discs, rings and spiral arms. The underlying argument for such is that these components have distinct Sérsic index (or concentration) which directly impact the curvature. But, unlike standard multicomponent modelling of light profiles, the curvature is non parametric and does not depend on model parameters.

We measured the curvature profile for structural analysis to 16 galaxies (TABLE 3) comprising different morphologies. For these galaxies, we identified their structural components and inferred their domain regions in terms of the local peaks in $\tilde{\kappa}(R)$; Following the peaks in the measured curvature profile we spotted the matching regions in the image and residual maps where the different components can be identified and related to the curvature behaviour. Thus regarding the curvature curve (in terms of logarithm normalized scale of intensity):

1. Disks have a broad profile in the curvature with near zero (Type I) or negative (Type II) values.
2. Bars and rings have narrow negative valleys in $\tilde{\kappa}$ (more pronounced for rings);
3. pseudobulges have small values (compared to the highest absolute values) or near zero curvature in their regions;

4. the curvature in elliptical galaxies shows that they are not completely homogeneous system;

We also have extended the calculation of $\tilde{\chi}$ for galaxies of TABLE 2 which have high values of C . The results in FIGURE 3I shows that $\tilde{\chi}$ is able to unveil the cases that galaxies are multicomponent. Our critical review is that the concentration index and the effective Sérsic parameter should be carefully used in the analysis of galaxies, since they are affected by multicomponent galaxies. The study of the data with a second methodology – such as $\tilde{\chi}$ – can avoid the misclassifications. In respect to the analysis of high effective Sérsic parameters, an extended exploration was not possible since we found difficulties getting the data from other works.

Work in progress

Our next steps in the current work, with the main purpose of multicomponent analysis, is divided into basic three studies: **i)** Improve the calculation of $\tilde{\chi}$, including in the filter the explicit dependence of the signal-to-noise along radius, and obtain each structural component automatically, therefore the procedure can be implemented in analysis of large data sets. Also, tests the limits of curvature in terms of resolution, applied to Jellyfish galaxies – a collaborated work already established. **ii)** continue explore the effects of high concentration and effective Sérsic parameters; and use the curvature to break the misclassifications that were made, also we aim to use the curvature in fitting routines to suggest each morphological component that will be fitted in, as a constrain for the Sérsic parameters. A collaboration has already been established for the analysis of the images from the Hubble Space Telescope; **iii)** extend the study of the information entropy H in morphometry to the general non-extensive case, where the information theory is generalized by the Tsallis generalization of statistical mechanics ([TSALLIS, 1988](#); [TSALLIS, 2009](#)), see also ([RODRIGUES; GIRALDI, 2009](#); [LIN; OU, 2012](#); [RAMÍREZ-REYES et al., 2016](#)). A work already have been started, showing original results which will be published soon.

References

- ABAZAJIAN, K. et al. The first data release of the sloan digital sky survey. *The Astronomical Journal*, IOP Publishing, v. 126, n. 4, p. 2081–2086, 2003. Available from Internet: <<https://doi.org/10.1086%2F378165>>.
- ABRAHAM, R. G.; BERGH, S. van den; NAIR, P. A new approach to galaxy morphology. i. analysis of the sloan digital sky survey early data release. *The Astrophysical Journal*, IOP Publishing, v. 588, n. 1, p. 218–229, 2003. Available from Internet: <<https://doi.org/10.1086%2F373919>>.
- ABRAHAM, R. G. et al. The morphologies of distant galaxies. i: an automated classification system. *The Astrophysical Journal*, Hampton, E.U.A., v. 432, p. 75–90, 1994.
- AGUERRI, J. A. L. et al. Optical surface photometry of a sample of disk galaxies. i. observations and data reduction. *The Astronomical Journal*, IOP Publishing, v. 119, n. 4, p. 1638–1644, 2000. Available from Internet: <<https://doi.org/10.1086%2F301281>>.
- ALAM, S. et al. The eleventh and twelfth data releases of the sloan digital sky survey: Final data from sdss-iii. *The Astrophysical Journal Supplement Series*, IOP Publishing, v. 219, n. 1, p. 12, 2015. Available from Internet: <<https://doi.org/10.1088%2F0067-0049%2F219%2F1%2F12>>.
- ANDRAE, R.; JAHNKE, K.; MELCHIOR, P. Parametrizing arbitrary galaxy morphologies: potentials and pitfalls. *Monthly Notices of the Royal Astronomical Society*, v. 411, n. 1, p. 385–401, 2011. ISSN 0035-8711. Available from Internet: <<https://doi.org/10.1093/mnras/stt160.x>>.
- ARGYLE, J. J. et al. Bayesian bulge-disc decomposition of galaxy images. *ArXiv e-prints*, 2018.
- ASCASIBAR, Y.; GOTTLÖBER, S. The dynamical structure of dark matter haloes. *Monthly Notices of the Royal Astronomical Society*, v. 386, n. 4, p. 2022–2030, 2008. ISSN 0035-8711. Available from Internet: <<https://doi.org/10.1093/mnras/stn160.x>>.
- ATHANASSOULA, E. On the nature of bulges in general and of box/peanut bulges in particular: input from N-body simulations. *Monthly Notices of the Royal Astronomical Society*, v. 358, n. 4, p. 1477–1488, 2005. ISSN 0035-8711. Available from Internet: <<https://doi.org/10.1093/mnras/stn160.x>>.
- BAGGETT, W. E.; BAGGETT, S. M.; ANDERSON, K. S. J. Bulge-Disk Decomposition of 659 Spiral and Lenticular Galaxy Brightness Profiles. *The Astronomical Journal*, v. 116, p. 1626–1642, 1998.
- BAILLARD, A. et al. The efigi catalogue of 4458 nearby galaxies with detailed morphology. *Astronomy & Astrophysics*, v. 532, p. A74, 2011. Available from Internet: <<https://doi.org/10.1051/0004-6361/201016423>>.

BERGH, S. van den. A Preliminary Luminosity Classification for Galaxies of Type Sb. *Astrophysical Journal*, E.U.A., v. 131, p. 558, 1960. Available from Internet: <<http://adsabs.harvard.edu/abs/1960ApJ...131..558V>>.

BERGH, S. van den. A Preliminary Luminosity Classification of Late-Type Galaxies. *Astrophysical Journal*, E.U.A., v. 131, p. 215, 1960. Available from Internet: <<http://adsabs.harvard.edu/abs/1960ApJ...131..215V>>.

BERGH, S. van den. A new classification system for galaxies. *Astrophysical Journal*, Hampton, E.U.A., v. 206, p. 883–887, 1976. Available from Internet: <<http://adsabs.harvard.edu/abs/1976ApJ...206..883V>>.

BERSHADY, M. A.; JANGREN, A.; CONSELICE, C. J. Structural and Photometric Classification of Galaxies. I. Calibration Based on a Nearby Galaxy Sample. *The Astronomical Journal*, The University of Chicago Press, Chigaco, E.U.A., v. 119, p. 2645–2663, 2000. Available from Internet: <http://adsabs.harvard.edu/cgi-bin/bib_query?arXiv:astro-ph/0002262>.

BLANTON, M. R. et al. The luminosity function of galaxies in SDSS commissioning data. *The Astronomical Journal*, IOP Publishing, v. 121, n. 5, p. 2358–2380, 2001. Available from Internet: <<https://doi.org/10.1086%2F320405>>.

BRUCE, V. A. et al. The bulge–disc decomposed evolution of massive galaxies at $1 < z < 3$ in CANDELS. *Monthly Notices of the Royal Astronomical Society*, v. 444, n. 2, p. 1001–1033, 2014. ISSN 0035-8711. Available from Internet: <<https://doi.org/10.1093/mnras/stu1478>>.

BRUCE, V. A. et al. The decomposed bulge and disc size-mass relations of massive galaxies at $1 < z < 3$ in CANDELS. *Monthly Notices of the Royal Astronomical Society*, v. 444, p. 1660–1673, 2014.

BURKERT, A.; NAAB, T. Major mergers and the origin of elliptical galaxies. In: _____. *Galaxies and Chaos*. Berlin, Heidelberg: Springer Berlin Heidelberg, 2003. p. 327–339. ISBN 978-3-540-45040-5. Available from Internet: <https://doi.org/10.1007/978-3-540-45040-5_27>.

BUTA, R.; COMBES, F. Galactic Rings. *Fundamentals of Cosmic Physics*, v. 17, p. 95–281, 1996.

BUTA, R. J. Galaxy morphology. In: _____. *Secular Evolution of Galaxies*. Cambridge University Press, 2013. (Canary Islands Winter School of Astrophysics), p. 155–258. ISBN 9781139547420. Available from Internet: <<https://doi.org/10.1017/CBO9781139547420>>.

CABRERA-LAVERS, A.; GARZÓN, F. An optical study of a sample of spiral galaxies. *The Astronomical Journal*, v. 127, n. 3, p. 1386, 2004. Available from Internet: <<http://stacks.iop.org/1538-3881/127/i=3/a=1386>>.

CAON, N.; CAPACCIOLI, M.; D’ONOFRIO, M. On the Shape of the Light Profiles of Early Type Galaxies. *Monthly Notices of the Royal Astronomical Society*, v. 265, p. 1013, 1993.

CAROLLO, C. M. The Centers of Early- to Intermediate-Type Spiral Galaxies: A Structural Analysis. *The Astrophysical Journal*, v. 523, p. 566–574, 1999.

CASEY, J. *Exploring Curvature*. [S.l.]: Springer, 1996. ISBN 978-3-528-06475-4.

CHAMBERS, K. C. et al. The Pan-STARRS1 Surveys. *arXiv e-prints*, p. arXiv:1612.05560, 2016.

CHENG, J. Y. et al. Automated morphological classification of Sloan Digital Sky Survey red sequence galaxies. *Monthly Notices of the Royal Astronomical Society*, v. 412, p. 727–747, 2011.

CIOTTI, L.; BERTIN, G. Analytical properties of the $R^{1/m}$ law. *Astronomy and Astrophysics*, v. 352, p. 447–451, 1999.

COLE, S. et al. A recipe for galaxy formation. *Monthly Notices of the Royal Astronomical Society*, v. 271, n. 4, p. 781–806, 1994. ISSN 0035-8711. Available from Internet: <<https://doi.org/10.1093/mnras/271.4.781>>.

COLE, S. et al. Hierarchical galaxy formation. *Monthly Notices of the Royal Astronomical Society*, v. 319, n. 1, p. 168–204, 2000. Available from Internet: <<http://dx.doi.org/10.1046/j.1365-8711.2000.03879.x>>.

COMERÓN, S. Inner rings in disc galaxies: dead or alive. *Astronomy & Astrophysics*, v. 555, p. L4, 2013. Available from Internet: <<https://doi.org/10.1051/0004-6361/201321983>>.

COMPÈRE, P.; LÓPEZ-CORREDOIRA, M.; GARZÓN, F. Three-dimensional decomposition of galaxies with bulge and long bar. *Astronomy & Astrophysics*, v. 571, p. A98, 2014.

CONSELICE, C. J. The Relationship between Stellar Light Distributions of Galaxies and Their Formation Histories. *The Astrophysical Journal Supplement Series*, v. 147, p. 1–28, 2003.

CONSELICE, C. J. The Evolution of Galaxy Structure over Cosmic Time. *Ann. Rev. Astron. Astrophys.*, v. 52, p. 291–337, 2014.

CONSELICE, C. J.; BERSHADY, M. A.; JANGREN, A. The Asymmetry of Galaxies: Physical Morphology for Nearby and High-Redshift Galaxies. *The Astrophysical Journal*, v. 529, p. 886–910, 2000.

CRANE, K. et al. Digital geometry processing with discrete exterior calculus. In: *ACM SIGGRAPH 2013 Courses*. New York, NY, USA: ACM, 2013. (SIGGRAPH '13), p. 7:1–7:126. ISBN 978-1-4503-2339-0. Available from Internet: <<http://doi.acm.org/10.1145/2504435.2504442>>.

DALE, D. A. et al. The spitzer local volume legacy: Survey description and infrared photometry. *The Astrophysical Journal*, IOP Publishing, v. 703, n. 1, p. 517–556, 2009. Available from Internet: <<https://doi.org/10.1088%2F0004-637X%2F703%2F1%2F517>>.

de Vaucouleurs, G. Recherches sur les Nebuleuses Extragalactiques. *Annales d'Astrophysique*, v. II, p. 247, 1948.

DESTREZ, R. et al. Automatic registration of 3d dental mesh based on photographs of patient's mouth. *Computer Methods in Biomechanics and Biomedical Engineering: Imaging & Visualization*, Taylor & Francis, v. 0, n. 0, p. 1–12, 2018. Available from Internet: <<https://doi.org/10.1080/21681163.2018.1519849>>.

DIEMAND, J.; KUHLEN, M.; MADAU, P. Formation and evolution of galaxy dark matter halos and their substructure. *The Astrophysical Journal*, IOP Publishing, v. 667, n. 2, p. 859–877, 2007. Available from Internet: <<https://doi.org/10.1086%2F520573>>.

DIMAURO, P. et al. A catalog of polychromatic bulge-disc decompositions of ~ 17.600 galaxies in CANDELS. *Monthly Notices of the Royal Astronomical Society*, v. 478, p. 5410–5426, 2018.

DUBOIS, Y. et al. Dancing in the dark: galactic properties trace spin swings along the cosmic web. *Monthly Notices of the Royal Astronomical Society*, v. 444, n. 2, p. 1453–1468, 2014. ISSN 0035-8711. Available from Internet: <<https://doi.org/10.1093/mnras/stu1227>>.

ELMEGREEN, D. M.; ELMEGREEN, B. G. Flocculent and grand design spiral structure in field, binary and group galaxies. *Monthly Notices of the Royal Astronomical Society*, v. 201, p. 1021–1034, 1982.

ELMEGREEN, D. M.; ELMEGREEN, B. G. Arm classifications for spiral galaxies. *Astrophysical Journal*, v. 314, p. 3–9, 1987.

ERWIN, P. Double-barred galaxies. I. A catalog of barred galaxies with stellar secondary bars and inner disks. *Astronomy & Astrophysics*, v. 415, p. 941–957, 2004. Available from Internet: <<https://doi.org/10.1051/0004-6361:20034408>>.

ERWIN, P. IMFIT: A Fast, Flexible New Program for Astronomical Image Fitting. *The Astrophysical Journal*, v. 799, p. 226, 2015.

ERWIN, P.; POHLEN, M.; BECKMAN, J. E. The Outer Disks of Early-Type Galaxies. I. Surface-Brightness Profiles of Barred Galaxies. *The Astronomical Journal*, v. 135, p. 20–54, 2008. Available from Internet: <<https://doi.org/10.1088%2F0004-6256%2F135%2F1%2F20>>.

ERWIN, P.; SPARKE, L. S. An imaging survey of early-type barred galaxies. *The Astrophysical Journal Supplement Series*, IOP Publishing, v. 146, n. 2, p. 299–352, 2003. Available from Internet: <<https://doi.org/10.1086%2F367885>>.

ESKRIDGE, P. B. et al. Near-infrared and optical morphology of spiral galaxies. *The Astrophysical Journal Supplement Series*, IOP Publishing, v. 143, n. 1, p. 73–III, 2002. Available from Internet: <<https://doi.org/10.1086%2F342340>>.

FALCON-BARROSO, J.; KNAPEN, s. J. *Secular Evolution of Galaxies*. [S.l.]: Cambridge University Press, 2013. (Canary Islands Winter School of Astrophysics). ISBN 978-1-107-03527-0.

FERRARI, F.; CARVALHO, R. R. de; TREVISAN, M. Morfometryka – A New Way of Establishing Morphological Classification of Galaxies. *The Astrophysical Journal*, v. 814, p. 55, 2015.

FERRARI, F. et al. The relationship between the Sérsic law profiles measured along the major and minor axes of elliptical galaxies. *Monthly Notices of the Royal Astronomical Society*, v. 347, n. 3, p. 824–832, 2004. ISSN 0035-8711. Available from Internet: <<https://dx.doi.org/10.1111/j.1365-2966.2004.07254.x>>.

FIRMANI, C.; AVILA-REESE, V. Physical processes behind the morphological Hubble sequence. In: Avila-Reese, V. et al. (Ed.). *Revista Mexicana de Astronomia y Astrofisica Conference Series*. [S.l.: s.n.], 2003. (Revista Mexicana de Astronomia y Astrofisica, vol. 27, v. 17), p. 107–120.

FISCHER, J.-L.; BERNARDI, M.; MEERT, A. Comparing pymorph and SDSS photometry – I. Background sky and model fitting effects. *Monthly Notices of the Royal Astronomical Society*, v. 467, n. 1, p. 490–500, 2017. ISSN 0035-8711. Available from Internet: <<https://doi.org/10.1093/mnras/stx136>>.

FISHER, D. Kinematic Profiles of SO Galaxies. *Astronomical Journal*, v. 113, p. 950, 1997.

FISHER, D. B.; DRORY, N. The Structure of Classical Bulges and Pseudobulges: the Link Between Pseudobulges and Sérsic Index. *The Astronomical Journal*, IOP Publishing, v. 136, n. 2, p. 773–839, 2008. Available from Internet: <<https://doi.org/10.1088%2F0004-6256%2F136%2F2%2F773>>.

FISHER, D. B.; DRORY, N. Bulges of nearby galaxies with spitzer: Scaling relations in pseudobulges and classical bulges. *The Astrophysical Journal*, IOP Publishing, v. 716, n. 2, p. 942–969, 2010. Available from Internet: <<https://doi.org/10.1088%2F0004-637X%2F716%2F2%2F942>>.

- FISHER, D. B.; DRORY, N.; FABRICIUS, M. H. Bulges of nearby galaxies with spitzer: The growth of pseudobulges in disk galaxies and its connection to outer disks. *The Astrophysical Journal*, IOP Publishing, v. 697, n. 1, p. 630–650, 2009. Available from Internet: <<https://doi.org/10.1088%2F0004-637X%2F697%2F1%2F630>>.
- FREEMAN, K. C. On the Disks of Spiral and so Galaxies. *The Astrophysical Journal*, v. 160, p. 811, 1970.
- GADOTTI, D. A. Image decomposition of barred galaxies and AGN hosts. *Monthly Notices of the Royal Astronomical Society*, v. 384, n. 1, p. 420–439, 2008. ISSN 0035-8711. Available from Internet: <<https://doi.org/10.1111/j.1365-2966.2007.12723.x>>.
- GADOTTI, D. A. Structural properties of pseudo-bulges, classical bulges and elliptical galaxies: a Sloan Digital Sky Survey perspective. *Monthly Notices of the Royal Astronomical Society*, v. 393, p. 1531–1552, 2009.
- GADOTTI, D. A. et al. Near-infrared surface photometry of a sample of barred galaxies. *Monthly Notices of the Royal Astronomical Society*, v. 381, p. 943–961, 2007.
- Gadotti, D. A.; de Souza, R. E. On the Lengths, Colors, and Ages of 18 Face-on Bars. *The Astrophysical Journal Supplement Series*, v. 163, p. 270–281, 2006.
- GAO, H.; HO, L. C. An Optimal Strategy for Accurate Bulge-to-disk Decomposition of Disk Galaxies. *The Astrophysical Journal*, v. 845, p. 114, 2017.
- GRAHAM, A. W.; DRIVER, S. P. A Concise Reference to (Projected) Sérsic $R^{1/n}$ Quantities, Including Concentration, Profile Slopes, Petrosian Indices, and Kron Magnitudes. *Publications of the Astronomical Society of Australia*, v. 22, p. 118–127, 2005.
- GRAHAM, A. W. et al. A New Empirical Model for the Structural Analysis of Early-Type Galaxies, and A Critical Review of the Nuker Model. *The Astronomical Journal*, v. 125, p. 2951–2963, 2003.
- GROSSI, M. et al. Bulgeless galaxies in the COSMOS field: environment and star formation evolution at $z < 1$. *Monthly Notices of the Royal Astronomical Society*, v. 475, n. 1, p. 735–747, 2018.
- GUEDES, J. et al. Pseudobulge formation as a dynamical rather than a secular process. *The Astrophysical Journal*, IOP Publishing, v. 772, n. 1, p. 36, 2013. Available from Internet: <<https://doi.org/10.1088%2F0004-637X%2F772%2F1%2F36>>.
- HAUSSLER, B. et al. GEMS: Galaxy fitting catalogs and testing parametric galaxy fitting codes: GALFIT and GIM2d. *The Astrophysical Journal Supplement Series*, IOP Publishing, v. 172, n. 2, p. 615–633, 2007. Available from Internet: <<https://doi.org/10.1088%2F0067-0049%2F172%2F2%2F615>>.
- HEAD, J. T. C. G.; LUCEY, J. R.; HUDSON, M. J. Beyond Sérsic + exponential disc morphologies in the Coma Cluster. *Monthly Notices of the Royal Astronomical Society*, v. 453, n. 4, p. 3729–3753, 2015. ISSN 0035-8711. Available from Internet: <<https://dx.doi.org/10.1093/mnras/stv1662>>.
- HINZ, J. L.; RIEKE, G. H.; CALDWELL, N. The tully-fisher relation in coma and virgo cluster so galaxies. *The Astronomical Journal*, IOP Publishing, v. 126, n. 6, p. 2622–2634, 2003. Available from Internet: <<https://doi.org/10.1086%2F379555>>.
- HOPKINS, P. F. et al. Mergers and bulge formation in Λ cdm: Which mergers matter. *The Astrophysical Journal*, IOP Publishing, v. 715, n. 1, p. 202–229, 2010. Available from Internet: <<https://doi.org/10.1088%2F0004-637X%2F715%2F1%2F202>>.

HUBBLE, E. P. Extragalactic nebulae. *The Astrophysical Journal*, v. 64, 1926.

HUBBLE, E. P. *Realm of the Nebulae*. [S.l.: s.n.], 1936. ISBN 9780300025002.

HÄUFLER, B. et al. MegaMorph – multiwavelength measurement of galaxy structure: complete Sérsic profile information from modern surveys. *Monthly Notices of the Royal Astronomical Society*, v. 430, n. 1, p. 330–369, 2013. ISSN 0035-8711. Available from Internet: <<https://dx.doi.org/10.1093/mnras/sts633>>.

JAFFE, W. A simple model for the distribution of light in spherical galaxies. *Monthly Notices of the Royal Astronomical Society*, v. 202, p. 995–999, 1983.

JEDRZEJEWSKI, R. I. CCD surface photometry of elliptical galaxies – I. Observations, reduction and results. *Monthly Notices of the Royal Astronomical Society*, v. 226, n. 4, p. 747–768, 1987. ISSN 0035-8711. Available from Internet: <<https://dx.doi.org/10.1093/mnras/226.4.747>>.

JONG, R. S. D. et al. Structural properties of discs and bulges of early-type galaxies. *Monthly Notices of the Royal Astronomical Society*, v. 355, n. 4, p. 1155–1170, 2004. ISSN 0035-8711. Available from Internet: <<https://dx.doi.org/10.1111/j.1365-2966.2004.08394.x>>.

JONG, R. S. de. Near-infrared and optical broadband surface photometry of 86 face-on disk dominated galaxies. II. A two-dimensional method to determine bulge and disk parameters. *Astronomy and Astrophysics Supplement*, v. 118, p. 557–573, 1996.

JUNGWIERT, B.; COMBES, F.; AXON, D. J. Near-IR photometry of disk galaxies: Search for nuclear isophotal twist and double bars. *Astronomy & Astrophysics Supplement series*, v. 125, p. 479–496, 1997. Available from Internet: <<https://doi.org/10.1051/aas:1997236>>.

KAUFFMANN, G.; WHITE, S. D. M.; GUIDERDONI, B. The formation and evolution of galaxies within merging dark matter haloes. *Monthly Notices of the Royal Astronomical Society*, v. 264, n. 1, p. 201–218, 1993. ISSN 0035-8711. Available from Internet: <<https://doi.org/10.1093/mnras/264.1.201>>.

KAVIRAJ, S. et al. The Horizon-AGN simulation: evolution of galaxy properties over cosmic time. *Monthly Notices of the Royal Astronomical Society*, v. 467, n. 4, p. 4739–4752, 2017. ISSN 0035-8711. Available from Internet: <<https://doi.org/10.1093/mnras/stx126>>.

KEEL, W. C. Berlin, Heidelberg: Springer Berlin Heidelberg, 2007. ISBN 978-3-540-72535-0. Available from Internet: <<https://doi.org/10.1007/978-3-540-72535-0>>.

KEEL, W. C.; OSWALT, T. D. *Planets, Stars and Stellar Systems: Volume 6: Extragalactic Astronomy and Cosmology*. 2013. ed. [S.l.]: Springer, 2013. ISBN 9400756089, 9789400756083.

KENT, S. M. CCD surface photometry of field Galaxies. II - Bulge/disk decompositions. *Astrophysical Journal Supplement Series*, v. 59, p. 115–159, 1985.

KESELMAN, J. A.; NUSSER, A. Pseudo-bulge formation via major mergers. *Monthly Notices of the Royal Astronomical Society*, v. 424, n. 2, p. 1232–1243, 2012. ISSN 0035-8711. Available from Internet: <<https://doi.org/10.1111/j.1365-2966.2012.21300.x>>.

KIM, T. et al. Early-type galaxies with tidal debris and their scaling relations in the spitzer survey of stellar structure in galaxies (s⁴g). *The Astrophysical Journal*, IOP Publishing, v. 753, n. 1, p. 43, 2012. Available from Internet: <<https://doi.org/10.1088%2F0004-637X%2F753%2F1%2F43>>.

KING, I. The structure of star clusters. I. an empirical density law. *Astronomical Journal*, v. 67, p. 471, 1962.

KORMENDY, J.; BENDER, R. A Revised Parallel-sequence Morphological Classification of Galaxies: Structure and Formation of So and Spheroidal Galaxies. *The Astrophysical Journal Supplement*, v. 198, p. 2, 2012.

KORMENDY, J. et al. HST Photometry of the Cores of Early-Type Galaxies. In: Meylan, G.; Prugniel, P. (Ed.). *European Southern Observatory Conference and Workshop Proceedings*. [S.l.: s.n.], 1994. (European Southern Observatory Conference and Workshop Proceedings, v. 49), p. 147.

KORMENDY, J.; KENNICUTT JR., R. C. Secular Evolution and the Formation of Pseudobulges in Disk Galaxies. *Annual Review of Astronomy & Astrophysics*, v. 42, p. 603–683, 2004.

LACEY, C. Semi-Analytical Models of Galaxy Formation. In: Umemura, M.; Susa, H. (Ed.). *The Physics of Galaxy Formation*. [S.l.: s.n.], 2001. (Astronomical Society of the Pacific Conference Series, v. 222), p. 273.

LACKNER, C. N.; GUNN, J. E. Astrophysically motivated bulge-disc decompositions of Sloan Digital Sky Survey galaxies. *Monthly Notices of the Royal Astronomical Society*, v. 421, p. 2277–2302, 2012.

LAUER, T. R. et al. The Centers of Early-Type Galaxies with HST.I.An Observational Survey. *Astronomical Journal*, v. 110, p. 2622, 1995.

LAUER, T. R. et al. The Centers of Early-Type Galaxies with Hubble Space Telescope. VI. Bimodal Central Surface Brightness Profiles. *The Astrophysical Journal*, v. 664, p. 226–256, 2007.

LAURIKAINEN, E.; PELETIER, R.; GADOTTI, D. e. *Galactic Bulges*. 1. ed. Springer International Publishing, 2016. (Astrophysics and Space Science Library 418). ISBN 978-3-319-19377-9, 978-3-319-19378-6. Available from Internet: <<https://www.springer.com/gp/book/9783319193779>>.

LAURIKAINEN, E.; SALO, H. Barlenses and X-shaped features compared: two manifestations of boxy/peanut bulges. *Astronomy & Astrophysics*, v. 598, p. A10, 2017. Available from Internet: <<https://doi.org/10.1051/0004-6361/201628936>>.

LAURIKAINEN, E. et al. Morphology of 15 southern early?type disk galaxies. *The Astronomical Journal*, IOP Publishing, v. 132, n. 6, p. 2634–2652, 2006. Available from Internet: <<https://doi.org/10.1086%2F508810>>.

LAURIKAINEN, E. et al. Photometric scaling relations of lenticular and spiral galaxies. *Monthly Notices of the Royal Astronomical Society*, v. 405, n. 2, p. 1089–1118, 2010. ISSN 0035-8711. Available from Internet: <<https://dx.doi.org/10.1111/j.1365-2966.2010.16521.x>>.

LEE, J. et al. Local curvature analysis for classifying breast tumors: Preliminary analysis in dedicated breast CT. *Medical Physics*, v. 42, p. 5479–5489, 2015.

LI, Z.-Y. et al. THE CARNEGIE-IRVINE GALAXY SURVEY. II. ISOPHOTAL ANALYSIS. *The Astrophysical Journal Supplement Series*, IOP Publishing, v. 197, n. 2, p. 22, 2011. Available from Internet: <<https://doi.org/10.1088%2F0067-0049%2F197%2F2%2F22>>.

LIN, Q.; OU, C. Tsallis entropy and the long-range correlation in image thresholding. *Signal Processing*, v. 92, p. 2931–2939, 2012.

LOTZ, J. M.; PRIMACK, J.; MADAU, P. A New Nonparametric Approach to Galaxy Morphological Classification. *The Astronomical Journal*, v. 128, p. 163–182, 2004.

LUCATELLI, G.; FERRARI, F. Morfometria paramétrica e não paramétrica em imagens simuladas de galáxias: Um estudo do Índice concentração das quantidades efetivas de sérsic. Trabalho de Conclusão de Curso. 2016.

LUDERS, E. et al. A curvature-based approach to estimate local gyration on the cortical surface. *NeuroImage*, v. 29, n. 4, p. 1224 – 1230, 2006. ISSN 1053-8119. Available from Internet: <<http://www.sciencedirect.com/science/article/pii/S1053811905006543>>.

LYNDEN-BELL, D. The chemical evolution of galaxies. *Vistas in Astronomy*, v. 19, p. 299 – 316, 1975. ISSN 0083-6656. Available from Internet: <<http://www.sciencedirect.com/science/article/pii/0083665675900057>>.

MALIN, D. F. Unsharp masking. *AAS Photo Bulletin*, v. 16, p. 10–13, 1977.

MARTIN, G. et al. The formation and evolution of low-surface-brightness galaxies. *Monthly Notices of the Royal Astronomical Society*, v. 485, n. 1, p. 796–818, 2019. ISSN 0035-8711. Available from Internet: <<https://doi.org/10.1093/mnras/stz356>>.

MATTEUCCI, F. *Chemical Evolution of Galaxies*. 1. ed. Springer-Verlag Berlin Heidelberg, 2012. (Astronomy and Astrophysics Library). ISBN 3642224903, 9783642224904. Available from Internet: <<http://gen.lib.rus.ec/book/index.php?md5=551ee3c35d3b41021b63fd26cd648374>>.

MEERT, A.; BERNARDI, M.; VIKRAM, V. Simulations of single- and two-component galaxy decompositions for spectroscopically selected galaxies from the Sloan Digital Sky Survey. *Monthly Notices of the Royal Astronomical Society*, v. 433, n. 2, p. 1344–1361, 2013. ISSN 0035-8711. Available from Internet: <<https://dx.doi.org/10.1093/mnras/stt822>>.

MÉNDEZ-ABREU, J. et al. Morpho-kinematic properties of field So bulges in the CALIFA survey. *Monthly Notices of the Royal Astronomical Society*, v. 474, n. 1, p. 1307–1334, 2017. ISSN 0035-8711. Available from Internet: <<https://dx.doi.org/10.1093/mnras/stx2804>>.

MEURER, G. R. et al. The survey for ionization in neutral gas galaxies. i. description and initial results. *The Astrophysical Journal Supplement Series*, IOP Publishing, v. 165, n. 1, p. 307–337, 2006. Available from Internet: <<https://doi.org/10.1086%2F504685>>.

MILONE, A. D. C.; RICKES, M. G.; PASTORIZA, M. G. The elliptical galaxies NGC 1052 and NGC 7796. Stellar populations and abundance ratio α/Fe . *Astronomy & Astrophysics*, v. 469, p. 89–113, 2007. Available from Internet: <<https://doi.org/10.1051/0004-6361:20054615>>.

MO, H.; BOSCH, F. van den; WHITE, S. *Galaxy Formation and Evolution*. 1. ed. [S.l.]: Cambridge University Press, 2010. ISBN 0521857937, 9780521857932.

MOISEEV, A. V.; VALDÉS, J. R.; CHAVUSHYAN, V. H. Structure and kinematics of candidate double-barred galaxies. *Astronomy & Astrophysics*, v. 421, p. 433–453, 2004. Available from Internet: <<https://doi.org/10.1051/0004-6361:20040045>>.

MOLAEINEZHAD, A. et al. The imprints of bars on the vertical stellar population gradients of galactic bulges. *Monthly Notices of the Royal Astronomical Society*, v. 467, p. 353–368, 2017.

MORGAN, W. W. A Preliminary Classification of the Forms of Galaxies According to Their Stellar Population. *Publications of the Astronomical Society of the Pacific*, v. 70, p. 364, 1958.

MORGAN, W. W. Preliminary Classification of the Forms of Galaxies According to Their Stellar Population. II. *Publications of the Astronomical Society of the Pacific*, v. 71, p. 394, 1959.

- MULCHAEY, J. S.; REGAN, M. W.; KUNDU, A. The fueling of nuclear activity. i. a near-infrared imaging survey of seyfert and normal galaxies. *The Astrophysical Journal Supplement Series*, IOP Publishing, v. 110, n. 2, p. 299–319, 1997. Available from Internet: <<https://doi.org/10.1086%2F313005>>.
- MUÑOZ-MATEOS, J. C. et al. The impact of bars on disk breaks as probed by s^4g imaging. *The Astrophysical Journal*, IOP Publishing, v. 771, n. 1, p. 59, 2013. Available from Internet: <<https://doi.org/10.1088%2F0004-637X%2F771%2F1%2F59>>.
- NAAB, T.; OSTRIKER, J. P. Theoretical Challenges in Galaxy Formation. *Annual Review of Astronomy and Astrophysics*, v. 55, n. 1, p. 59–109, 2017.
- NAAB, T.; TRUJILLO, I. Surface density profiles of collisionless disc merger remnants. *Monthly Notices of the Royal Astronomical Society*, v. 369, n. 2, p. 625–644, 2006. ISSN 0035-8711. Available from Internet: <<https://doi.org/10.1111/j.1365-2966.2006.10252.x>>.
- NAIR, P. B.; ABRAHAM, R. G. A Catalog of Detailed Visual Morphological Classifications for 14,034 Galaxies in the Sloan Digital Sky Survey. *The Astrophysical Journal Supplement Series*, v. 186, p. 427–456, 2010.
- NILSON, P. Uppsala General Catalogue of Galaxies, 1973, Acta Universitatis Upsaliensis, Nova Regiae Societatis Upsaliensis, Series v: a Vol. *Nova Acta Regiae Soc. Sci. Upsaliensis Ser. V*, 1973.
- PAGEL, B. E. J. Chemical evolution of galaxies. *Publications of the Astronomical Society of the Pacific*, IOP Publishing, v. 113, n. 780, p. 137–141, 2001. Available from Internet: <<https://doi.org/10.1086%2F318608>>.
- PAGEL, B. E. J. *Nucleosynthesis and Chemical Evolution of Galaxies*. 2nd. ed. Cambridge University Press, 2009. ISBN 9780511812170. Available from Internet: <<http://gen.lib.rus.ec/book/index.php?md5=1C755AAFDD3C77275B6C174A142055CD>,<https://www.cambridge.org/core/books/nucleosynthesis-and-chemical-evolution-of-galaxies/D8362A57B1DE75D98470350FE167123E>>.
- PENG, C. Y. et al. Detailed Structural Decomposition of Galaxy Images. *The Astronomical Journal*, v. 124, p. 266–293, 2002.
- PENG, C. Y. et al. Detailed Decomposition of Galaxy Images. II. Beyond Axisymmetric Models. *The Astronomical Journal*, v. 139, p. 2097–2129, 2010.
- PÉREZ, I.; SÁNCHEZ-BLÁZQUEZ, P.; ZURITA, A. Study of the stellar line-strength indices and kinematics along bars. I. Bar age and metallicity gradients. *Astronomy & Astrophysics*, v. 495, p. 775–794, 2009. Available from Internet: <<https://doi.org/10.1051/0004-6361:200811084>>.
- PETROSIAN, V. Surface brightness and evolution of galaxies. *The Astrophysical Journal*, v. 209, p. L1–L5, 1976.
- PLUMMER, H. C. On the problem of distribution in globular star clusters. *Monthly Notices of the Royal Astronomical Society*, v. 71, p. 460–470, 1911.
- POGGE, R. W.; MARTINI, P. Hubble space telescope imaging of the circumnuclear environments of the cfa seyfert galaxies: Nuclear spirals and fueling. *The Astrophysical Journal*, IOP Publishing, v. 569, n. 2, p. 624–640, 2002. Available from Internet: <<https://doi.org/10.1086%2F339400>>.
- PRANTZOS, N. An Introduction to Galactic Chemical Evolution. In: Charbonnel, C.; Zahn, J. P. (Ed.). *EAS Publications Series*. [S.l.: s.n.], 2008. (EAS Publications Series, v. 32), p. 311–356.

PREIM, B.; BOTHA, C. P. *Visual Computing for Medicine. Theory, Algorithms, and Applications*. 2. ed. [S.l.]: Morgan Kaufmann, 2014. ISBN 978-0-12-415873-3.

PRIETO, M. et al. Optical surface photometry of a sample of disk galaxies. II. Structural components. *Astronomy and Astrophysics*, v. 367, p. 405–427, 2001.

RAMÍREZ-REYES, A. et al. Determining the entropic index q of tsallis entropy in images through redundancy. *Entropy*, v. 18, n. 8, 2016. ISSN 1099-4300. Available from Internet: <<http://www.mdpi.com/1099-4300/18/8/299>>.

REYNOLDS, J. H. hubble1926. *Monthly Notices of the Royal Astronomical Society*, v. 80, p. 746, 1920.

RÍO, M. S. del; CEPA, J. The nature of arms in spiral galaxies. III. Azimuthal profiles. *Astronomy & Astrophysics*, v. 340, p. 1–20, 1998.

RÍO, M. S. del; CEPA, J. The nature of arms in spiral galaxies. IV. Symmetries and asymmetries. *Astronomy and Astrophysics Supplement Series*, v. 134, p. 333–358, 1999. Available from Internet: <<https://doi.org/10.1051/aas:1999440>>.

ROBOTHAM, A. S. G. et al. PROFIT: Bayesian profile fitting of galaxy images. *Monthly Notices of the Royal Astronomical Society*, v. 466, p. 1513–1541, 2017.

RODRIGUES, P. S.; GIRALDI, G. A. Computing the q-index for tsallis nonextensive image segmentation. In: IEEE. *Computer Graphics and Image Processing (SIBGRAPI), 2009 XXII Brazilian Symposium on*. [S.l.], 2009. p. 232–237.

SAGLIA, R. P. et al. The peculiar motions of early-type galaxies in two distant regions. IV. the photometric fitting procedure. *The Astrophysical Journal Supplement Series*, IOP Publishing, v. 109, n. 1, p. 79–102, 1997. Available from Internet: <<https://doi.org/10.1086%2F312978>>.

SALO, H.; LAURIKAINEN, E.; BUTA, R. Multicomponent decompositions for a sample of So galaxies. *Monthly Notices of the Royal Astronomical Society*, v. 362, n. 4, p. 1319–1347, 2005. ISSN 0035-8711. Available from Internet: <<https://dx.doi.org/10.1111/j.1365-2966.2005.09404.x>>.

SALO, H. et al. The Spitzer Survey of Stellar Structure in Galaxies (S⁴G): Multi-component Decomposition Strategies and Data Release. *The Astrophysical Journal Supplement Series*, v. 219, p. 4, 2015.

SANDAGE, A. *The Hubble atlas of galaxies*. [S.l.: s.n.], 1961.

SANDAGE, A.; SANDAGE, M.; KRISTIAN, J. *Galaxies and the Universe*. [S.l.: s.n.], 1975.

SANDAGE, A.; TAMMANN, G. A. *A Revised Shapley-Ames Catalog of Bright Galaxies*. [S.l.: s.n.], 1981.

SANI, E. et al. The Spitzer/IRAC view of black hole–bulge scaling relations. *Monthly Notices of the Royal Astronomical Society*, v. 413, n. 2, p. 1479–1494, 2011. ISSN 0035-8711. Available from Internet: <<https://dx.doi.org/10.1111/j.1365-2966.2011.18229.x>>.

SCHAYE, J. et al. The EAGLE project: simulating the evolution and assembly of galaxies and their environments. *Monthly Notices of the Royal Astronomical Society*, v. 446, p. 521–554, 2015.

SÉRSIC, J. L. Influence of the atmospheric and instrumental dispersion on the brightness distribution in a galaxy. *Boletín de la Asociación Argentina de Astronomía La Plata Argentina*, v. 6, p. 41, 1963. Available from Internet: <<http://www.astronomiaargentina.org.ar/b06/1963BAAA....6...41S.pdf>>.

- SÉRSIC, J. L. *Atlas de galaxias australes*. [S.l.: s.n.], 1968.
- SHANNON, C. E.; WEAVER, W. *The mathematical theory of communication*. [S.l.: s.n.], 1949.
- SHETH, K. et al. The spitzersurvey of stellar structure in galaxies (s4g). *Publications of the Astronomical Society of the Pacific*, IOP Publishing, v. 122, n. 898, p. 1397–1414, 2010. Available from Internet: <<https://doi.org/10.1086%2F657638>>.
- SIMARD, L. et al. A Catalog of Bulge+disk Decompositions and Updated Photometry for 1.12 Million Galaxies in the Sloan Digital Sky Survey. *The Astrophysical Journal Supplement*, v. 196, p. 11, 2011.
- SIMARD, L. et al. The DEEP Groth Strip Survey. II. Hubble Space Telescope Structural Parameters of Galaxies in the Groth Strip. *The Astrophysical Journal Supplement Series*, v. 142, p. 1–33, 2002.
- SOMERVILLE, R. S.; PRIMACK, J. R. Semi-analytic modelling of galaxy formation: the local Universe. *Monthly Notices of the Royal Astronomical Society*, v. 310, n. 4, p. 1087–1110, 1999. ISSN 0035-8711. Available from Internet: <<https://doi.org/10.1046/j.1365-8711.1999.03032.x>>.
- SOUZA, R. E. de; GADOTTI, D. A.; ANJOS, S. dos. BUDDA: A New Two-dimensional Bulge/Disk Decomposition Code for Detailed Structural Analysis of Galaxies. *The Astrophysical Journal Supplement Series*, v. 153, p. 411–427, 2004.
- SPRINGEL, V. et al. Simulations of the formation, evolution and clustering of galaxies and quasars. *Nature*, v. 435, p. 629–636, 2005.
- TARENghi, M.; GARILLI, B.; MACCAGNI, D. Galaxy structures in the Hercules region. *The Astronomical Journal*, v. 107, p. 1629–1636, 1994.
- TASCA, L. A. Bulge-to-disk decomposition of large galaxies in the sloan digital sky survey. 2004. Available from Internet: <<http://nbn-resolving.de/urn:nbn:de:bvb:19-27040>>.
- TASCA, L. A. M.; WHITE, S. D. M. Quantitative morphology of galaxies from the SDSS. I. Luminosity in bulges and discs. *Astronomy and Astrophysics*, v. 530, p. A106, 2011.
- TENENBLAT, K. *Introdução à geometria diferencial*. 2nd. ed. [S.l.]: Edgard Blucher, 2008. ISBN 8521204671, 9788521204671.
- TONINI, C. et al. The growth of discs and bulges during hierarchical galaxy formation – II. Metallicity, stellar populations and dynamical evolution. *Monthly Notices of the Royal Astronomical Society*, v. 465, n. 4, p. 4133–4146, 2016. ISSN 0035-8711. Available from Internet: <<https://doi.org/10.1093/mnras/stw3053>>.
- TOOMRE, A.; TOOMRE, J. Galactic Bridges and Tails. *The Astrophysical Journal*, v. 178, p. 623–666, 1972.
- TRUJILLO, I. et al. Evidence for a New Elliptical-Galaxy Paradigm: Sérsic and Core Galaxies. *The Astronomical Journal*, v. 127, p. 1917–1942, 2004.
- TRUJILLO, I.; GRAHAM, A. W.; CAON, N. On the estimation of galaxy structural parameters: the Sérsic model. *Monthly Notices of the Royal Astronomical Society*, v. 326, p. 869–876, 2001.
- TSALLIS, C. Possible generalization of Boltzmann-Gibbs statistics. *Journal of Statistical Physics*, v. 52, p. 479–487, 1988.

- TSALLIS, C. *Introduction to nonextensive statistical mechanics: approaching a complex world*. 1. ed. Springer-Verlag New York, 2009. ISBN 0387853588, 9780387853581. Available from Internet: <<http://gen.lib.rus.ec/book/index.php?md5=7ABfEE&D51B09944396AC6F09A52315C>>.
- VAUCOULEURS, G. Classification and Morphology of External Galaxies. *Handbuch der Physik*, v. 53, p. 275–310, 1959.
- VAUCOULEURS, G. de. General Physical Properties of External Galaxies. *Handbuch der Physik*, v. 53, p. 311, 1959.
- VAUCOULEURS, G. de et al. *Third Reference Catalogue of Bright Galaxies. Volume I: Explanations and references. Volume II: Data for galaxies between 0^b and 12^b. Volume III: Data for galaxies between 12^b and 24^b*. [S.l.: s.n.], 1991.
- VIKA, M. et al. MegaMorph – multiwavelength measurement of galaxy structure. Sérsic profile fits to galaxies near and far. *Monthly Notices of the Royal Astronomical Society*, v. 435, n. 1, p. 623–649, 2013. ISSN 0035-8711. Available from Internet: <<https://dx.doi.org/10.1093/mnras/stt1320>>.
- VIKA, M. et al. The near-IR Mbh–L and Mbh–n relations. *Monthly Notices of the Royal Astronomical Society*, v. 419, n. 3, p. 2264–2292, 2012. ISSN 0035-8711. Available from Internet: <<https://dx.doi.org/10.1093/mnras/stt1320>>.
- VOGELSBERGER, M. et al. Introducing the Illustris Project: simulating the coevolution of dark and visible matter in the Universe. *Monthly Notices of the Royal Astronomical Society*, v. 444, n. 2, p. 1518–1547, 2014. ISSN 0035-8711. Available from Internet: <<https://doi.org/10.1093/mnras/stt1320>>.
- WHITE, S. D. M.; FRENK, C. S. Galaxy formation through hierarchical clustering. *Astrophysical Journal*, v. 379, p. 52–79, 1991.
- WHITE, S. D. M.; REES, M. J. Core condensation in heavy halos - A two-stage theory for galaxy formation and clustering. *Monthly Notices of the Royal Astronomical Society*, v. 183, p. 341–358, 1978.
- WOZNIAK, H.; PIERCE, M. J. CCD surface photometry of early-type barred galaxies. I - Data reduction and results. *Astronomy and Astrophysics Supplement Series*, v. 88, p. 325–348, 1991.
- WYSE, R. F. G.; GILMORE, G.; FRANX, M. Galactic Bulges. *Annual Review of Astronomy and Astrophysics*, v. 35, p. 637–675, 1997.
- YILDIRIM, A. et al. The structural and dynamical properties of compact elliptical galaxies. *Monthly Notices of the Royal Astronomical Society*, v. 468, p. 4216–4245, 2017.
- ZHANG, J. *Medicine Sciences and Bioengineering: Proceedings of the 2014 International Conference on Medicine Sciences and Bioengineering*. [S.l.]: CRC Press, 2015. (ICMSB2014). ISBN 978-1-138-02684-1, 978-1-315-73451-4, 1138026840.
- ZHAO, D.; ARAGÓN-SALAMANCA, A.; CONSELICE, C. J. The link between morphology and structure of brightest cluster galaxies: automatic identification of cDs. *Monthly Notices of the Royal Astronomical Society*, v. 448, n. 3, p. 2530–2545, 2015. ISSN 0035-8711. Available from Internet: <<https://dx.doi.org/10.1093/mnras/stv190>>.
- ZHAO, D. H. et al. The growth and structure of dark matter haloes. *Monthly Notices of the Royal Astronomical Society*, v. 339, n. 1, p. 12–24, 2003. ISSN 0035-8711. Available from Internet: <<https://doi.org/10.1046/j.1365-8711.2003.06135.x>>.

Appendix

A

Article I (submitted)

Galaxy Structural Analysis with the Curvature of the Brightness Profile

Geferson Lucatelli,¹★ Fabricio Ferrari,¹†

¹*Instituto de Matemática Estatística e Física – IMEF, Universidade Federal do Rio Grande – FURG, Rio Grande, RS, Brasil.*

Accepted XXX. Received YYY; in original form ZZZ

ABSTRACT

In this work we introduce the curvature of a galaxy brightness profile to non-parametrically identify its structural subcomponents. Bulges, bars, disks, lens, rings and spiral arms are a key to understanding the formation and evolution path the galaxy undertook. Identifying them is also crucial for morphological classification of galaxies. We measure and analyse in detail the curvature of 16 galaxies with varied morphology. High (low) steepness profiles show high (low) curvature measures. Transitions between components present local peaks oscillations in the values of the curvature. We identify patterns that characterise bulges (pseudo or classic), disks, bars, rings, spiral arms. The procedure can be automated to deal with large datasets and identify galaxy components automatically or to provide a reliable starting point for traditional multicomponent modelling of galaxy light distribution.

Key words: galaxies: morphometry – galaxies: fundamental parameters – galaxies: structure analysis – galaxies: photometry

1 INTRODUCTION

Galaxy formation and evolution are vital to understand the Universe as a whole, for galaxies portray the general structure where they emerged and evolved. Galaxy morphology provides us with a framework on which we describe galaxy structures that are connected with such evolution. The processes that gave birth to bulges, disks, bars, rings, arms, halos, for example, are imprinted in the properties or absence of these features.

Traditional understanding of galaxy formation and evolution encloses, basically, the distinction of the processes that origin elliptical galaxies and classical bulges from the formation of disk dominated/spiral galaxies and pseudobulges. The first mechanism are merger events having violent relaxations and hierarchical clustering (Toomre & Toomre 1972; Tonini et al. 2016; Naab & Trujillo 2006; Hopkins et al. 2010). In the merger scenario, it is established that elliptical galaxies are formed by major mergers of spiral galaxies (Burkert & Naab 2003). In the case of spiral, lenticular and irregular galaxies, first it was supposed that they are a result of formative evolution where rapid violent processes such as hierarchical clustering and merging led to the formation of them (White & Rees 1978; White & Frenk 1991; Firmani & Avila-Reese 2003; Buta 2013).

The physical properties of the galaxy components also bring relevant information regarding the history of the galaxy. Bulges can be formed by two different ways and therefore separated in two categories: classical originates from violent processes such as hierarchi-

cal clustering via minor mergers (Naab & Trujillo 2006; Hopkins et al. 2010; Gadotti 2009), are dynamically hot and posses similar properties of elliptical galaxies (Fisher & Drory 2008); pseudo originates from secular evolution through longer times scales where disk material is rearranged by bars and spiral structures in a slow steady process (Wyse et al. 1997; Firmani & Avila-Reese 2003; Kormendy & Kennicutt 2004; Athanassoula 2005; Guedes et al. 2013; Grossi et al. 2018). Characteristics of pseudo bulges are not found in elliptical galaxies and can be similar to those of disks, which are dynamically cold with the kinematics dominated by rotation (Fisher & Drory 2008). Even so, not all bulges can be clearly labelled as classic or pseudo, for there are bulges that present a mix of properties of the two types (Kormendy & Kennicutt 2004).

More recently, however, computer simulations such as (Springel et al. 2005; Dubois et al. 2014; Vogelsberger et al. 2014; Schaye et al. 2015; Kaviraj et al. 2017) (between others) allowed more profound studies on galaxy formation and evolution (Martin et al. 2019). Therefore the principles of the ideas commented above changed slightly and other assumptions raised. For example, to cite only: pseudobulges instead of being formed only by secular processes, can also be formed trough dynamical process (Guedes et al. 2013), and also from major mergers (Keselman & Nusser 2012; Grossi et al. 2018); dark matter haloes can also evolve in terms of two phases (not only by secular evolution), early by major mergers and later by minor mergers (Zhao et al. 2003; Diemand et al. 2007; Ascasibar & Gottlöber 2008).

Complementing these analysis, galaxy morphological classification helps recognise the process that drove the galaxy evolution Buta (2013). The first ideas were presented by Reynolds (1920) and later by Hubble (1936), who separated galaxies in classes con-

★ E-mail: glucatelli.astro.ph@furg.br

† E-mail: fabricio.ferrari@furg.br

2 Lucatelli & Ferrari

stituting the Hubble sequence - early to late types galaxies. Their classification, and the main procedures adopted in the XX Century, were based on visual examination of galaxy images. The procedures of classification gained in detail along the years, new parameters and schemes have been introduced but they remained based on the visual inspection of the image by an expert (Morgan 1958; de Vaucouleurs 1959; van den Bergh 1960a,b; Sandage 1961; van den Bergh 1976; Buta 2013).

Within this scheme of components as building blocks of galaxy structure, it is relevant to quantify which structures are present in a given galaxy and what is their contribution to the total galaxy light compared to other components. There are several ways to accomplish that, in general by modelling each component in an analytical fashion and then trying a combination of them that best describes the galaxy light distribution (Caon et al. 1993; Peng et al. 2002; Simard et al. 2002; de Souza et al. 2004; Erwin 2015, among others). This process can describe the galaxy photometry very precisely, however there are some drawbacks. In cases of multicomponent, which are the majority of galaxies, the minimisation data-model is numerically unstable and converges only with the assistance of an experienced user, which limits the range of the model parameters. Furthermore, the joint component models fitted to the galaxy can be degenerate for different combinations of the parameters (De Jong et al. 2004; Andrae et al. 2011; Sani et al. 2011; Meert et al. 2013), giving the same residuals within the photometric errors, and thus are inconclusive. In some cases leading to situations where they are not physically reasonable.

These restrictions can be overcome with user inspection, as mentioned. Nevertheless, the flood of photometric data that was been made available in the last two decades, for example since the first data release of SDSS (Abazajian et al. 2003) (to cite only one big survey) urged us to reinvent our basic methods and tools to appropriate from all the physical information contained in it. Thus, a method which can infer the basic properties of the components of a given galaxy automatically and non-parametrically could greatly increase the amount of information we could gather from the survey's data. In this way, we introduce the **curvature of the galaxy's brightness profile** $\kappa(R)$ with the purpose of inferring the galaxy's structural components.

The purpose in doing this is that $\kappa(R)$ may be used to identify if a galaxy is single or multicomponent, and in this case, it would inform the radial scale length of each component. This is possible because $\tilde{\kappa}$ calculated on the radial profile is a measure of its steepness, and a priori each component has its own. We argue that this new approach is more physically motivated than previously ones because it is independent of parameters. In this paper we are firstly introducing the concept and analysing the results in an non-automated way, the automation and improvements is left for a next paper.

This paper is structured as follows. In Section 2 briefly exposes approaches similar to ours. In Section 3 we introduce our approach for galaxy structural analysis and morphometry using the curvature. In 4 we discuss the data sample used. The application of the technique to the data is carried out in Section 5. In Sections 6 and 7 we discuss the results and summarize our results, respectively. Also, supplementary material is found in the Appendix Sections.

2 RELATED WORK

Several techniques to distinguish galaxy components have been developed over the years. Basically they are classified whether they

perform the modelling in the extracted brightness profile of the galaxy (1D modelling) or directly in the galaxy image (2D modelling). The most widespread 1D approach is to fit ellipses to a set of isophotes – an evolution of aperture photometry done at the telescope (Jedrzejewski 1987; Jungwiert et al. 1997; Erwin & Sparke 2003; Cabrera-Lavers & Garzón 2004; Erwin 2004; Laurikainen et al. 2005; Gadotti et al. 2007; Pérez et al. 2009).

For each isophote there is a collection of geometric and physical parameters that describe it, including the brightness profile (energy flux as a function of distance) which is later used to compare to a model of the components of the galaxy. As a side effect, this technique is often used to identify behaviour in the parameters (ellipticity, position angle, Fourier coefficients of the ellipse expansion) that may indicate the domain of different components or, in another context, to give hints of ancient interactions, mergers or cannibalism. Also with a similar purpose, other non-parametric approaches like unsharp masking (Malin 1977) (Erwin & Sparke 2003; Kim et al. 2012) and structure maps (Pogge & Martini 2002; Kim et al. 2012) are used.

Unidimensional techniques are better suited to extract geometric information of individual isophotes, but incorporating the instrument response function (the PSF – point spread function) is not trivial. Furthermore, there is no consensus on which distance coordinate to use to extract the profile – major or minor axis or different combination of both – whose choice impacts the leading parameters Ferrari et al. (2004).

Two-dimensional algorithms operate directly in the galaxy image, so there is no ambiguity in extracting the brightness profile. Real PSFs can be incorporated in the models and the process (convolution) in this conserves energy. Their disadvantage are the high computational cost – not so critical nowadays – and the instability to initial conditions. This instability raises wildly with the number of components and free parameters in the models. In some situations (e.g. a combination of bulge, bar and disc), the algorithm only converges if the initial parameters are very close to the final ones, which makes the algorithm itself unnecessary (see for example Haussler et al. 2007).

Regardless the method, 1D or 2D, the galaxy is then modelled with a combination of components, usually described with a Sérsic function (Sérsic 1968) with different n , scale lengths and intensity to resemble a bulge, a disk, a bar and so on. (See for example Caon et al. 1993; Peng et al. 2002; de Souza et al. 2004; Laurikainen et al. 2005; Gadotti 2008; Simard et al. 2011; Kormendy & Bender 2012; Bruce et al. 2014; Argyle et al. 2018; Erwin 2015, and references therein).

The curvature itself, as far as we know, has not been used in the context of galaxy structural analysis, nevertheless it has been used in different fields of science in a similar manner. In medicine, for example, it is used to recognize the existence of breast tumors (Lee et al. 2015), where it is applied on the imaging data of the photograph of each patient's breast in order to classify the tumors. Luders et al. (2006) used the curvature to study the process of brain gyration according genre, a process present on the cerebral cortex which forms folds, composed by peaks and valleys (see their methodology for details). They have used the mean curvature as a external measure of how the normal vector of the surface of the brain changes across it. The idea behind it is similar to ours, because here the curvature $\kappa(R)$ specifies how the normal vector of $I(R)$ changes along radius, giving information of what kind of component is present in each specific region of the profile. Other works using curvature were found on dental studies (Zhang 2015; Destrez et al. 2018) and in general medicine (Preim & Botha 2014).

3 CURVATURE OF THE BRIGHTNESS PROFILE

3.1 Definitions

With the purpose to identify galaxy substructures non-parametrically we introduce the **curvature of the brightness profile** $\kappa(R)$. The concept of curvature comes from differential geometry (e.g. Tenenblat 2008): given a function $f = f(x)$ it is possible to measure how it deviates from a straight line (the same reasoning can be extended to higher dimensional spaces) by means of a curvature measure on f , that is $\kappa[f(x)] \equiv \kappa(x)$. Here we take $f(x)$ to be the radial brightness profile $I(R)$ of the galaxy (more details below), thus

$$\kappa(R) = \frac{\frac{d^2 I(R)}{dR^2}}{\left[1 + \left(\frac{dI(R)}{dR} \right)^2 \right]^{3/2}}. \quad (1)$$

Equation (1) is a particular case when we have a one-dimensional continuous function. However, in this work we will deal with non-continuous quantities, which are the discrete data of light profiles of the galaxies. Therefore, we seek for a discrete curvature measure on our data which involves numerical operations. For two discrete vectors representing two quantities, say I and R , the curvature is defined as

$$\kappa = \frac{\delta R_i \delta^2 I_i - \delta I_i \delta^2 R_i}{(\delta R_i^2 + \delta I_i^2)^{3/2}} \quad (2)$$

where δ represents the numerical differentials (derivatives) between the discrete i -values of R and I .

The curvature at a point P in a curve S is inversely proportional to the osculating circle of radius \mathcal{R} bypassing through that same point whose surface normal vector points towards to the centre of the circle, that is $\kappa \propto 1/\mathcal{R}$ (see, for example, schematics in Crane et al. (2013); Lee et al. (2015)). This means that in any arbitrary scale, both x -axis and y -axis variables must have the same units. In other words, one variation in x need to have the same length as y (the norm of the basis vector must have the same length), consequently we can trace an osculating circle for a set of points near to a centred point P . Otherwise we would have an ellipse instead of a circle, and the curvature definition's does not hold any more, since it is not possible to drawn an osculating circle in the $x - y$ space.

This makes sense in defining the curvature of a spatial surface because x and y describes positions in that space. However, when these two quantities does not have the same physical meaning, like intensity I and radius R , some modifications are needed. Once established that, given two different quantities I and R with distinct scales, it is necessary to transform them into a space having equal metric. This is accomplished finding a normalization to the equations (1) and (2). An example of normalization is to confine both $I(R)$ and R to vary in an equal interval, for example the unitary one $[0, 1]$.

Before we proceed to the normalization, there is a particular result from the curvature for we should take into account: it is zero for a straight line and non zero for other general cases. A galactic disk generally follow an exponential profile (Freeman 1970) (see Appendix A). Then in log space, this profile is a straight line and we can conclude that the curvature of a disk in log space is close to zero. With this in mind we argue that is more useful to normalize the logarithm of $I(R)$, $\log[I(R)]$, instead of $I(R)$. Our point is that we will be able to easily distinguish disks from non disks using $\tilde{\kappa}$.

Hence a normalization $\nu(R)$ for $\log[I(R)]$ in the range $[0, 1]$ is

$$\nu(R) \equiv \frac{\log[I(R)] - \min(\log I)}{\max(\log I) - \min(\log I)}. \quad (3)$$

The next step is the normalization for R . We need to change the variation of the dimensional variable R to another quantity that is dimensionless and confine it in the range $[0, 1]$. Generally, observations do not reach the faintest parts of a galaxy, so it is usual to define a galaxy size. One common choice is the Petrosian radius R_p (Petrosian 1976), defined by the radius where the Petrosian function

$$\eta(R) = \frac{\langle I \rangle(R)}{I(R)} \quad (4)$$

has a definite value, i.e.

$$\eta(R_p) = \eta_0. \quad (5)$$

Here $\langle I \rangle(R)$ is the mean intensity inside R and $I(R)$ the intensity at R . Following (Bershady et al. 2000; Blanton et al. 2001; Ferrari et al. 2015) we use here $\eta_0 = 5$ with $2R_p$ as the size of galaxy. The normalization of R now reads

$$\chi = \frac{R}{2R_p}. \quad (6)$$

The curvature in terms of normalized variables measures the rate of change of $\nu(R)$ in terms of the new variable χ . So the complete normalized curvature is obtained taking the derivative of $\nu(R)$ with respect to χ . The relationship between the differentials of dR and $d\chi$ is

$$d\chi = \frac{dR}{2R_p}. \quad (7)$$

With

$$\frac{d\nu}{d\chi} = 2R_p \frac{d\nu}{dR} \quad \text{and} \quad \frac{d^2\nu}{d\chi^2} = 4R_p^2 \frac{d^2\nu}{dR^2} \quad (8)$$

we obtain the **normalized curvature** as

$$\tilde{\kappa}(R) = 4R_p^2 \frac{d^2\nu}{dR^2} \left[1 + 4R_p^2 \left(\frac{d\nu}{dR} \right)^2 \right]^{-3/2}. \quad (9)$$

We will use the expression (9) in Appendix A to derive the curvature for a Sérsic profile.

Returning to the discrete case in Eq. (2), the discrete normalized curvature in terms of the new variables is

$$\tilde{\kappa} = \frac{\delta \chi_i \delta^2 \nu_i - \delta \nu_i \delta^2 \chi_i}{(\delta \chi_i^2 + \delta \nu_i^2)^{3/2}}. \quad (10)$$

As an example, Figure Fig. 1 shows $\tilde{\kappa}$ measured for the EFIGI galaxy NGC 1211/PGC 11670 (see Section 3.3), together with the normalized profile $\nu(R)$ and the related derivatives of $\nu(R)$ (raw and filtered, see Section 3.3) used to calculate the curvature.

The rationale behind using the brightness profile curvature $\tilde{\kappa}$ to identify structural subcomponents in galaxy light is based on the fact that the curvature of disks will be null whilst that of bulges will be positive and dependent on its Sérsic index; regions highly affected by the PSF would tend to be negative in $\tilde{\kappa}$; the transition between different components would be manifested in curvature changes; galaxies with disks (either inner or outer) will present $\tilde{\kappa}$ that are zero over the region dominated by the disk (see next section). In Appendix A we work out the expressions for curvatures of Sérsic models (including disks). In Section 5 we develop this concepts in practice examining how $\tilde{\kappa}$ behaves for different combinations of galaxy subcomponents.

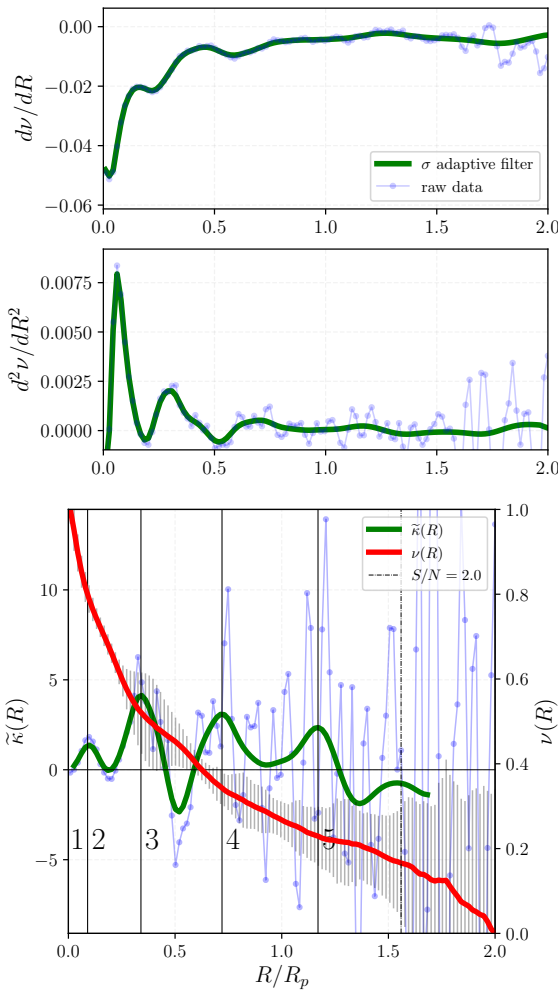


Figure 1. Example of the procedure to calculate $\tilde{\kappa}(R)$ for the EFIGI/SDSS data of galaxy NGC 1211/PGC 11670. **Top:** first derivative of $I(R)$, raw (blue) and filtered (green). **Middle:** the same but for the second derivative of $I(R)$. **Bottom:** log-normalized brightness profile $\nu(R)$ (red) and the raw (blue) and filtered (green) curvature. The filter is discussed in Section 3.3. The solid vertical lines represent the possible transition between regions dominated by different components, and will be explained latter on Section 5.1. The vertical dashed line delimit the regions where the signal-to-noise S/N goes below 2 and we avoid to interpret profiles outside that region.

3.2 Measuring $I(R)$ with MORFOMETRYKA

The brightness profile is measured as part of the processing done by MORFOMETRYKA (Ferrari et al. 2015). MORFOMETRYKA is an algorithm designed to perform several photometric and morphometric measurements on a galaxy image in an automated way with no user interaction. The inputs are the galaxy image stamp and respective point spread function (PSF) image. It then measures the background in an iterative way, segmentates the image – separating galaxy, other objects and background – and measure basic geometric parameters of the segmented region, like the centre, the position angle, major and minor axis. Based on this information, it performs aperture photometry on similar ellipses from the centre up to $2R_p$ (the Petrosian radius), spaced 2 pixel apart and having the width of 1 pixel. The brightness profile $I(R)$ is the azimuthally averaged value of the ellipses aforementioned; the error is the standard deviation of the same pixel set.

3.3 The Filters for $\tilde{\kappa}(R)$

Measuring the curvature, according to Eq. (1), would be just a matter of evaluating the first and second derivatives of the brightness profile. In practice, with discrete points for $I(R)$ contaminated by noise, the direct estimation of $d\nu/dR$ and $d^2\nu/dR^2$ are worthless because the noise in $I(R)$ is amplified by the derivative operator (a high pass filter). Fig. 1 shows this noise magnification that yield a very scattered curvature (blue points).

One way to overcome the limitations imposed by the noise is to use a filter to enhance the signal-to-noise of the data. Many linear filters attenuate the signal as well as the noise. For our purpose, we need a filter that attenuates the noise but keeps the overall structure present in the data. In general, the signal-to-noise ratio is higher in inner regions of the galaxy data and decreases to outermost regions. Therefore, the best solution to use in the filtering task is an adaptive filter, which takes into account the level of the dispersion and adapts the level of the smoothing accordingly.

We adopt a simple adaptive Gaussian filter G , which changes the Gaussian dispersion σ according to the local signal to noise ratio. We write a linear relation between σ and the radial distance R , assuming that inner regions are less noisy and constituted by small structures, and outer regions, more noisy and large structures, which is true for the majority of galaxies. We then write

$$\sigma(R) = (\sigma_{\max} - \sigma_{\min}) \frac{R}{2R_p} + \sigma_{\min} \quad (11)$$

where σ_{\min} is the standard deviation of the filter at the center of the data and σ_{\max} in the outermost region. Generally $\sigma_{\min} \lesssim 2$ and $\sigma_{\max} \sim 0.1 \times (2R_p)$. We performed tests with this design and verified that a single step of filtering in $\nu(R)$ is enough to remove effectively the noise from the data; to overcome edge effects caused by the filter when smoothing points at the edges, we discard the points corresponding to $2\sigma_{\min}$ at the beginning and $2\sigma_{\max}$ and the end of $\tilde{\kappa}$. – note that the green line of $\tilde{\kappa}(R)$ in Fig. 1 ends at $R/R_p \sim 1.7$.

4 DATA SAMPLE

The data in the present study is constituted by galaxies that already have been studied in terms of structural decompositions and multicomponent analysis. We have selected galaxies contained in the following works (Wozniak & Pierce 1991; Prieto et al. 2001; Cabrera-Lavers & Garzón 2004; Lauer et al. 2007; Gadotti et al. 2007; Gadotti 2008, 2009; Compère et al. 2014; Salo et al. 2015; Gao & Ho 2017; Yıldırım et al. 2017) (individual references bellow). The data were extracted according to their availability in NED and other databases. These are: EFIGI survey (Baillard et al. 2011), Hubble Space Telescope Archive (HLA¹), SPITZER Telescope (Dale et al. 2009), Pan-STARRS-1 telescope² (Chambers et al. 2016)

¹ Based on observations made with the NASA/ESA Hubble Space Telescope, and obtained from the Hubble Legacy Archive, which is a collaboration between the Space Telescope Science Institute (STScI/NASA), the Space Telescope European Coordinating Facility (ST-ECF/ESA) and the Canadian Astronomy Data Centre (CADC/NRC/CSA).

² The Pan-STARRS1 Surveys (PS1) and the PS1 public science archive have been made possible through contributions by the Institute for Astronomy, the University of Hawaii, the Pan-STARRS Project Office, the Max-Planck Society and its participating institutes, the Max Planck Institute for Astronomy, Heidelberg and the Max Planck Institute for Extraterrestrial Physics, Garching, The Johns Hopkins University, Durham University, the University of Edin-

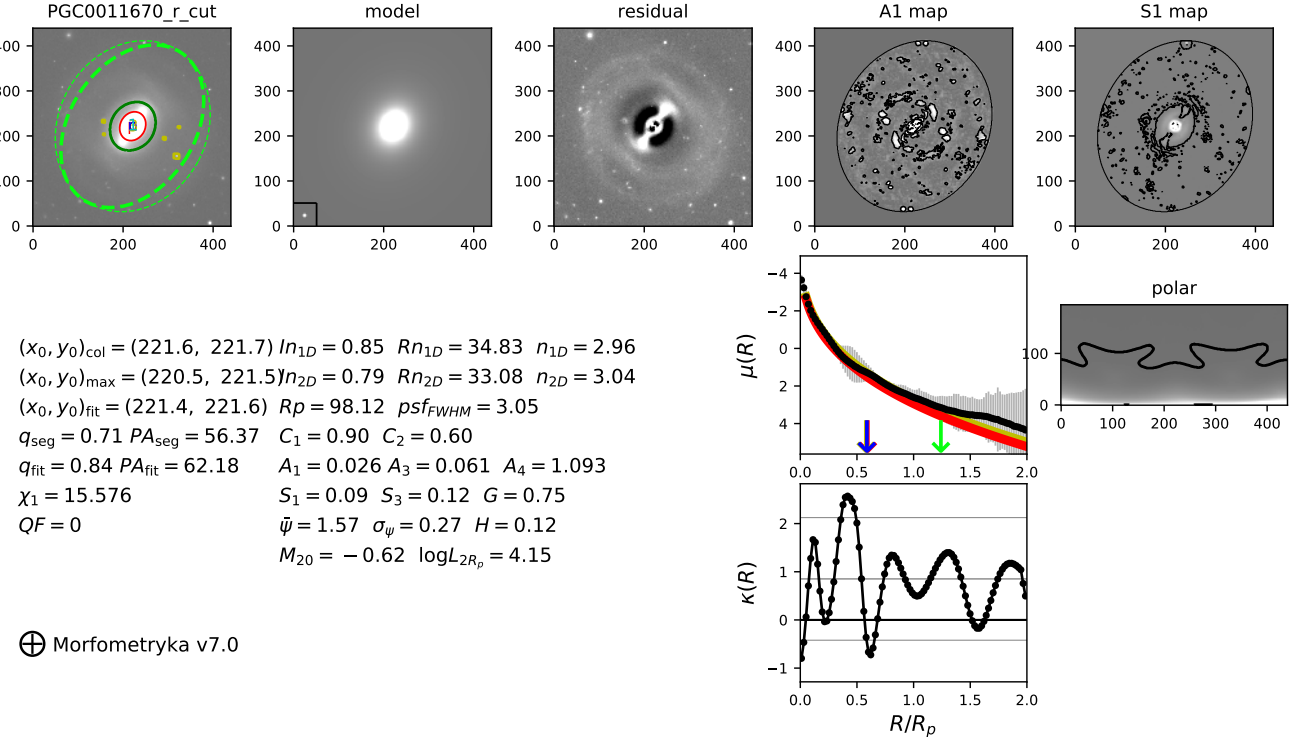


Figure 2. Output from MFMTK for the SDSS r image of NGC1211. The top panel shows (from left to right) the galaxy image, a single Sérsic fits model, residual image, and the asymmetry A_1 and smoothness S_1 maps. The numerical quantities are related to photometry and morphometry. The Sérsic parameters used to the model are the ones with the $2D$ index, performed in a two dimensional modelling (see Ferrari et al. 2015). The bottom right panel displays the surface brightness profile $\mu(R)$, the curvature $\tilde{\kappa}(R)$ and the polar plot used for σ_{ψ} .

and Cerro Tololo Inter-American Observatory 0.9m (CTIO0.9m) telescope³.

Tab. 1 introduces the following information for each galaxy: the complete references, where the data was taken, the filter used and the morphological classification found in the literature. Most of galaxies are in the r band, corresponding to a wavelength around 6250 angstroms. NGC 4251 is in the i band, with a wavelength around of 7760 angstroms. For the HST images we have the filter f160w, which corresponds to the H band with a wavelength peak of 1.545 microns⁴. For the Spitzer galaxies, the filter correspond to the IRAC3.6 band with a wavelength around of 3.6 microns. We have limited our study to a small set of 16 galaxies in order to lead a careful analysis with curvature. We selected galaxies in each general morphology: ellipticals, lenticular, disk/spiral (with and without bar).

The sample cover the following diversity:

inburgh, the Queen’s University Belfast, the Harvard-Smithsonian Center for Astrophysics, the Las Cumbres Observatory Global Telescope Network Incorporated, the National Central University of Taiwan, the Space Telescope Science Institute, the National Aeronautics and Space Administration under Grant No. NNX08AR22G issued through the Planetary Science Division of the NASA Science Mission Directorate, the National Science Foundation Grant No. AST-1238877, the University of Maryland, Eotvos Lorand University (ELTE), the Los Alamos National Laboratory, and the Gordon and Betty Moore Foundation. <https://outerspace.stsci.edu/display/PANSTARRS/Pan-STARRS1+data+archive+home+page>

³ <http://www.ctio.noao.edu/noao/>.

⁴ http://www.stsci.edu/hst/wfc3/ins_performance/ground/components/filters.

- (i) galaxies with complex structure, e.g. bars, rings, arms, disks, which are notably seem: NGC 1211 (Buta 2013), NGC 0936 (Wozniak & Pierce 1991), NGC 1512 (Laurikainen et al. 2006; Compère et al. 2014), NGC 7723 (Prieto et al. 2001);
- (ii) galaxies with fine structures, e.g. core, smooth bars or arms + S0 galaxies with smooth disks which barely can be identified: NGC 0384 (Yıldırım et al. 2017), NGC 1052 (Lauer et al. 2007), NGC 2767 (Nair & Abraham 2010; Yıldırım et al. 2017), NGC 4251 (Wozniak & Pierce 1991; Molaeinezhad et al. 2017), NGC 4267 (Wozniak & Pierce 1991), NGC 1357 (Li et al. 2011; Gao & Ho 2017), NGC 2273 (Cabrera-Lavers & Garzón 2004), NGC 6056 (Tarenghi et al. 1994; Prieto et al. 2001);
- (iii) galaxies with well known structure in shape, for example ellipticals: NGC 472, NGC 1270 (Yıldırım et al. 2017);

With this set we investigate the behaviour of $\tilde{\kappa}(R)$ for each representative morphology, recognizing how the curvature differs between each type.

5 APPLICATIONS TO THE DATA SAMPLE

Now we will study the behaviour of $\tilde{\kappa}(R)$ for galaxies presented in Tab. 1 with the aim to distinguish galaxy multicomponents and decipher different morphologies. Each galaxy in our sample will be discussed individually in separated sections, divided by their global morphologies, e.g. lenticulars (Section 5.3), spirals (Section 5.4) and ellipticals/spheroidal components (Section 5.5). We begin by discussing $\tilde{\kappa}$ for two cases in detail: NGC 1211 and NGC 1357. The

Table 1. Data sample used in this work.

<i>i</i>	Galaxy Name + filter	Morphology	Origin	Reference of the data
1	NGC0384-f160w	S0 ³ /E ^{1,2}	HST	(Yıldırım et al. 2017)
2	NGC0472-f160w	VY CMPT ²	HST	(Yıldırım et al. 2017)
3	NGC0936- <i>r</i>	SB0 ⁴	EFIGI	(Baillard et al. 2011)
4	NGC1052- <i>r</i>	E ^{1,5} (+core ⁶)/S0 ⁵	EFIGI	(Baillard et al. 2011)
5	NGC1211- <i>r</i>	SB0/a(r) ⁷	EFIGI	(Baillard et al. 2011)
6	NGC1270-f160w	E ¹ /VY CMPT ²	HST	(Yıldırım et al. 2017)
7	NGC1357-3.6μm	SA(s)ab ¹	SPITZER	(Dale et al. 2009; Sheth et al. 2010)
8	NGC1512- <i>r</i>	SB(r)a ¹	CTIO	(Meurer et al. 2006)
9	NGC2273- <i>r</i>	SB(r)a ¹	Pan-STARRS	(Chambers et al. 2016)
10	NGC2767- <i>r</i>	E ¹ /S0 ⁸	HST	(Yıldırım et al. 2017)
11	NGC4251- <i>i</i>	SB0 ⁴	SDSS	(Alam et al. 2015)
12	NGC4267- <i>r</i>	S0 ³ /SB0 ^{4,5}	EFIGI	(Baillard et al. 2011)
13	NGC4417- <i>r</i>	SA0a ⁹	EFIGI	(Baillard et al. 2011)
14	NGC4452- <i>r</i>	SB(l)0c ⁹	EFIGI	(Baillard et al. 2011)
15	NGC6056- <i>r</i>	SB(s)0 ^{1,10} /S0/a ¹¹	EFIGI	(Baillard et al. 2011)
16	NGC7723-3.6μm	SB(r)b ^{1,10}	SPITZER	(Dale et al. 2009; Sheth et al. 2010)

¹ (de Vaucouleurs et al. 1991).² (Yıldırım et al. 2017).³ (Nilson 1973).⁴ (Wozniak & Pierce 1991).⁵ (Sandage & Tammann 1981).⁶ (Lauer et al. 2007).⁷ (Gadotti et al. 2007).⁸ (Nair & Abraham 2010).⁹ (Kormendy & Bender 2012).¹⁰ (Prieto et al. 2001).¹¹ (Tarenghi et al. 1994).

full data sample is discussed below. The complete set of figures for the curvature are given in the Appendix A.

For each galaxy (see the model reference Fig. 3), we present the broad band image of the galaxy in the top left panel. In the middle panel we show the residual map from a single Sérsic fit to the broad band image made with MORFOMETRYKA – for the structures are easily visualized on it. For both, yellow dotted lines correspond to regions identified in the curvature plot and yellow dot-dashed line mark the $2R_p$ region. The bottom panel shows the normalized brightness profile $v(R)$ (red curve – scale in the axis at right) and curvature $\tilde{\kappa}(R)$ calculated from it (green curve – scale on axis at left). The solid vertical lines delimitate regions of different components (discussed below for each galaxies); they correspond to the yellow ellipses in the images, but are inferred from the $\tilde{\kappa}$ behaviour. Vertical dashed line is the limit of confidence of SNR = 2.

5.1 Case Study 1: Curvature of NGC 1211

We begin by analysing the $\tilde{\kappa}$ and components for galaxy NGC 1211 (PGC 11670) of the EFIGI sample. NGC 1211 is classified as (R)SB(r)0/a (de Vaucouleurs et al. 1991), i.e. barred spiral/lenticular with rings. In Fig. 3 it is shown the SDSS galaxy *r* image (top), the residual from a single Sérsic fit by MORFOMETRYKA (middle) and the curvature $\tilde{\kappa}$ on the bottom. The behaviour of $\tilde{\kappa}$ is related to the transition between regions dominated by different components. In the galaxy image on the top panel, the size of the yellow dotted lines overlaid were determined by the local peaks in the curvature plot (bottom), signalled as vertical solid lines. They delimitate the regions (identified by the labels) that are dominated by different components.

Starting from the central region, we have two local peaks in $\tilde{\kappa}$

at $R/R_p \sim 0.1$ and $R/R_p \sim 0.3$. The region inside the first (label 1) seems to be a small structure inside the bulge which is represented by region 2. However, both components have small values in curvature compared to the maximum amplitude (at $R/R_p \sim 0.4$), the bulge in region 2 reaches values close to zero, therefore this indicates that the Sérsic index of this component is close to 1 (this can also be seen by the straight brightness profile in the region – red curve in bottom plot). This may indicate that the bulge of NGC 1211 is a pseudobulge. Note also that the component in the innermost region also has a small $\tilde{\kappa}$. In Méndez-Abreu et al. (2018) they comment that NGC 1211 has an internal structure called “barlenses”, which is a component different of a bulge contained inside the bar (Laurikainen et al. 2010). Gadotti et al. (2007) also observed a nuclear structure in this galaxy. Therefore, the signature in $\tilde{\kappa}$ in regions 1 and 2 are not of a classical bulge, but indicate the presence of the nucleus and a pseudobulge.

The second peak at $R/R_p \sim 0.3$ is the transition between the bulge with the bar+inner ring – a narrow and negative valley in $\tilde{\kappa}$. Usually Bars and inner rings are associated with narrow valleys in $\tilde{\kappa}$. For inner rings they are negative and for bars they can be negative or not, however in general both have narrow valleys.

The third peak at $R/R_p \sim 0.75$ defines the end of the bar and the start of the outer region of the galaxy, label 4 and 5. The transition 4 → 5 is indicated by the local peak at $R/R_p \sim 1.2$. The intermediate regions of 4 shows $\tilde{\kappa} \sim 0$ regarding a disk like structure. As indicated by Buta (2013), NGC 1211 has two outer rings, the inner outer is red and the outer outer blue (see his Figure 2.30).

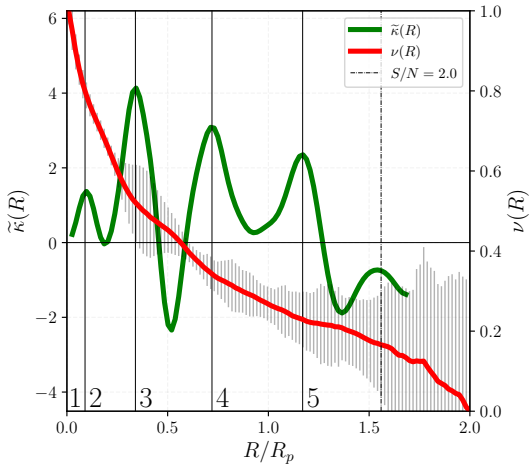
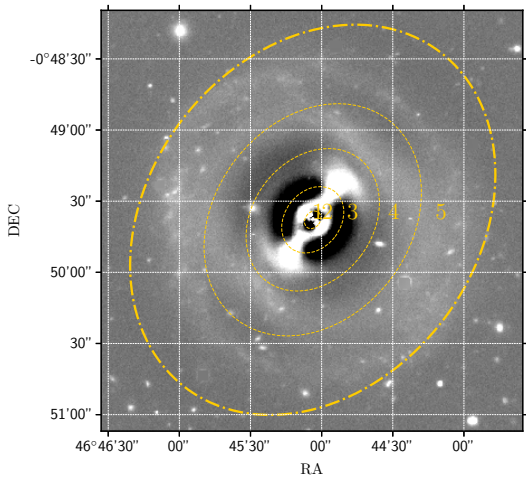
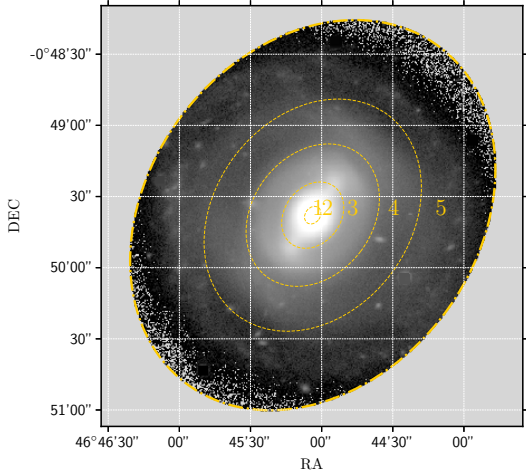


Figure 3. **Top:** SDSS r image for NGC1211 from the EFIGI sample. The yellow lines represent each component of the galaxy. These regions were drawn from the local peaks in the green line of $\tilde{\kappa}(R)$ (see bellow). The numbers in the yellow ellipses and in the $\tilde{\kappa}$ plots refer to the same regions. **Middle:** Residual from a single Sérsic fit to the image above made with MORFOMETRYKA. For both, yellow dotted lines correspond to regions identified in the curvature plot below; yellow dot-dashed line is the $2R_p$ region. **Bottom:** Normalized log-brightness profile (red curve) and curvature $\tilde{\kappa}$ calculated from it (green curve). The solid vertical lines delimit regions of different components (see text for details). The vertical dashed line is the limit of confidence of SNR=2.

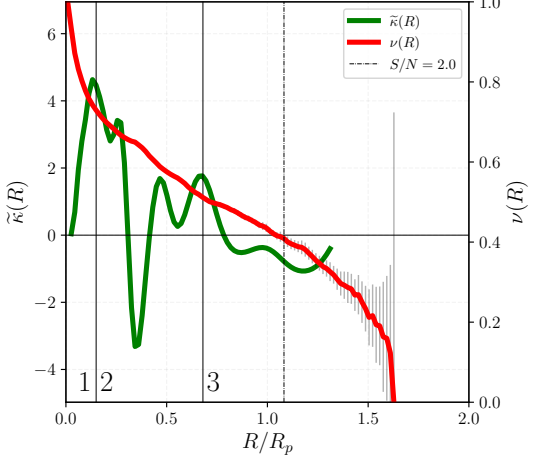
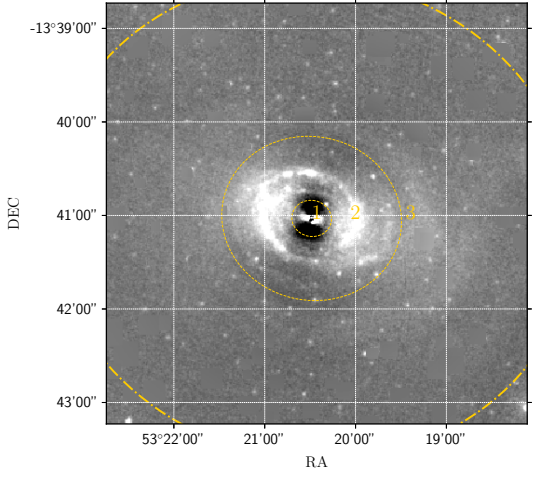
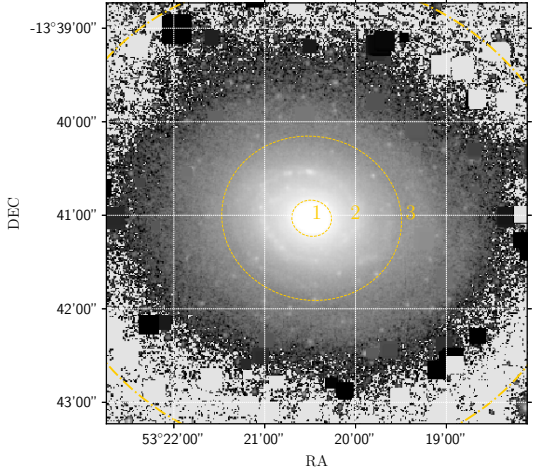


Figure 4. Near infrared band ($3.6\mu\text{m}$) of NGC 1357 from Spitzer telescope. Labels and graphic positions are the same as Fig. 3, and the same for the remaining figures. Region 1 is the bulge (high and large peak in $\tilde{\kappa}$). Region 2 is the disk with spiral arms and the outer disk is region 3 with low values in curvature. Again, the dashed vertical line (SNR=2) is our limit of confidence. See the text for further details of this galaxy.

5.2 Case Study 2: Curvature of NGC 1357

NGC 1357 is a non-barred spiral galaxy classified as SA(s)ab (de Vaucouleurs et al. 1991). Gao & Ho (2017) considered that the galaxy have two disks: an inner blue disk which contains well defined spiral arms, and an outer red disk with no spiral arms. Fig. 4 shows the curvature for NGC 1357.

The bulge is indicated by the region of high curvature (1); the valley at (2) is related to the tight shape of the spiral arms, having a ring-like shape. The valley in $\tilde{\kappa}$ is an evidence of the ring structure, pointed out by Li et al. (2011); Gao & Ho (2017). We found that a high and narrow negative gradient in curvature is characteristic of ring and bar components – which corresponds to Sérsic index lower than unity. The transition of this ring with the spiral structure corresponds to the middle inwards part of region 2. However, all spiral structure is contained inside region 2 which is the inner disk.

The transition between the inner and the outer disk is underpinned by the decrease in the oscillations after the local peak at $R/R_p \sim 0.65$, therefore region 3 corresponds to the outer disk with no spiral arms. As mentioned before, a disk has values of $\tilde{\kappa}$ close to zero. In following Section, we extend the same analysis for the rest of the sample, separating them according to each morphological type. The remaining the figures are in Appendix B.

5.3 Lenticular Galaxies

NGC 936

NGC936 is classified as barred lenticular galaxy SB0 (Wozniak & Pierce 1991), formed by a structure of bulge+bar+disk. In Fig. B1 we infer from $\tilde{\kappa}$ that the bulge dominates region 1, while the bar becomes dominant in region 2 – indicated by the strait valley and negative $\tilde{\kappa}$. It ends close to $R/R_p \sim 0.5$. Bar properties were also extracted by Muñoz-Mateos et al. (2013), regarding the bar length. The peak in $\tilde{\kappa}$ at $R/R_p \sim 0.5$ indicating the end of the bar seems to be in agreement with the outer limit found by the authors (see their figure 3). The bar of NGC 936 was also studied by Erwin & Sparke (2003) together with a nuclear ring inside the bar region. Returning back to the inner component, $\tilde{\kappa}$ is nearly constant and ~ 1 . This suggest that the inner region is not a classical bulge, rather being a pseudobulge, which also contains a nuclear ring.

In region 3 (around $R/R_p \sim 0.8$) we see a broad and smooth valley of negative curvature, and subsequently being close to zero for $R/R_p > 1.0$ – this pattern appears because the disk is of type II (Erwin et al. 2008; Muñoz-Mateos et al. 2013) which explains the broad valley. It is possible to discriminate a valley in $\tilde{\kappa}$ entailed by the disk of Type II morphology and one related to a ring or a bar. Valleys for bars and rings have high negative gradient in $\tilde{\kappa}$ and are thin in width (see additional examples in FIGURES 3, 4, B1, B2, B6, B7, B8 and B9).

NGC 2767

NGC 2767 is classified as an elliptical (de Vaucouleurs et al. 1991) and as an S0 (Nair & Abraham 2010). However, the structure of this galaxy is not trivial to be resolved. Yıldırım et al. (2017) comment that the PA twist in the centre of the galaxy may imply the existence of a bar and a dust disk. Examining $\tilde{\kappa}$ in Fig. B2 shows the existence of two peaks and a narrow deep valley, revealing that the galaxy has at least three components (regions 1, 2 and 3). The bulged central part is demarcated by 1. The valley in 2 ($R/R_p \sim 0.4$), even not being negative (but ~ 0), is much smaller than the neighbouring

peaks in terms of amplitude, therefore pointing to a bar component. The region 3 seems to be of a disk structure of type II, very similar to NGC 936 (note that after $R/R_p \sim 1.0$, the curvature almost vanishes). A final note is that, photometrically, the bulge of this galaxy is indicated to be pseudobulge due to the behaviour of $\tilde{\kappa}$ in the inner part of the profile – it takes some distance from the centre to increase significantly until the transition region at $R/R_p \sim 0.4$. Summarizing, in agreement with Yıldırım et al. (2017), the curvature entail that the galaxy may have a bulge+bar+disk structure. The residual image in the middle panel of Fig. B2 demonstrates these structures well within the delimited regions gathered from the curvature in bottom plot.

NGC 4267

In earlier catalogues (Nilson 1973) NGC 4267 was classified as S0. In Sandage & Tammann (1981) and more recent works (Wozniak & Pierce 1991; Jungwiert et al. 1997; Gadotti & de Souza 2006; Erwin et al. 2008) it is suggested the presence of a bar. The shape of $\tilde{\kappa}(R)$ is shown in Fig. B3. In comparison to NGC 2767, NGC 4267 exhibit an akin radial profile, however $\tilde{\kappa}$ is considerably different. Region 1 around $R/R_p \sim 0.3$ refers to the bulge while the disk takes part in the remaining of the profile in region 2 (lower $\tilde{\kappa}$ below zero). In respect to the bar, the curvature does not trace a sign of it because the pattern of a narrow valley is not exhibited. Also combining together the curvature and the residual image (middle panel of Fig. B3), shows no evidence of a photometric bar component. In relation the bulge and the disk, the transition of both is highlighted by the peak in $\tilde{\kappa}$ at $R/R_p \sim 0.3$. The inner region shows an abrupt increasing of $\tilde{\kappa}$ from zero to the transition region with the disk, therefore this points that the bulge is a classical bulge. This is in agreement with Fisher & Drory (2010) (see their Table 2).

NGC 4251

NGC 4251 is classified as S0 (Nilson 1973; Sandage & Tammann 1981) and SB0 (de Vaucouleurs et al. 1991), but the confirmation of a bar component is not direct. Wozniak & Pierce (1991) performed a multicomponent analysis and reaffirmed its existence, having oval shape similar to the bulge. Molaeinezhad et al. (2017) indicates the presence of a bar based on the kinematics of the galaxy. Fisher (1997) noted that there is no bar in this system. The bar pattern for $\tilde{\kappa}$ does not appear in Fig. B4, still we delimitate the galaxy in regions. Region 1 and 2 (the part of the bulge) shows that the inner structure has a spheroidal shape. Analysing the residual image, great part of region 3 is supposed to be the bar, while 4 is the disk, since $\tilde{\kappa}$ decrease – do not account for $R/R_p > 1.5$, where $\tilde{\kappa}$ increases again, because of the filter. For this galaxy the limit $S/N \sim 2$ is externally to the cutted profile. Also, the pattern for bars found in other galaxies is not present in NGC4251.

NGC 4417

NGC4417 is classified as SB0:edge-on (de Vaucouleurs et al. 1991; Hinz et al. 2003) and also S0:edge-on (Sandage & Tammann 1981; Nilson 1973). In the curvature plot of Fig. B5, two peaks stand out in the first half of the R_p region: 1 and 2 seems to have a bulge morphology, while 3 is a disk. Analysing $\tilde{\kappa}$, it seems plausible that it distinguish two components inside $R/R_p \sim 1.0$, the first part identified by the first peak and the second by the second peak. Both components have small $\tilde{\kappa}$ (the values in the intermediary region are

lower than the transitions). Kormendy & Bender (2012) argued that the inner part is an inner disk and 2 is the bulge⁵ with a boxy shape due to a faint bar. This seems reasonable to confirm here because the behaviour in $\tilde{\kappa}$ resembles a bar, as we are arguing here. However, in this case we could not differentiate the bulge from the bar. In the residual image it is clear that there are signs of two components, in 1 a more oval shape while in 2 a boxy one. A final comment is related to the peak in $\tilde{\kappa}$ close to $R/R_p \sim 1.5$. Due to the signal-to-noise limit and considering that this region is close to the edge of the galaxy, we do not treat it as a transition of components.

NGC4452

NGC 4452 is an edge-on SB0(l) galaxy having a small pseudobulge (Kormendy & Bender 2012). In the curvature plot of Fig. B6 is seen a small component at the centre ($R/R_p \lesssim 0.15$). Since the first component has a small $\tilde{\kappa}$ and does not increase immediately, it is confirmed a pseudobulge component, however not being well pronounced due to the few data points. From that point to $R/R_p \sim 0.5$ the value of $\tilde{\kappa}$ reaches negative values and has the bar pattern, as exposed by Kormendy & Bender (2012). The bar extension goes to $R/R_p \sim 0.53$, marking the transition between the bar and the lens (Kormendy & Bender 2012). The third smooth peak at $R/R_p \sim 1.1$ indicates the emergence of an outer disk with low positive value in curvature.

5.4 Spirals

NGC1512

NGC 1512 is classified as a barred spiral galaxy SBa (de Vaucouleurs et al. 1991), however there are many references bringing up other components in its morphology: rings, pseudorings, nuclear ring and pseudobulge, see for example (Laurikainen et al. 2006; Fisher & Drory 2008). According to Compère et al. (2014), who conducted a deep study on this galaxy, it has a bulge, a bar and a disk.

Fig. B7 shows the results for $\tilde{\kappa}$. The region inside $R/R_p < 0.5$ shows two components delimited by the local peak at $R/R_p \sim 0.15$, and both shows small $\tilde{\kappa}$ compared with the overall curvature profile, therefore one must consider a pseudobulge component. From Laurikainen et al. (2006); Compère et al. (2014), the innermost region (1) is a nuclear ring. Region 2 is dominated by the bulge. If fact, by the shape of $\tilde{\kappa}$ it is a pseudobulge, which is in agreement with Fisher et al. (2009); Fisher & Drory (2010).

Regarding the bar, it seems that pseudobulge and bar coexist (the change in the position angle and ellipticity between the bulge and the bar is very smooth, see figure 4 of Jungwiert et al. (1997)), with the bar connecting the pseudobulge and the outer ring – according to Fisher & Drory (2008), a pseudoring (region 3). This does not allow $\tilde{\kappa}$ to distinguish the bar from the pseudobulge – in region 2 there is not a significant narrow valley to indicate it. Fisher & Drory (2008) also did not fit a bar component separately to NGC 1512 and considered only a Sérsic+Exp fit to it.

What is noticeably is the outer ring, the peak at $R/R_p \sim 0.5$ points to the transition between the pseudobulge+bar with this ring, which is dominant in region 3. The last smooth peak at $R/R_p \sim$

⁵ Kormendy & Bender (2012) found a prominent bulge ($B/T \sim 0.88$) to this galaxy.

1.1 bound the dominance of the outer ring with a faint disk ($\tilde{\kappa}$ approaches to zero).

NGC 2273

NGC 2273 is classified as SBa (Nilson 1973) and SB(r)a (de Vaucouleurs et al. 1991). In Fig. B8 the curvature indicates a small bulge contained inside $R/R_p \sim 0.1$ (region 1). Considering the valley in region 2, it retains a significant gradient in $\tilde{\kappa}$ in comparison to the first and second peaks, this suggests a bar component. The next valley in region 3 is formed by two tightly wound spiral arms Laurikainen & Salo (2017), which behaves like a ring. The fourth peak at $R/R_p \sim 0.5$ makes the transition of this ring with the outermost region of the galaxy.

Cabrera-Lavers & Garzón (2004) worked on in details considering the previous structures, adding a lens component and assuming that the outer region is a disk. Also, they argue that the bulge is prominent, nevertheless $\tilde{\kappa}$ advises that the bulge is not too prominent. Erwin & Sparke (2003) says that this galaxy is four-ringed, two of them outer rings (outer region). The curvature give a picture of these rings in regions 4. The evidence that the bulge is not to prominent can be explained by the fact that the inner region can be formed by other components: Moiseev et al. (2004) noted that the bar is of large scale; Erwin & Sparke (2003); Moiseev et al. (2004) also assert that the innermost region can be built by a nuclear spiral while Mulchaey et al. (1997) says that it is a secondary bar. Therefore, an acceptable constraint that $\tilde{\kappa}$ gives for NGC 2273 is a bulge+bar+ring/disk structure.

NGC 7723

NGC 7723 is classified as SB(r)b/SB(rs) (de Vaucouleurs et al. 1991; Comerón 2013). Fig. B9 shows the result of the curvature for NGC 7723. The bulge is contained inside the region 1 delimited by $R/R_p \sim 0.1$. Eskridge et al. (2002) says that the central part of this galaxy is composed by a boxy bulge with a symmetric nucleus embedded in. As indicated by $\tilde{\kappa}$, it has a pseudobulge – note that $\tilde{\kappa}$ does not increase continuously and fast, it took up to $R/R_p \sim 0.2$ to grow abruptly until the transition region at the peak. This hint of a pseudobulge is in agreement with Prieto et al. (2001) (they found an unitary Sérsic index in r -band).

Analysing the valley in region 2 together with the residual image we see that it is related to a bar and a ring. However, the bar is much more prominent (Prieto et al. 2001) than the later and it becomes non-trivial to demonstrate the existence of a ring. In fact, this component is considered to be a pseudoring formed by the way the spiral arms emerges from the bar (del Rio & Cepa 1998; del Río & Cepa 1999; Prieto et al. 2001; Eskridge et al. 2002). In Aguerri et al. (2000); Prieto et al. (2001) they mentioned the ring structure but in their structural decomposition they have not taken it into account. The spiral arms begin at $R/R_p \sim 0.35$ – observe the oscillations in $\tilde{\kappa}$. del Rio & Cepa (1998) made another commentary arguing that there is a disk outside the spiral arms, which is seen in $\tilde{\kappa}$ after $R/R_p \sim 1.0$ because $\tilde{\kappa} \sim 0$.

NGC 6056

This galaxy is considered to be an barred spiral with an internal bulge (SB(s)0) (de Vaucouleurs et al. 1991; Prieto et al. 2001), and also non-barred (S0/a) (Tarenghi et al. 1994). In $\tilde{\kappa}$ of Fig. B10, the bulge is within $R/R_p \lesssim 0.18$ (first peak). The valley in 2 is the bar

(the same behaviour in $\tilde{\kappa}$ as the other galaxies), and confirmed by [Prieto et al. \(2001\)](#). The transition of the bar with the outer disk (spiral) is the local peak at $R/R_p \sim 0.6$.

A pseudobulge component was pointed by [Prieto et al. \(2001\)](#) and they found a Sérsic fit of $n = 1.1$ in the r band. This is the only galaxy in our sample (but quite similar to NGC 4452) that the pseudobulge part does not show the same behaviour in $\tilde{\kappa}(R)$ as the other galaxies. We may attribute this to the low resolution of the galaxy image – note that there are few data points in the region pertaining to the bulge.

5.5 Spheroidal components

Unlike spiral and lenticular galaxies, whose components are structurally very diverse (bulge, bar, spiral arms and disk, for example), in the case of spheroidal galaxies (the various kind of ellipticals, bulges and some lenticular) the differences in the components are much more subtle. Consider, for instance, that many elliptical galaxies substructures cannot be seen in raw images, but rather, reveal themselves after image manipulation techniques, such as unsharp masking, brightness profile modelling and so on. In this way, we may regard that the effects that the different component of elliptical galaxies have on the curvature are more faint than for spiral galaxies.

NGC 1270

NGC 1270 is classified as an elliptical galaxy ([de Vaucouleurs et al. 1991](#)) and further as a compact elliptical galaxy ([Yıldırım et al. 2017](#)). The curvature $\tilde{\kappa}(R)$ is displayed in Fig. B11, its shape is not continuous (as expected) and having small oscillations of low scale. However, the curvature has a smooth overall shape, is high in inner regions (around $R/R_p \sim 0.2$) and drops to near zero at large radius. As can be seen in the residual image, the central region ($R/R_p \lesssim 0.25$) indicates an inner spheroidal component with different properties compared to the main body of the galaxy (missing light regarding the model for the main body). There is a sign of a small disk within $R/R_p \lesssim 0.1$ aligned with the apparent main axis of the galaxy.

NGC 472

NGC 472 is a compact elliptical galaxy ([Yıldırım et al. 2017](#)). Similar to NGC 1270, it does show some perturbations in the inner regions – the two local peaks are attributed to inhomogeneities – but the shape of $\tilde{\kappa}$ follows an overall shape resembling a pure component, which is smooth and increases in the inner region and decreases for the outermost part. A single Sérsic fit of $n = 5.8$ returned a robust representative model, since there is no residual structures in the outer regions.

NGC 384

NGC 384 is classified in literature as E ([de Vaucouleurs et al. 1991; Yıldırım et al. 2017](#)) but also S0 ([Nilson 1973](#)). In comparison to NGC 472 and NGC 1270, $\tilde{\kappa}(R)$ is quite different (Fig. B13) due to the emergence of the substantial oscillations in the region $R/R_p \lesssim 0.5$. These delineates some internal and small structure. In the residual image of Fig. B13 it is readily seen such structure with a disk oval shape.

NGC 1052

NGC1052 is classified as an elliptical galaxy ([de Vaucouleurs et al. 1991](#)) and as E/S0 ([Sandage & Tammann 1981](#)). [Lauer et al. \(2007\)](#) indicates the presence of a core. In Fig. B14 the curvature suggests some possibly transition around $R/R_p \sim 0.15$, in which, therefore, might be between the core structure and the remaining structure of an elliptical. [Milone et al. \(2007\)](#) (and references therein) conclude that NGC 1052 has a rotating disk. The curvature seems to indicate such kind of component because it has small values around $R/R_p \sim 0.75$, this is also seen in the residual image.

6 DISCUSSION

Galaxy structural analysis has been traditionally tackled with parametric methods of model fitting. Currently, given the amount of data available, there is a growing need of using non-parametric methods that do not have an underlying model and that require less user intervention. The curvature, being non-parametrical, provide us with a framework that allow us to automate the galaxy structural analysis and thus its appliance to large datasets..

With our set of 16 galaxies, distinct behaviours appeared concerning the curvature. The basics is that regions dominated by different structural components have its own shape in the surface brightness and we can use $\tilde{\kappa}$ to unveil the difference between each one. The curvature is sensitive to smooth (e.g NGC 384, NGC 6056) or abrupt variations (e.g. NGC 1512, NGC 7723) of the light profile. High concentrated regions have high values of $\tilde{\kappa}$, but transitions between high to low concentrated also reveal high $\tilde{\kappa}$ or (in some cases) even higher than a high concentrated component itself. This happen because along the radius, a transition is a smooth discontinuity of the inner part, which gives rise to the next component – i.e. the point where the profile changes from one component to another – frequently has a different slope (higher) than the slope characteristic of each profile alone. Below we discuss the signature of each component in the curvature profile related to the individual galaxies.

Bars

Bars and rings show a depression pattern in $\tilde{\kappa}$ where these components dominate. For NGC 936 and NGC 2767 (Fig. B1 and Fig. B2 respectively) the bars have a distinct valley between the two local peaks 1 → 2 and 2 → 3, respectively. These bars are represented by the narrow valleys in $\tilde{\kappa}$ (note the difference between a narrow valley in $\tilde{\kappa}$ related to a bar and a broad valley related to a disk type II in region 3 of NCG 936). For the faint bar of NGC 2273 (Fig. B8), the curvature exhibit a deep but non non-negative valley in region 2 (between the two local peaks). We found that the depression in $\tilde{\kappa}$ for bars is not always negative, but considerably lower than the local peaks. Galaxies NGC 1512 (Fig. B7) and NGC 4251 (Fig. B4) does not have a clear indication of a bar in (region 2 and 3, respectively). Despite this, considering that the bar exists in fact – according to the literature – for both galaxies, bulge and bar appear to show a subtle transition.

Rings

Galaxies NGC 1512 (Fig. B7), NGC 2273 (Fig. B8) and NGC 7723 (Fig. B9) have rings. They exhibit a high and narrow negative gradient in region 3(first two) and region 2 (last one). These ring

structures are also likely to be formed by the tight morphology of the spiral arms after the end of the bar. Between rings and bars, the rings showed more pronounced narrow valleys in $\tilde{\kappa}$.

Disks and spiral arms

The most notable galactic disk absent of spiral arms that shows values of $\tilde{\kappa}$ close to zero is that of NGC 4267 (Fig. B3). For NGC 936 (Fig. B1) the disk is of Type II, therefore it shows a valley in region 3, but the outer part approaches zero. A similar result is found for NGC 2767 (Fig. B2). Another case is NGC 4417 (Fig. B5) which in region 3 shows a decreasing $\tilde{\kappa}$ and reach small values, regarding that not all galaxy disks follows a $n = 1$ Sérsic law, therefore there are disk components that exhibit $\tilde{\kappa} > 0$ or $\tilde{\kappa} < 0$.

NGC 1357 (Fig. 4), NGC 2273 (Fig. B8), NGC 7723 (Fig. B9) and NGC 6056 (Fig. B10) have spiral arms. For NGC 7723 the spirals arm are well identified by $\tilde{\kappa}$ at the inner to middle part of region 3, due to the homogeneous oscillations. Galaxy NGC 1357 also shows two oscillations of this kind from the middle onwards part of region 3. For NGC 2273, the pattern in $\tilde{\kappa}$ is not well defined, but we still get an indication of a perturbed disk in region 4. The spiral galaxy in which the spiral structure does not appear clearly is NGC 6056.

Spheroidal

For our elliptical galaxies the curvature behaviour also revealed interesting results. For NGC 384 (Fig. B13) $\tilde{\kappa}$ revealed an inner component due to the in the region $R/R_p < 0.5$, which is a inner dust disk. For NGC 472 (Fig. B12), NGC 1052 (Fig. B14) and NGC 1270 (Fig. B11) $\tilde{\kappa}$ also indicates perturbations of $I(R)$. This behaviour indicates that these galaxies are not a complete homogeneous system but are formed by heterogeneous light distribution. This means that even in systems with subtle variations of the brightness profile, we can unveil the existence of perturbations in the galaxy's structure.

Pseudobulges

Another important result we found on this work is the behaviour of $\tilde{\kappa}$ for pseudobulges. Inner regions that shows small values of curvature compared to the values of posterior regions might infer pseudobulge components. In our sample the cases are NGC 1211 (Fig. 3), NGC 936 (Fig. B1), NGC 2767 (Fig. B2), NGC 1512 (Fig. B7), NGC 2273 (Fig. B8) and NGC 7723 (Fig. B9). For NGC 2273 this pattern is not too clear. For NGC 2767 there is no reference in literature indicating that the bulge is pseudo – here we point that it is.

In summary, in pseudobulges the curvatures displayed a distinct pattern. Since pseudobulges are more similar to disks, having nearly-exponential surface brightness profiles (Laurikainen et al. 2016), the curvature might in general shows a behaviour that resembles a disk, we mean this by having small values in inner regions and no abrupt variations (fast increasing) in some range of R .

7 SUMMARY

We summarise bellow our conclusions in using the curvature of the brightness profile for structural analysis. We have introduced the curvature of the brightness profile of galaxies as a tool to identify and study their different structural components, most notably

bulges, bars, discs, rings and spiral arms. The underlying argument for such is that these components have distinct Sérsic index (or concentration) which directly impact the curvature. But, unlike standard multicomponent modelling of light profiles, the curvature is non parametric and does not depend on model parameters.

We measured the curvature profile for structural analysis to 16 galaxies (Tab. 1) comprising different morphologies. For these galaxies, we identified their structural components and inferred their domain regions in terms of the local peaks in $\tilde{\kappa}(R)$; Following the peaks in the measured curvature profile we spotted the matching regions in the image and residual maps where the different components can be identified and related to the curvature behaviour. Thus regarding the curvature curve (in terms of logarithm normalized scale of intensity): (i) Disks have a broad profile in the curvature with near zero (Type I) or negative (Type II) values. (ii) Bars and rings have narrow negative valleys in $\tilde{\kappa}$ (more pronounced for rings); (iii) pseudobulges have small values (compared to the highest absolute values) or near zero curvature in their regions; (iv) the curvature in elliptical galaxies shows that they are not completely homogeneous system.

ACKNOWLEDGMENTS

We would like to thank Horácio Dottori and Leonardo de Albernaz Ferreira for useful comments in the original manuscript. Valérie de Lapparent for kindly providing the original high resolution EFIGI stamps used in this work. The Programa de Pós Graduação em Física of Universidade Federal do Rio Grande for all the infrastructure and PROPESP-FURG for part of financial support. We also thank Coordenação de Aperfeiçoamento de Pessoal de Nível Superior - Brasil (CAPES) for the research grant funding, supporting the development of this work.

References

- Abazajian K., et al., 2003, *The Astronomical Journal*, **126**, 2081
- Aguerri J. A. L., Varela A. M., Prieto M., Muñoz- Tuñón C., 2000, *The Astronomical Journal*, **119**, 1638
- Alam S., et al., 2015, *The Astrophysical Journal Supplement Series*, **219**, 12
- Andrae R., Jahnke K., Melchior P., 2011, *Monthly Notices of the Royal Astronomical Society*, **411**, 385
- Argyle J. J., Méndez-Abreu J., Wild V., Mortlock D. J., 2018, preprint, ([arXiv:1807.02097](https://arxiv.org/abs/1807.02097))
- Ascasibar Y., Gottlöber S., 2008, *Monthly Notices of the Royal Astronomical Society*, **386**, 2022
- Athanassoula E., 2005, *Monthly Notices of the Royal Astronomical Society*, **358**, 1477
- Baillard A., et al., 2011, *A&A*, **532**, A74
- Bershady M. A., Jangren A., Conselice C. J., 2000, *The Astronomical Journal*, **119**, 2645
- Blanton M. R., et al., 2001, *The Astronomical Journal*, **121**, 2358
- Bruce V. A., et al., 2014, *Monthly Notices of the Royal Astronomical Society*, **444**, 1660
- Burkert A., Naab T., 2003, Major Mergers and the Origin of Elliptical Galaxies. Springer Berlin Heidelberg, Berlin, Heidelberg, pp 327–339, doi:[10.1007/978-3-540-45040-5_27](https://doi.org/10.1007/978-3-540-45040-5_27), https://doi.org/10.1007/978-3-540-45040-5_27
- Buta R. J., 2013, Galaxy Morphology. p. 155
- Cabrera-Lavers A., Garzón F., 2004, *The Astronomical Journal*, **127**, 1386
- Caon N., Capaccioli M., D'Onofrio M., 1993, *Monthly Notices of the Royal Astronomical Society*, **265**, 1013
- Chambers K. C., et al., 2016, arXiv e-prints, p. [arXiv:1612.05560](https://arxiv.org/abs/1612.05560)
- Ciotti L., Bertin G., 1999, *Astronomy and Astrophysics*, **352**, 447

- Comerón S., 2013, *Astronomy & Astrophysics*, **555**, L4
- Compère P., López-Corredoira M., Garzón F., 2014, *Astronomy & Astrophysics*, **571**, A98
- Crane K., de Goes F., Desbrun M., Schröder P., 2013, in ACM SIGGRAPH 2013 Courses. SIGGRAPH '13. ACM, New York, NY, USA, pp 7:1–7:126, doi:10.1145/2504435.2504442, <http://doi.acm.org/10.1145/2504435.2504442>
- Dale D. A., et al., 2009, *The Astrophysical Journal*, **703**, 517
- De Jong R. S., Simard L., Davies R. L., Saglia R. P., Burstein D., Colless M., McMahan R., Wegner G., 2004, *Monthly Notices of the Royal Astronomical Society*, **355**, 1155
- Destrez R., Albouy-Kissi B., Treuillet S., Lucas Y., 2018, *Computer Methods in Biomechanics and Biomedical Engineering: Imaging & Visualization*, **0**, 1
- Diemand J., Kuhlen M., Madau P., 2007, *The Astrophysical Journal*, **667**, 859
- Dubois Y., et al., 2014, *Monthly Notices of the Royal Astronomical Society*, **444**, 1453
- Erwin P., 2004, *Astronomy and Astrophysics*, **415**, 941
- Erwin P., 2015, *The Astrophysical Journal*, **799**, 226
- Erwin P., Sparke L. S., 2003, *The Astrophysical Journal Supplement Series*, **146**, 299
- Erwin P., Pohlen M., Beckman J. E., 2008, *The Astronomical Journal*, **135**, 20
- Eskridge P. B., et al., 2002, *The Astrophysical Journal Supplement Series*, **143**, 73
- Ferrari F., Dottori H., Caon N., Nobrega A., Pavani D. B., 2004, *Monthly Notices of the Royal Astronomical Society*, **347**, 824
- Ferrari F., de Carvalho R. R., Trevisan M., 2015, *The Astrophysical Journal*, **814**, 55
- Firmani C., Avila-Reese V., 2003, in Avila-Reese V., Firmani C., Frenk C. S., Allen C., eds, Revista Mexicana de Astronomía y Astrofísica, vol. 27 Vol. 17, Revista Mexicana de Astronomía y Astrofísica Conference Series. pp 107–120 ([arXiv:astro-ph/0303543](https://arxiv.org/abs/astro-ph/0303543))
- Fisher D., 1997, *AJ*, **113**, 950
- Fisher D. B., Drory N., 2008, *The Astronomical Journal*, **136**, 773
- Fisher D. B., Drory N., 2010, *The Astrophysical Journal*, **716**, 942
- Fisher D. B., Drory N., Fabricius M. H., 2009, *The Astrophysical Journal*, **697**, 630
- Freeman K. C., 1970, *The Astrophysical Journal*, **160**, 811
- Gadotti D. A., 2008, *Monthly Notices of the Royal Astronomical Society*, **384**, 420
- Gadotti D. A., 2009, *Monthly Notices of the Royal Astronomical Society*, **393**, 1531
- Gadotti D. A., de Souza R. E., 2006, *The Astrophysical Journal Supplement Series*, **163**, 270
- Gadotti D. A., Athanassoula E., Carrasco L., Bosma A., de Souza R. E., Recillas E., 2007, *Monthly Notices of the Royal Astronomical Society*, **381**, 943
- Gao H., Ho L. C., 2017, *The Astrophysical Journal*, **845**, 114
- Grossi M., Fernandes C. A. C., Sobral D., Afonso J., Telles E., Bizzocchi L., Paulino-Afonso A., Matute I., 2018, *Monthly Notices of the Royal Astronomical Society*, **475**, 735
- Guedes J., Mayer L., Carollo M., Madau P., 2013, *The Astrophysical Journal*, **772**, 36
- Haussler B., et al., 2007, *The Astrophysical Journal Supplement Series*, **172**, 615
- Hinz J. L., Rieke G. H., Caldwell N., 2003, *The Astronomical Journal*, **126**, 2622
- Hopkins P. F., et al., 2010, *The Astrophysical Journal*, **715**, 202
- Hubble E. P., 1936, *Realm of the Nebulae*
- Jedrzejewski R. I., 1987, *Monthly Notices of the Royal Astronomical Society*, **226**, 747
- Jungwiert B., Combes F., Axon D. J., 1997, *Astronomy & Astrophysics Supplement series*, **125**, 479
- Kaviraj S., et al., 2017, *Monthly Notices of the Royal Astronomical Society*, **467**, 4739
- Keselman J. A., Nusser A., 2012, *Monthly Notices of the Royal Astronomical Society*, **424**, 1232
- Kim T., et al., 2012, *The Astrophysical Journal*, **753**, 43
- Kormendy J., Bender R., 2012, *The Astrophysical Journal Supplement*, **198**, 2
- Kormendy J., Kennicutt Jr. R. C., 2004, *ARA&A*, **42**, 603
- Lauer T. R., et al., 2007, *The Astrophysical Journal*, **664**, 226
- Laurikainen E., Salo H., 2017, *Astronomy & Astrophysics*, **598**, A10
- Laurikainen E., Salo H., Buta R., 2005, *Monthly Notices of the Royal Astronomical Society*, **362**, 1319
- Laurikainen E., Salo H., Buta R., Knapen J., Speltinx T., Block D., 2006, *The Astronomical Journal*, **132**, 2634
- Laurikainen E., Salo H., Buta R., Knapen J. H., Comerón S., 2010, *Monthly Notices of the Royal Astronomical Society*, **405**, 1089
- Laurikainen E., Peletier R., Gadotti D. e., 2016, Galactic Bulges, 1 edn. Astrophysics and Space Science Library 418, Springer International Publishing, <https://www.springer.com/gp/book/9783319193779>
- Lee J., Nishikawa R. M., Reiser I., Boone J. M., Lindfors K. K., 2015, *Medical Physics*, **42**, 5479
- Li Z.-Y., Ho L. C., Barth A. J., Peng C. Y., 2011, *The Astrophysical Journal Supplement Series*, **197**, 22
- Luders E., Thompson P., Narr K., Toga A., Jancke L., Gaser C., 2006, *NeuroImage*, **29**, 1224
- Malin D. F., 1977, *AAS Photo Bulletin*, **16**, 10
- Martin G., et al., 2019, *Monthly Notices of the Royal Astronomical Society*, **485**, 796
- Meert A., Bernardi M., Vikram V., 2013, *Monthly Notices of the Royal Astronomical Society*, **433**, 1344
- Méndez-Abreu J., et al., 2018, *Monthly Notices of the Royal Astronomical Society*, **474**, 1307
- Meurer G. R., et al., 2006, *The Astrophysical Journal Supplement Series*, **165**, 307
- Milone A. D. C., Rickes M. G., Pastoriza M. G., 2007, *Astronomy and Astrophysics*, **469**, 89
- Moiseev A. V., Valdés J. R., Chavushyan V. H., 2004, *Astronomy and Astrophysics*, **421**, 433
- Molaeinezhad A., Falcón-Barroso J., Martínez-Valpuesta I., Khosroshahi H. G., Vazdekis A., La Barbera F., Peletier R. F., Balcells M., 2017, *MNRAS*, **467**, 353
- Morgan W. W., 1958, *Publications of the Astronomical Society of the Pacific*, **70**, 364
- Muñoz-Mateos J. C., et al., 2013, *The Astrophysical Journal*, **771**, 59
- Mulchaey J. S., Regan M. W., Kundu A., 1997, *The Astrophysical Journal Supplement Series*, **110**, 299
- Naab T., Trujillo I., 2006, *Monthly Notices of the Royal Astronomical Society*, **369**, 625
- Nair P. B., Abraham R. G., 2010, *The Astrophysical Journal Supplement Series*, **186**, 427
- Nilson P., 1973, *Nova Acta Regiae Soc. Sci. Upsaliensis Ser. V*, **V**
- Peng C. Y., Ho L. C., Impey C. D., Rix H.-W., 2002, *The Astronomical Journal*, **124**, 266
- Pérez I., Sánchez-Blázquez P., Zurita A., 2009, *Astronomy and Astrophysics*, **495**, 775
- Petrosian V., 1976, *The Astrophysical Journal*, **209**, L1
- Pogge R. W., Martini P., 2002, *The Astrophysical Journal*, **569**, 624
- Preim B., Botha C. P., 2014, *Visual Computing for Medicine. Theory, Algorithms, and Applications*, 2 edn. Morgan Kaufmann
- Prieto M., Aguerri J. A. L., Varela A. M., Muñoz-Tuñón C., 2001, *Astronomy and Astrophysics*, **367**, 405
- Reynolds J. H., 1920, *Monthly Notices of the Royal Astronomical Society*, **80**, 746
- Salo H., et al., 2015, *The Astrophysical Journal Supplement Series*, **219**, 4
- Sandage A., 1961, *The Hubble atlas of galaxies*
- Sandage A., Tamman G. A., 1981, *A Revised Shapley-Ames Catalog of Bright Galaxies*
- Sani E., Marconi A., Hunt L. K., Risaliti G., 2011, *Monthly Notices of the Royal Astronomical Society*, **413**, 1479
- Schaye J., et al., 2015, *Monthly Notices of the Royal Astronomical Society*, **446**, 521

- Sérsic J. L., 1968, Atlas de galaxias australes
- Sheth K., et al., 2010, *PASP*, **122**, 1397
- Simard L., et al., 2002, *The Astrophysical Journal Supplement Series*, **142**, 1
- Simard L., Mendel J. T., Patton D. R., Ellison S. L., McConnachie A. W., 2011, *The Astrophysical Journal Supplement*, **196**, 11
- Springel V., et al., 2005, *Nature*, **435**, 629
- Sérsic J. L., 1963, Boletin de la Asociacion Argentina de Astronomia La Plata Argentina, **6**, 41
- Tarenghi M., Garilli B., Maccagni D., 1994, *The Astronomical Journal*, **107**, 1629
- Tenenblat K., 2008, Introdução à geometria diferencial, 2nd edn. Edgard Blucher
- Tonini C., Mutch S. J., Wyithe J. S. B., Croton D. J., 2016, *Monthly Notices of the Royal Astronomical Society*, **465**, 4133
- Toomre A., Toomre J., 1972, *The Astrophysical Journal*, **178**, 623
- Vogelsberger M., et al., 2014, *Monthly Notices of the Royal Astronomical Society*, **444**, 1518
- White S. D. M., Frenk C. S., 1991, *Astrophysical Journal*, **379**, 52
- White S. D. M., Rees M. J., 1978, *Monthly Notices of the Royal Astronomical Society*, **183**, 341
- Wozniak H., Pierce M. J., 1991, *A&AS*, **88**, 325
- Wyse R. F. G., Gilmore G., Franx M., 1997, *Annual Review of Astronomy and Astrophysics*, **35**, 637
- Yıldırım A., van den Bosch R. C. E., van de Ven G., Martín-Navarro I., Walsh J. L., Husemann B., Gültekin K., Gebhardt K., 2017, *Monthly Notices of the Royal Astronomical Society*, **468**, 4216
- Zhang J., 2015, Medicine Sciences and Bioengineering: Proceedings of the 2014 International Conference on Medicine Sciences and Bioengineering. ICMSB2014, CRC Press
- Zhao D. H., Jing Y. P., Börner G., Mo H. J., 2003, *Monthly Notices of the Royal Astronomical Society*, **339**, 12
- de Souza R. E., Gadotti D. A., dos Anjos S., 2004, *The Astrophysical Journal Supplement Series*, **153**, 411
- de Vaucouleurs G., 1959, Handbuch der Physik, **53**, 311
- de Vaucouleurs G., de Vaucouleurs A., Corwin Jr. H. G., Buta R. J., Paturel G., Fouqué P., 1991, Third Reference Catalogue of Bright Galaxies. Volume I: Explanations and references. Volume II: Data for galaxies between 0^h and 12^h . Volume III: Data for galaxies between 12^h and 24^h .
- del Rio M. S., Cepa J., 1998, *Astronomy and Astrophysics*, **340**, 1
- del Rio M. S., Cepa J., 1999, *Astronomy and Astrophysics Supplement*, **134**, 333
- van den Bergh S., 1960a, *Astrophysical Journal*, **131**, 215
- van den Bergh S., 1960b, *Astrophysical Journal*, **131**, 558
- van den Bergh S., 1976, *Astrophysical Journal*, **206**, 883

APPENDIX A: CURVATURE FOR A BULGE+DISK SÉRSIC PROFILE

A good description of brightness profile of different components of galaxies is given by the Sérsic law (Sérsic 1963; Sérsic 1968; Ciotti & Bertin 1999)

$$I(R) = I_n \exp \left\{ -b_n \left[\left(\frac{R}{R_n} \right)^{1/n} - 1 \right] \right\} \quad (\text{A1})$$

where R_n (effective radius) is the radii that contain half of the total luminosity of the galaxy integrated to infinity $L(R = R_n) = 0.5L_T^\infty$, and I_n is the effective surface brightness, i.e. the value of $I(R)$ at $R = R_n$, and n controls the concentration of the profile. The term b_n is defined to make the above definitions hold Ciotti & Bertin (1999)

$$b_n = 2n - \frac{1}{3} + \frac{4}{405n^2} + \frac{46}{25515n^2}. \quad (\text{A2})$$

Here we derive the curvature of a Sérsic law for a single

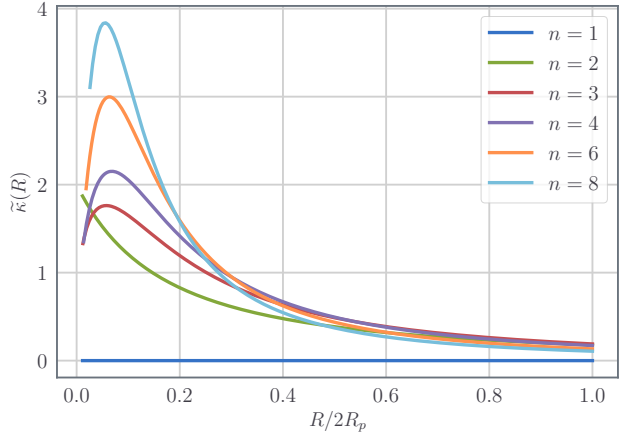


Figure A1. Plots of Equation (A9) for different Sérsic indexes. The higher is n , the higher is $\tilde{\kappa}$ in the inner regions, which is reasonable because high n represent inner components. Note that for large R , the $\tilde{\kappa}$ profiles are similar.

component. As commented, to remove the scale on I , we use normalization given by (3). Taking the logarithm of equation (A1) we have

$$\nu(R) \equiv \log I(R) = \log I_n + b(n) \left[1 - \left(\frac{R}{R_n} \right)^{1/n} \right]. \quad (\text{A3})$$

Since we consider galaxies extending up to $2R_p$, the maximum and minimum are at $R = 0$ and $R = 2R_p$, respectively, hence

$$\max \log I = I(0) = \log I_n + b(n) \quad (\text{A4})$$

$$\min \log I = I(2R_p) = \log I_n + b_n \left[1 - \left(\frac{2R_p}{R_n} \right)^{1/n} \right] \quad (\text{A5})$$

thus, inserting these into (3) gives

$$\nu(R) = 1 - \left(\frac{R}{2R_p} \right)^{1/n}. \quad (\text{A6})$$

This result is independent of I_n and R_n because of the normalization on I and on R . The first and second derivative are

$$\frac{d\nu(R)}{dR} = -\frac{1}{2R_p n} \left(\frac{R}{2R_p} \right)^{\frac{1-n}{n}} \quad (\text{A7})$$

$$\frac{d^2\nu(R)}{dR^2} = \frac{n-1}{4R_p^2 n^2} \left(\frac{R}{2R_p} \right)^{\frac{1-2n}{n}}. \quad (\text{A8})$$

Using these two result in equation (9) we obtain the normalized Sérsic curvature:

$$\tilde{\kappa}(R) = \frac{\frac{n-1}{n^2} \left(\frac{R}{2R_p} \right)^{\frac{1-2n}{n}}}{\left[1 + \frac{1}{n^2} \left(\frac{R}{2R_p} \right)^{\frac{2-2n}{n}} \right]^{3/2}} \quad (\text{A9})$$

Fig. A1 shows plots of (A9) for different values of n against the normalized variable $\chi = R/(2R_p)$. For a disk, which frequently follows an $n = 1$ law, we obtain that $\tilde{\kappa} = 0$ because the numerator vanishes. For $n > 1$, $\tilde{\kappa}$ is proportional to n (in the inner regions), for outer regions the Sérsic law becomes more flat and $\tilde{\kappa}$ behaves a disk.

APPENDIX B: ADDITIONAL CURVATURE PLOTS

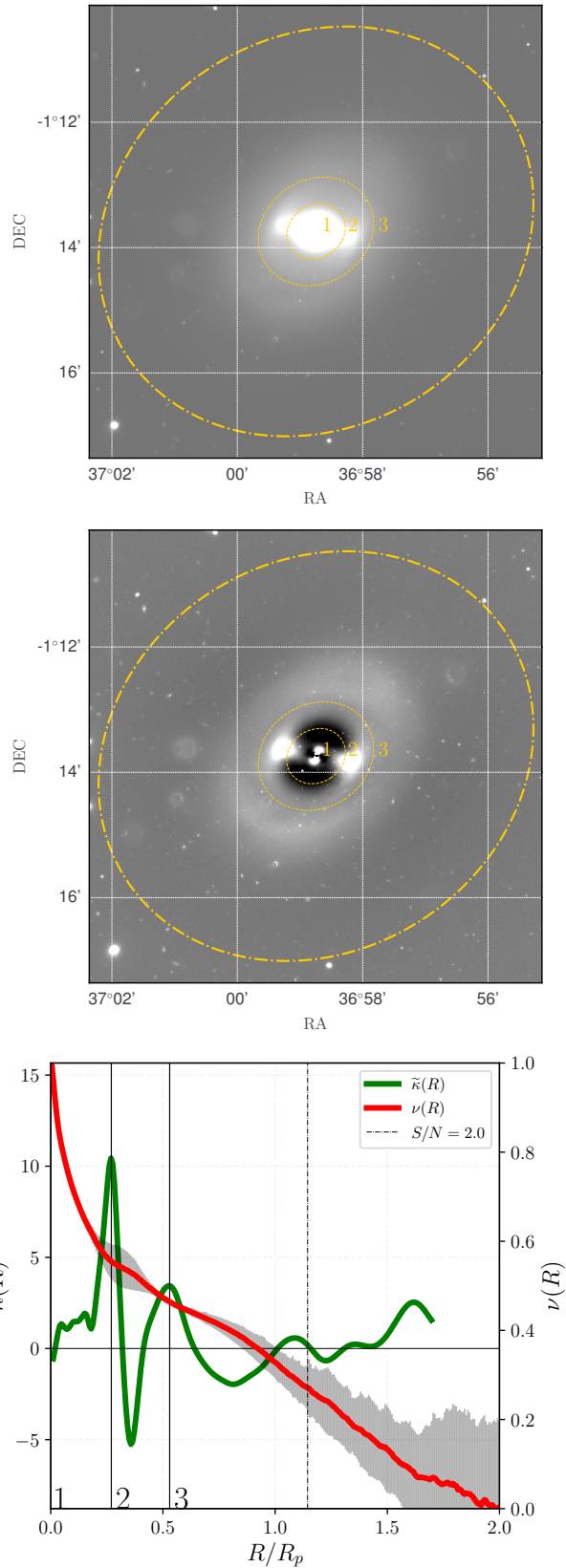


Figure B1. The same as Fig. 3, but for r band of NGC 936 from EFIGI. See text for details.

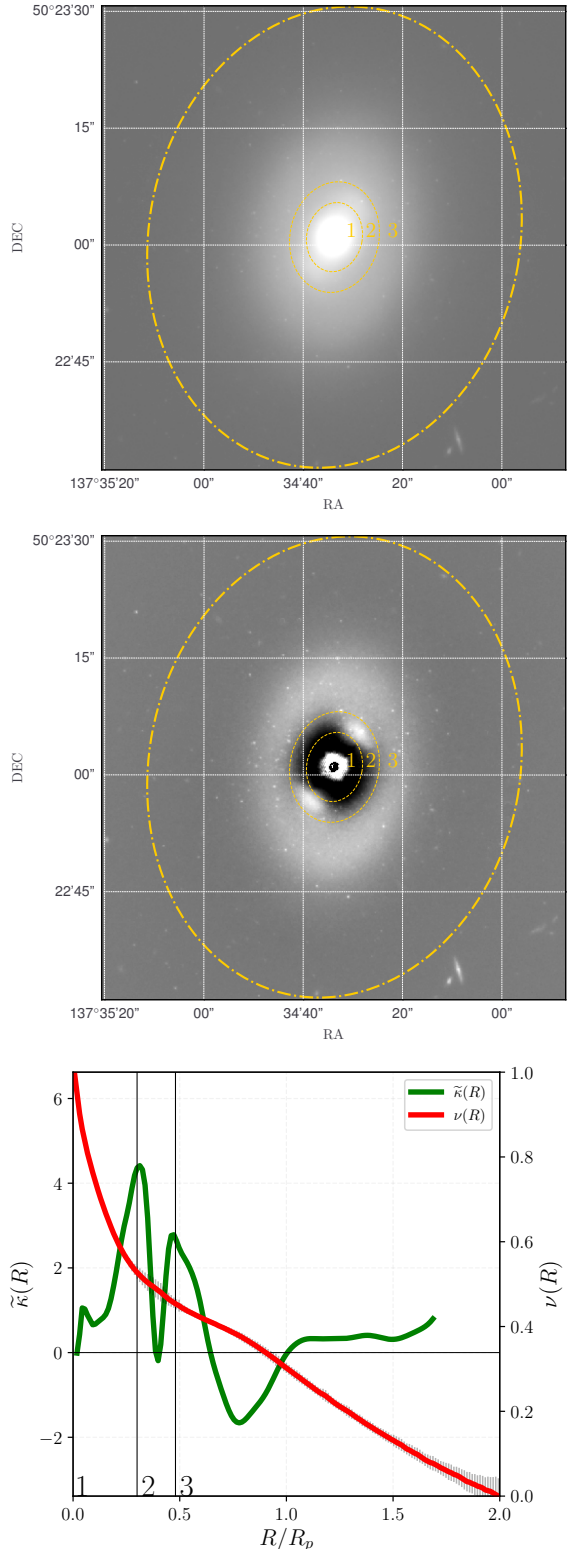


Figure B2. The same as Fig. 3, but for NGC 2767 from HST (f160w).

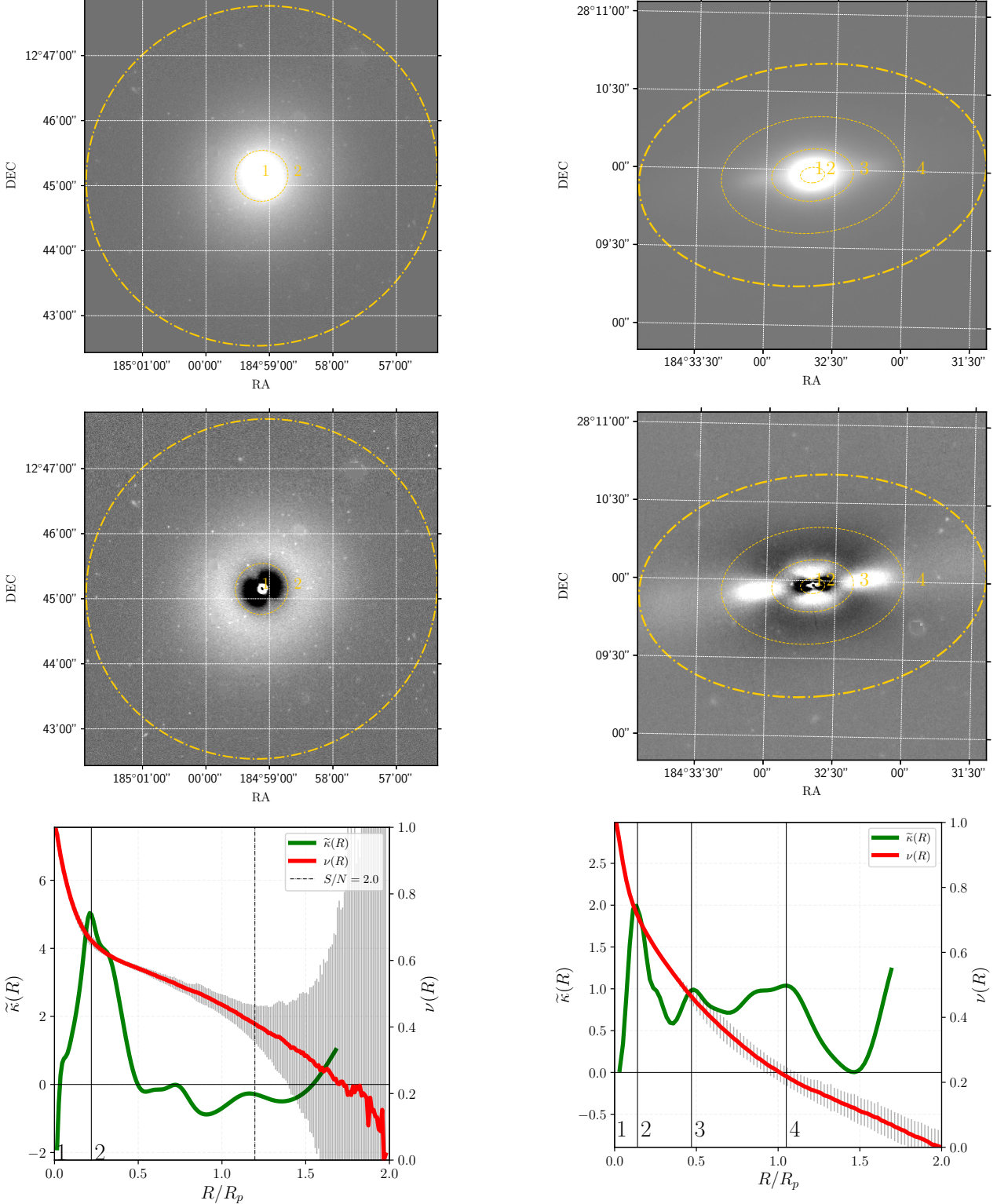


Figure B3. The same as Fig. 3, but for *r* band of NGC 4267 from EFIGI.

Figure B4. The same as Fig. 3, but for *i* band of NGC4251.

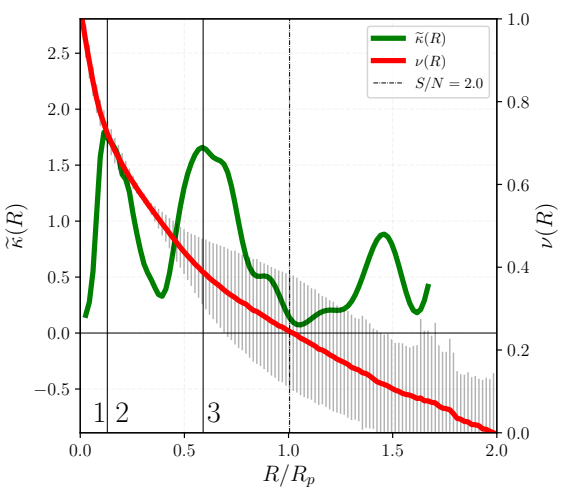
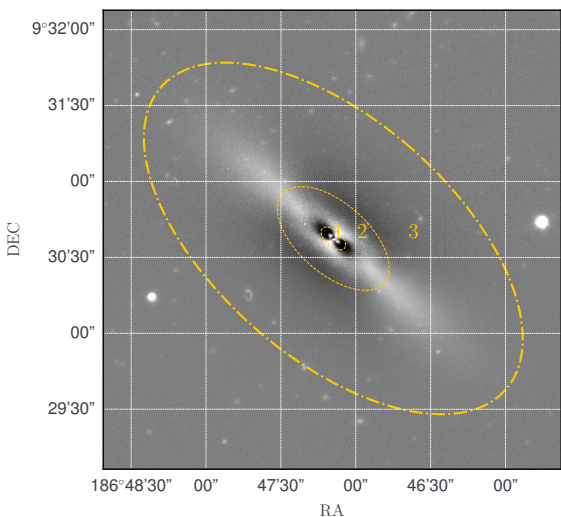
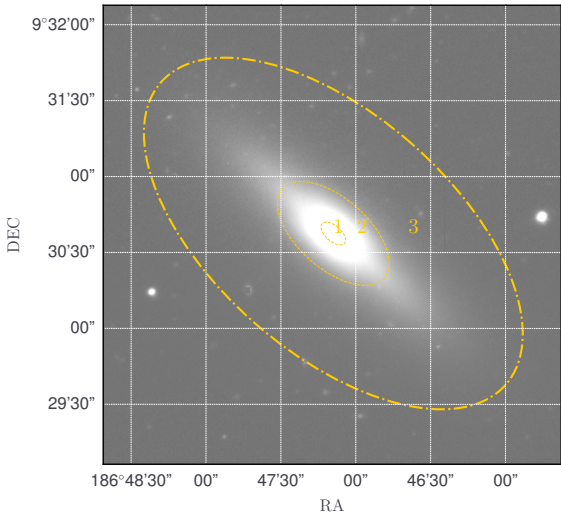


Figure B5. The same as Fig. 3, but for r band of NGC 4417.

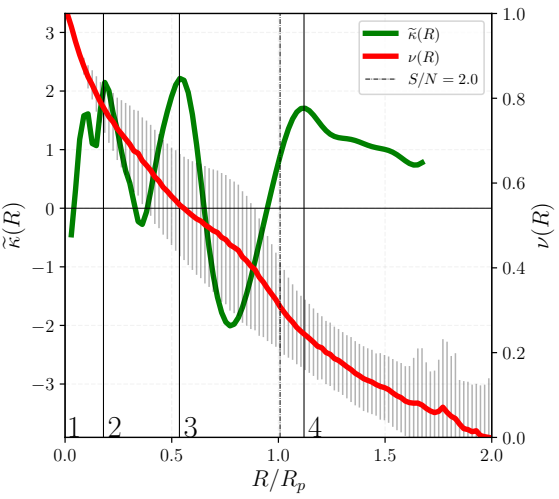
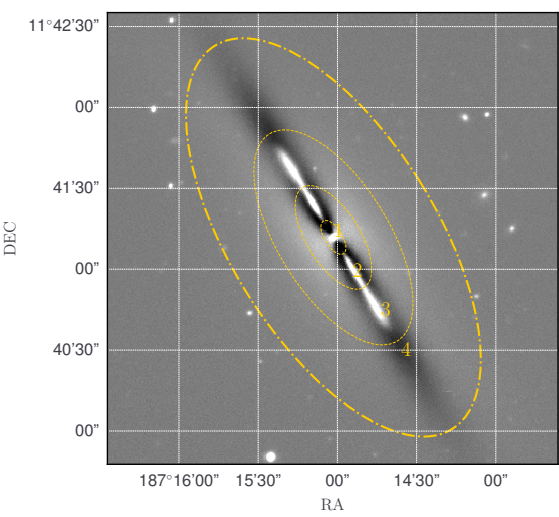
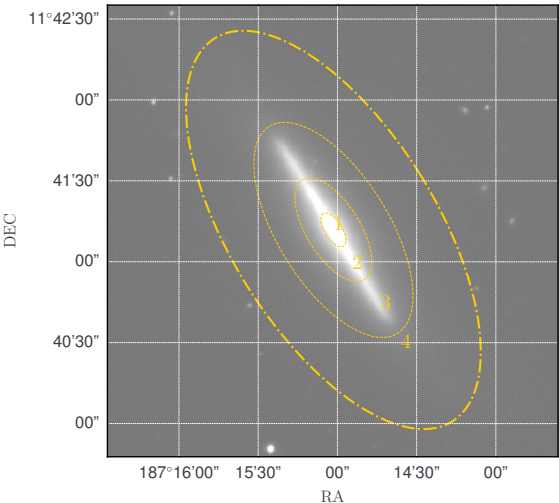


Figure B6. The same as Fig. 3, but for r band of NGC 4452.

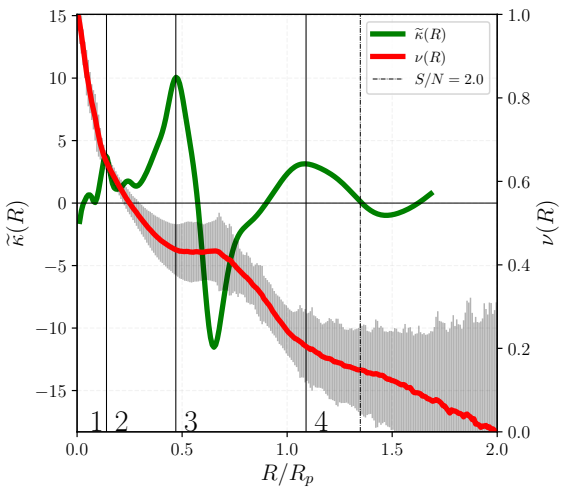
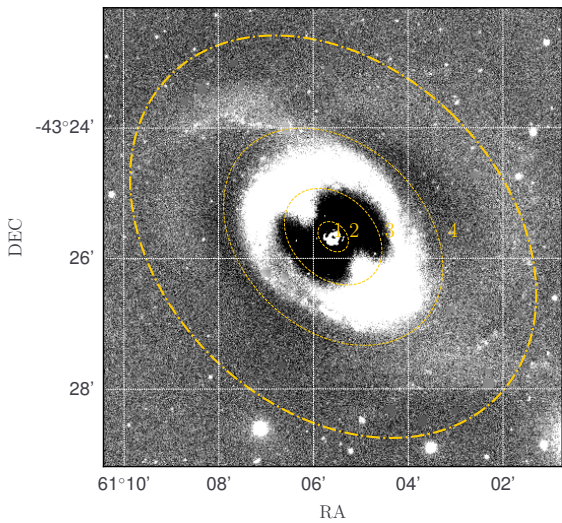
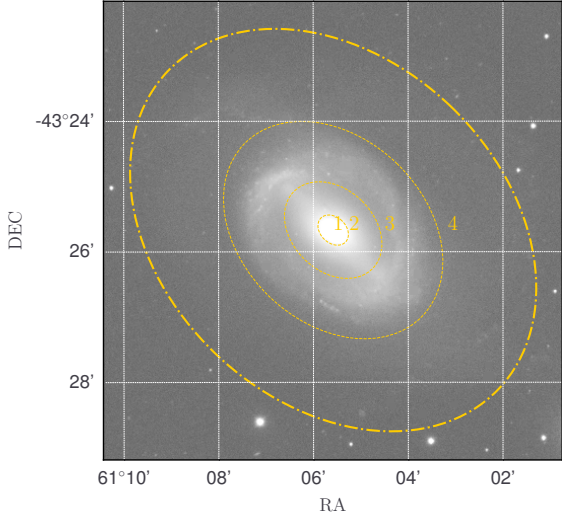


Figure B7. The same as Fig. 3, but for r band of NGC 1512 from CTIO telescope.

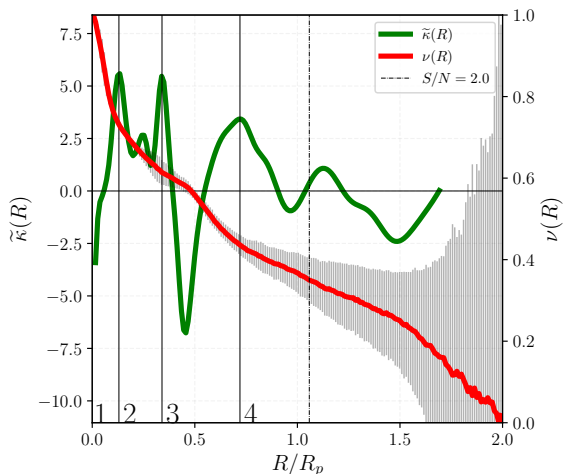
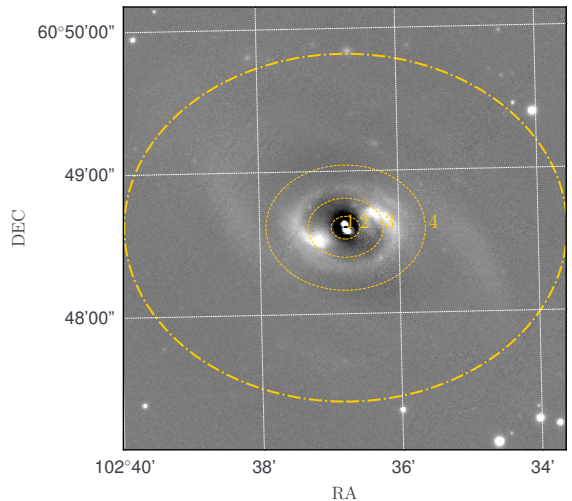
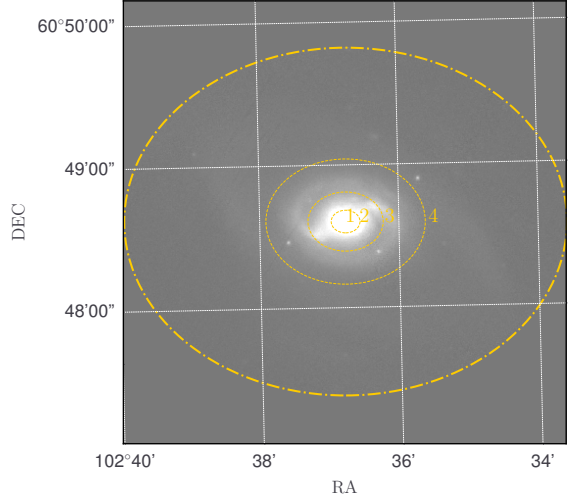


Figure B8. The same as Fig. 3, but for r band of NGC 2273 from Pan-STARRS.

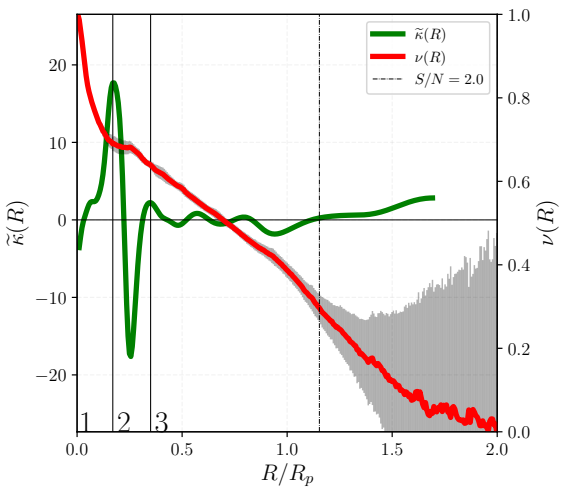
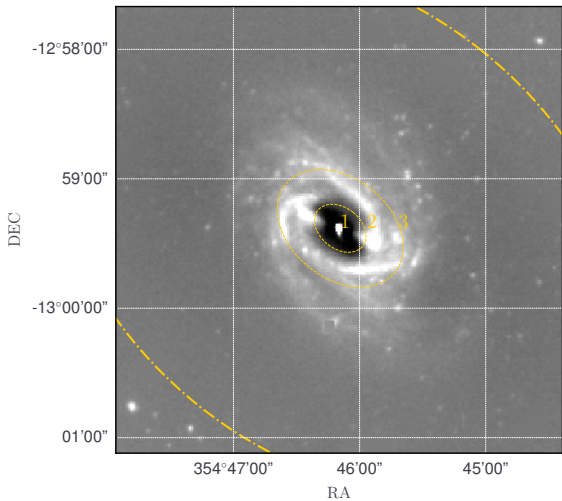
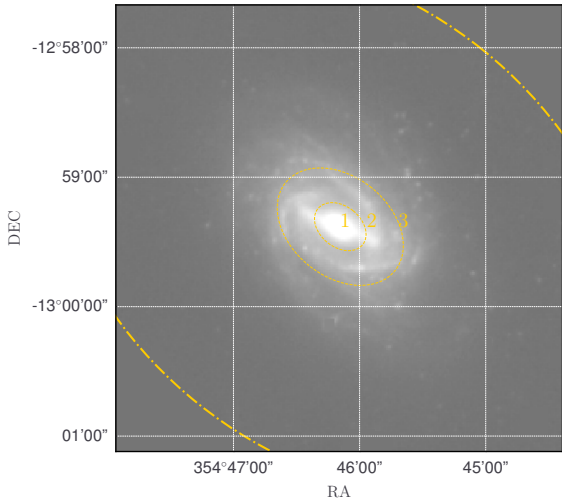


Figure B9. The same as Fig. 3, but for near infrared band ($3.56\mu\text{m}$) of NGC 7723 from Spitzer telescope.

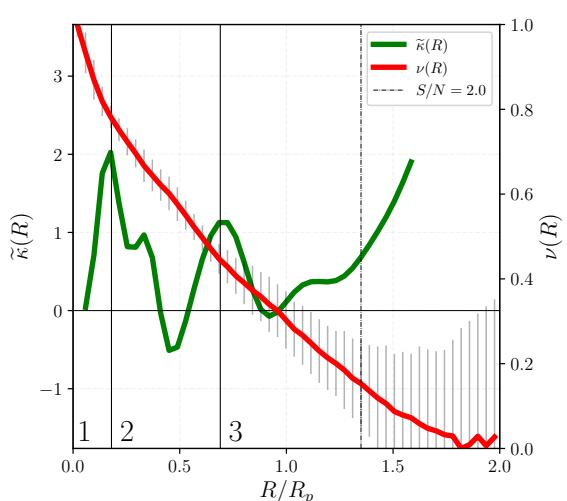
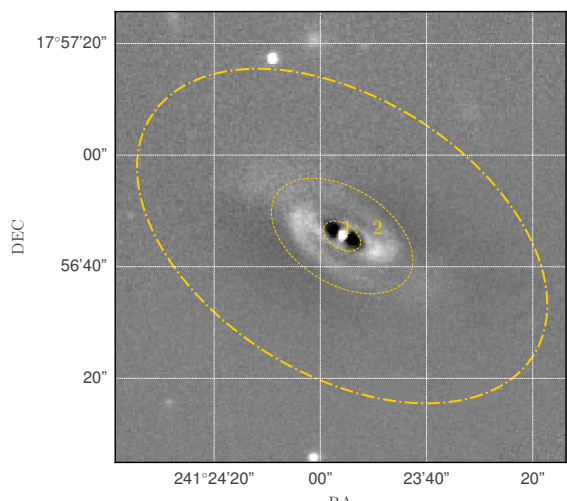
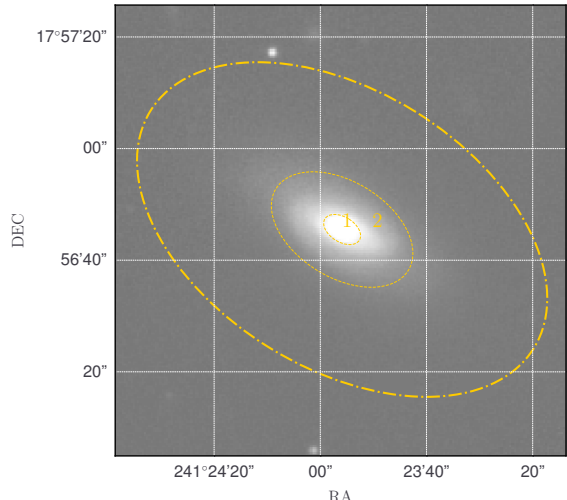


Figure B10. The same as Fig. 3, but for r band of NGC 6056.

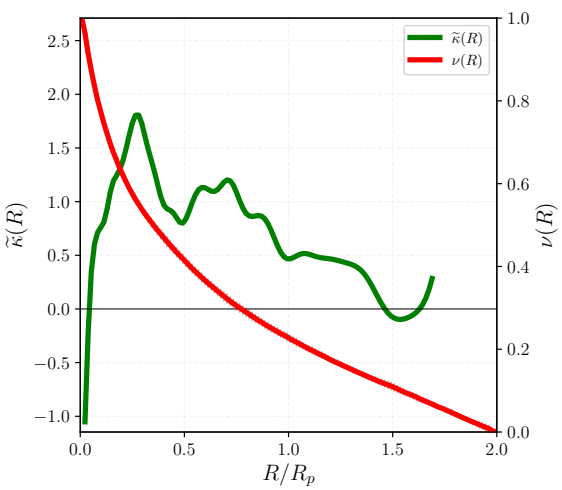
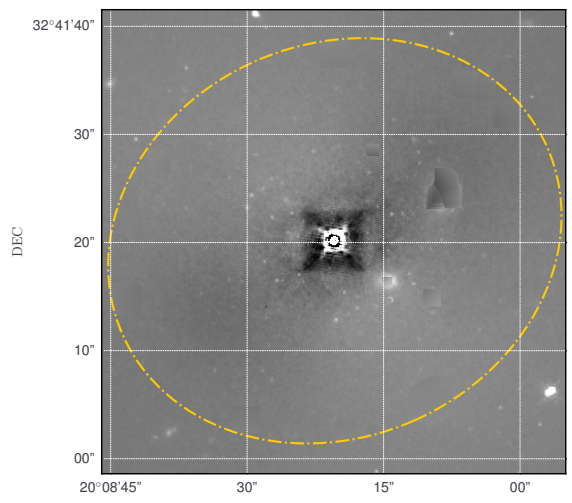
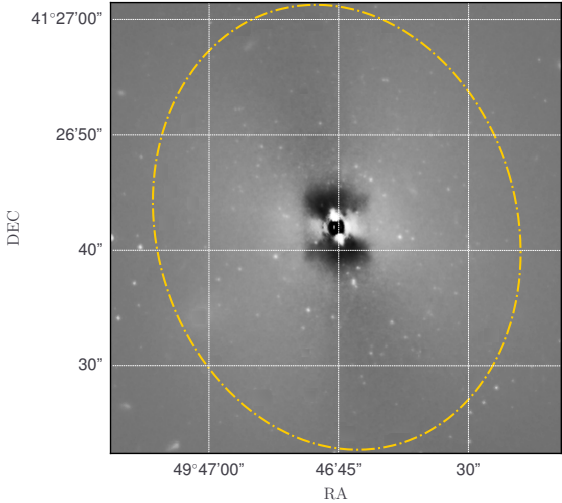
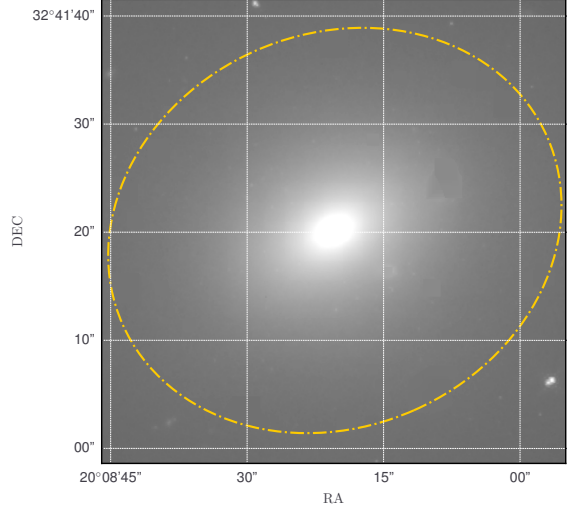
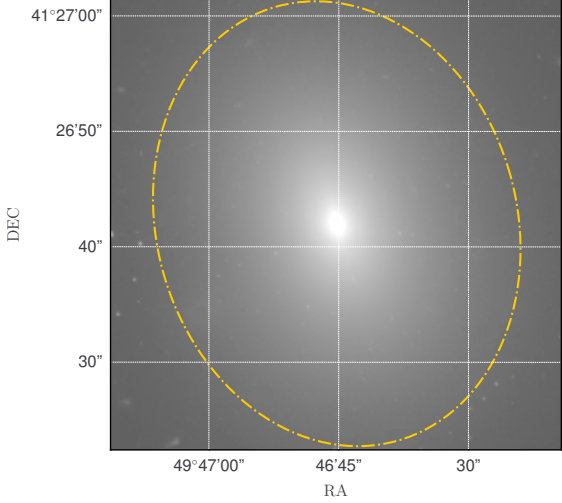


Figure B11. The same as Fig. 3, but for NGC 1270 from HST (f160w).

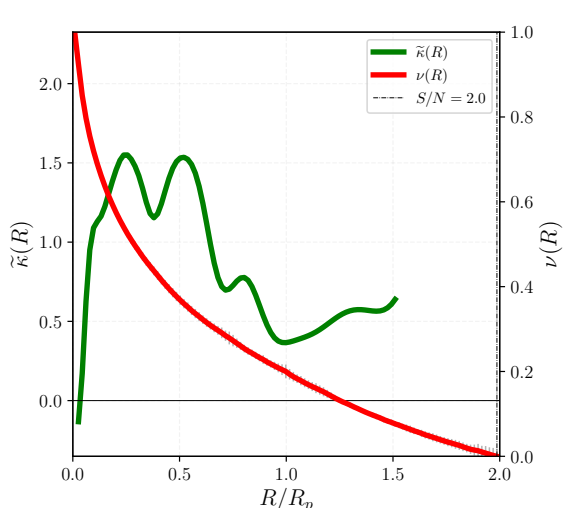


Figure B12. The same as Fig. 3, but for NGC 472 from HST (f160w).

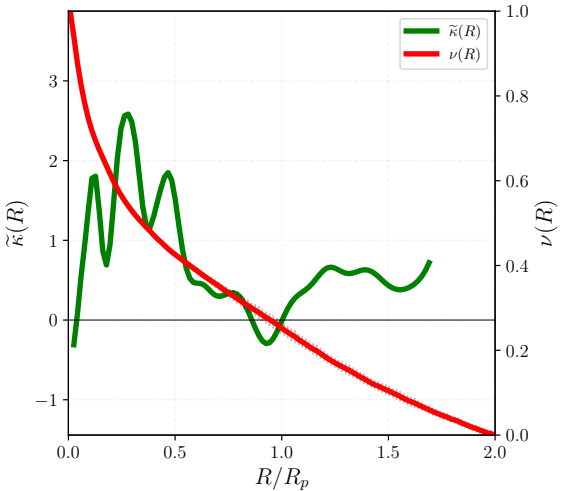
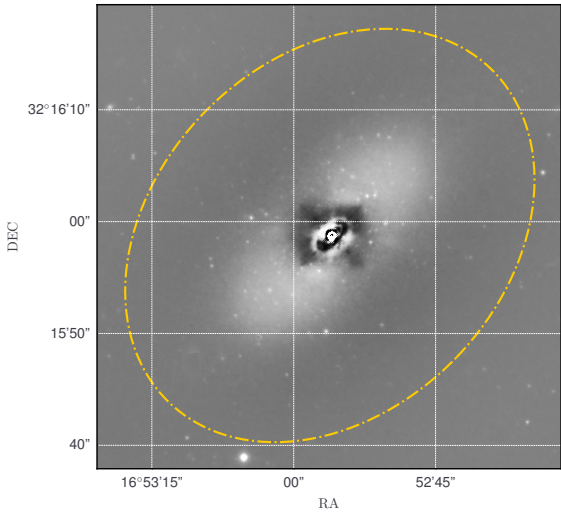
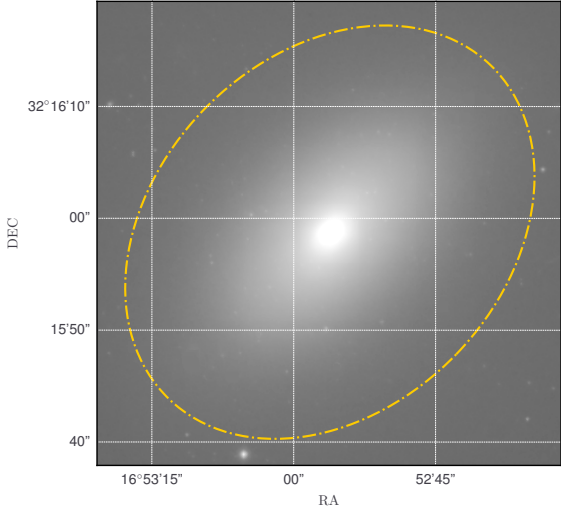


Figure B13. The same as Fig. 3, but for NGC 384 from HST (f160w).

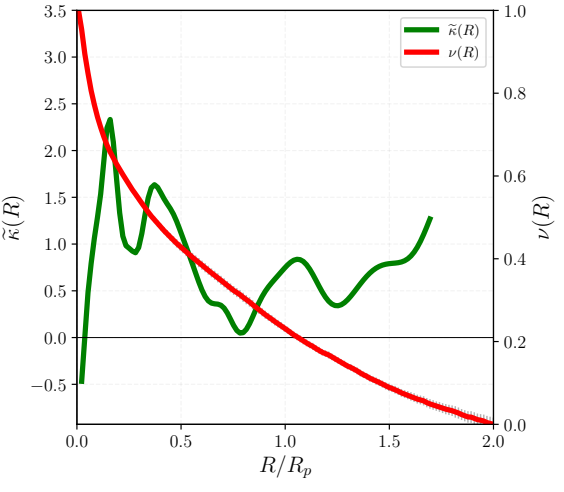
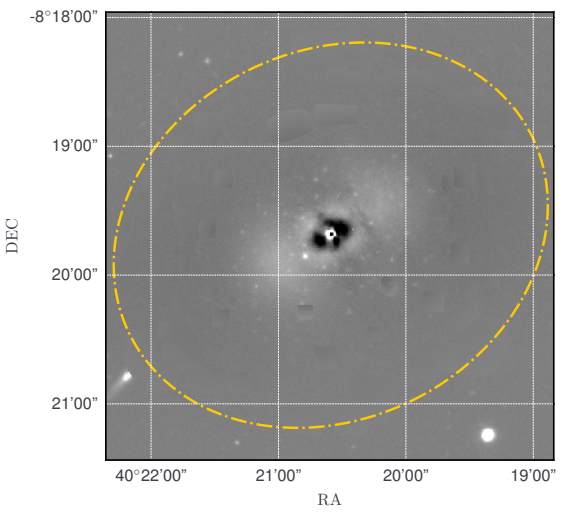
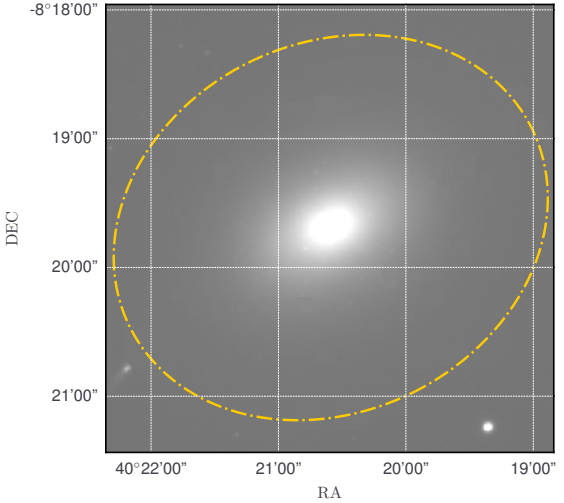


Figure B14. The same as Fig. 3, but for r -band of NGC 1052 from EFIGI.

B

Python code for $\tilde{\chi}(R)$

All implementations were done in Python, version 2.7, with libraries `numpy`, `scipy`, `pyfits`, `pylab`, `matplotlib` and `astropy`. Also, the `MORFOMETRYKA` algorithm was used: i) for image segmentation; ii) star masking; iii) calculation of $I(R)$; iv) calculation of the petrosian region R_p ; and v) residuals of the images.

The algorithm associated to $\tilde{\chi}(R)$ takes as input the profile $I(R)$ to be processed further, as is shown bellow.

```
#!/usr/bin/python
#-*- coding: utf-8 -*-
#kurvature.py

from __future__ import division

import matplotlib.pyplot as plt

import numpy as np

import scipy as sp

import scipy.integrate as si

import scipy.signal

import argparse

import os

from matplotlib import gridspec

import pylab as pl

from matplotlib import cm

import astropy.io.fits as pf
```

```

class kurv_mfmtk():

    def config(self):

        'Initial configurations.'

        self.Smin = self.RAIOS[-1]*0.004*0.5

        self.Smax = self.RAIOS[-1]*0.08*0.5

        self.window = 16 #for kur 2d

        self.order = 3

    def __init__(self,filename,psf_name=None,Raios=None,IR=None,Rmin=None):

        self.filename = filename

        self.psf_name = psf_name

        #Call morfometryka

        import morfometryka700 as mfm

        import morfometrykalib700 as mfl

        self.s = mfm.Stamp(self.filename,self.psf_name)

        self.p = mfm.Photometry(self.s)

        self.gal_image = self.p.galnostars #take the segmented image from mfm700

        self.RP = self.p.Rp

        self.RAIOS = self.p.Raios

        self.Ir = self.p.IR

        self.IRerror = self.p.IRerr

        self.IRshape = len(self.Ir)

        self.config()

        self.kurv1Dlog()

        self.plot_cur()

    def kurv1Dlog(self):

        'Calculate K(R)'

        def renormaliza(x):

            print x.min(),x.max()

            return (x-x.min())/(x.max()-x.min())

        def gaussian(x, x0, sigma):

            return 1. / (sigma * np.sqrt(2. * np.pi)) * np.exp(-(x-x0)**2. / (2. * sigma**2.))

        def apply_filter(I,R,PLOT=False):

```

```

Sigma = ((self.Smax-self.Smin)/R[-1])2R + self.Smin

Inew = np.zeros_like(I)

for i in range(len(I)):

    G = gaussian(np.arange(len(I)), float(i), Sigma[i] )

    G=G/G.sum()

    Inew[i] = (I * G).sum()

if PLOT==True:

    plt.plot(R/(0.5*R[-1]),I,label="original")

    plt.plot(R/(0.5*R[-1]),Inew,label="filtered")

    plt.plot(R/(0.5*R[-1]),I-Inew,label="residual")

    plt.legend()

    plt.grid()

return Inew

def Hentropy(data, bins=256,b=1,normed=1,meth="scott"):

    'Shannon entropy (Ferrari, 2015).'

    h = pl.histogram(data, bins=bins, normed=True)[0]

    pimg = h/float(h.sum())

    S = pl.sum([- p*pl.log(p) for p in pimg if p!=0 ])

    if normed==1:

        N = pl.log(bins)

    else:

        N = 1.0

    return S/N,bins

from scipy.ndimage.filters import gaussian_filter as GF

from medpy.filter.smoothing import anisotropic_diffusion as AD

self.Raios_new, self.IR_new = self.RAIOS, self.Ir

self.nu = apply_filter(renormaliza(np.log(self.IR_new) ),\

self.Raios_new,PLOT=True)

self.nu_o = renormaliza(np.log(self.Ir))

self.MUR = -2.5*np.log10(self.Ir[self.Rmin:])

self.MURerr = -2.5/(np.log(10) * self.Ir[self.Rmin:]) * self.IRerror[self.Rmin:]

#First derivatives

```

```

    self.dI = np.gradient(self.nu_0,1)

    self.dIs = np.gradient(self.nu,1.0)

    self.dR = np.gradient(self.Raios_new/self.Raios_new[—1],1.0)

#Second derivatives.

    self.d2Is =np.gradient(self.dIs,1)

    self.d2I = np.gradient(self.dI,1.0)

    self.d2R = np.gradient(self.dR)

#Curvature

    self.Kurvature_s = (self.dR* self.d2Is — self.dIs* self.d2R) / \
        np.power(self.dR** 2 + self.dIs** 2, 1.5)

#Update filtered quantities.

    self.dIs = self.dIs[self.Npts_i:]

    self.d2Is = self.d2Is[self.Npts_i:]

    self.Raios_new = self.Raios_new[self.Npts_i:]

    self.Kurvature_s = self.Kurvature_s[self.Npts_i:]

#Curvature without filter.

    self.Kurvature = (self.dR[self.Npts_i:]* self.d2I — self.dI* self.d2R[\
        self.Npts_i:]) / np.power(self.dR[self.Npts_i]** 2 + self.dI** 2, 1.5)

#Calculate the entropy of the kurvature profile.

    self.kur_entropy,self.kur_entropy_bins = Hentropy(self.Kurvature_s,\

        bins=int(self.RP/2),b=1)

    print "Entropy =",self.kur_entropy

#Separate the positive values from negative values of the curvature.

    positive_kur = np.zeros(len(self.Kurvature_s))

    negative_kur = np.zeros(len(self.Kurvature_s))

    positive_kur[self.Kurvature_s>0] = self.Kurvature_s[self.Kurvature_s>0]

    negative_kur[self.Kurvature_s<0] = self.Kurvature_s[self.Kurvature_s<0]

    init = 2*int(self.Smin)+int(1)*3

    index_max=int(len(self.Raios_new)*1.4*0.5)

    self.mean_kurv = self.Kurvature_s[init:index_max].mean()

    self.cumsum_kurv = self.Kurvature_s[init:index_max].sum()

    self.positive_mean_kurv = positive_kur[init:index_max].mean()

```

```

self.negative_mean_kurv = negative_kur[init:index_max].mean()

self.positive_cumsum_kurv = positive_kur[init:index_max].sum()

self.negative_cumsum_kurv = negative_kur[init:index_max].sum()

maxKindex = np.argmax(self.Kurvature_s[init:index_max])

minKindex = np.argmin(self.Kurvature_s[init:index_max])

#This takes only the max point of k(R)

self.KurPeak = self.Kurvature_s[init:index_max][maxKindex]

self.RKurPeak = self.RAIOS[init:index_max][maxKindex]

#For minimum value:

self.KurValley = self.Kurvature_s[init:index_max][minKindex]

self.RKurValley = self.RAIOS[init:index_max][minKindex]

RRR = self.RAIOS/self.RP

#Total Area under k(R).

self.Area = si.trapz(self.Kurvature_s[init:index_max]\
, RRR[init:index_max])

#Positive Area under k(R).

self.Area_pos = si.trapz(positive_kur[init:index_max]\
, RRR[init:index_max])

#Negative Area under k(R).

self.Area_neg = si.trapz(negative_kur[init:index_max]\
, RRR[init:index_max])

print "Area under K(R) =", self.Area

print "          + =" , self.Area_pos

print "          - =" , self.Area_neg

print "<K(R)> =", self.mean_kurv

print len(self.Raios_new), len(self.IR_new)

print self.Raios_new[-1], self.RP

#curvature 2d— kur 2d

dx,dy = np.gradient(renormaliza(np.log(abs(self.gal_image))),1.0)

self.dI_2D = np.sqrt(dx**2.+dy**2.)

try:

dxs,dys = mfl.savitzky_golay_2d(renormaliza(np.log(abs(self.gal_image))),\
```

```

int((self.window)/2.), self.order,derivative = "both")

except:

dxs,dys = mfl.savitzky_golay_2d(renormaliza(np.log(abs(self.gal_image))), \
int((self.window)/2.+1), self.order,derivative = "both")

self.dIs_2D = np.sqrt(dxs**2.0+dys**2.0)

dxs2,dys2 = mfl.savitzky_golay_2d(self.dIs_2D,int(self.window+1), self.order,\

derivative = "both")

self.d2Is_2D = np.sqrt(dxs2**2.0+dys2**2.0)

dx2,dy2 = np.gradient(self.dI_2D,1.0)

self.d2I_2D = np.sqrt(dx2**2.+dy2**2.)

self.Kurvature_s_2D = ( self.d2Is_2D )/ ( 1. + (self.dIs_2D)**2. )** (3/2.)

self.Kurvature_2D = ( self.d2I_2D )/ ( 1. + (self.dI_2D)**2. )** (3/2.)

self.Kurvature_s_2D = self.Kurvature_s_2D[self.Npts:]

self.Kurvature_grad_2D = ( self.d2I_2D )/ ( 1. + (self.dI_2D)**2. )** (3/2.)

#end

```
